

Modeling Impact Transients Analysis in the Time-Domain

Master of Science Thesis in the Master's Programme Sound and Vibration

HENRIK GULDBRANSEN
MATTIAS LUNDIN

Modeling Impact Transients
Analysis in the Time-Domain

© HENRIK GULDBRANSEN & MATTIAS LUNDIN, 2015

Master's Thesis 2015:151

Department of Civil and Environmental Engineering
Division of Applied Acoustics
Vibroacoustics Group
Chalmers University of Technology
SE-41296 Göteborg
Sweden

Tel. +46-(0)31 772 1000

Reproservice / Department of Civil and Environmental Engineering
Göteborg, Sweden 2015

Modeling Impact Transients
Analysis in the Time-Domain
Master's Thesis in the Master's programme in Sound and Vibration
HENRIK GULDBRANSEN & MATTIAS LUNDIN
Department of Civil and Environmental Engineering
Division of Applied Acoustics
Vibroacoustics Group
Chalmers University of Technology

Abstract

This thesis has studied whether or not the LMS adaptive algorithm is a favourable way of estimating the forces acting upon a car when hitting a small obstacle. The study has mainly been made as a comparison between the LMS algorithm and an IFRF method using three different approaches. First approach was a virtual study, comparing how well the forces were estimated by the two methods. The next step was using impact hammer measurements to determine how well the method could recreate a simple excitation. Lastly pressure was measured inside a car compartment while it was being driven over an obstacle and the pressure was calculated using each of the methods. The results of the first two cases suggests that the LMS is a more favourable approach when estimating the actual excitation. This was also found in the last case where the energy spectral density of the calculated pressure is estimated fairly well by both methods. In time domain there were larger differences between the estimated forces and the measurements.

Keywords: Force identification, Impact transient, time-domain, LMS-algorithm.

Contents

Abstract	iii
Contents	iv
Acknowledgements	xiii
Notations	xv
1. Introduction	1
2. Theory	3
2.1. The Inverse Problem	3
2.2. Force Identification	4
2.2.1. Frequency Domain Methods	4
2.2.2. Single Value Decomposition	5
2.2.3. Implementation of IFRF in MATLAB	7
2.2.4. Limitations	7
2.2.5. Time Domain Methods	9
2.2.6. The LMS-algorithm	9
2.2.7. About the LMS-algorithm	9
2.2.8. The LMS-algorithm as a Force Identification Method	11
2.2.9. Implementation of LMS method in MATLAB	13
2.2.10. MISO-System	16
2.2.11. SIMO	16
2.2.12. MIMO	18
2.3. Short on transients	19
2.3.1. Windowing and the ESD	19
2.4. Defining a System of Coordinates	21
2.5. Noise Generation	22
2.5.1. Wave Propagation in Tyres	22

3. Measurements	27
3.1. Drum Measurement Setup	27
3.1.1. List of Equipment	28
3.1.2. Notes About the Method	29
3.1.3. Measurement Points	29
3.2. Impact Measurements	31
3.2.1. Impact Measurement Setup	31
3.2.2. List of Equipment	32
3.2.3. Measurements	32
4. "Simulations"	35
4.1. Virtual Simulation	35
4.1.1. Verification of Method	35
4.1.2. Comparison with IFRF	44
4.2. Impact Hammer Simulations	48
4.2.1. SIMO Simulation	48
4.2.2. MIMO Simulation	50
4.3. MIMO Equivalent Forces	60
4.4. Drum Measurement Simulations	65
4.4.1. Calculation of Accelerations	65
4.4.2. Calculation of Pressure	69
4.4.3. Comments On Drum Measurements	73
5. Conclusions	77
5.1. Virtual simulations	77
5.2. Impact Hammer Simulations	77
5.3. Drum simulations	78
5.3.1. Accelerations	78
5.3.2. Pressure	78
5.4. Concluding Remarks	79
References	81
A. Glossary	83

List of Figures

2.1.	The direct problem (i) and the inverse problem (ii).	3
2.2.	Rough outline of the implementation of the IFRF method in MATLAB. For further explanation of the notations used, see section 2.2.1.	8
2.3.	Block diagram of an adaptive controller.	9
2.4.	Block diagram of a modified controller.	11
2.5.	Example of the original force and the force recreated by an LMS-algorithm.	12
2.6.	Rough outline of the implementation of the LMS method in MATLAB.	15
2.7.	Block diagram of a MISO system.	16
2.8.	Block diagram of a MISO system.	17
2.9.	Block diagram of a MIMO system.	18
2.10.	Definitions for the forces and directions.	21
2.11.	Wave types propagating on a tyre: Bending wave (i), longitudinal wave (ii) and rotational wave (iii) (Taken from [13]).	22
2.12.	Modal (i) and non-modal (ii) behavior of a tyre. (iii) shows the cavity resonance of the cavity and \uparrow denotes the point of excitation.	23
2.13.	The four first modes of an unconstrained tire.	25
2.14.	The four first modes of a tire constrained by a road surface.	26
3.1.	The setup of the measurements conducted at Volvo PV.	27
3.2.	Obstacles used in measurements.(i) and (ii) are made out of steel while (iii) is made out of aluminum	28
3.3.	Accelerometer positions on the knuckle. The positions of the accelerometers are indicated by \bullet (Modified from [19]).	30
3.4.	Approximate locations of accelerometers ($a_1 - a_6$) and microphone (p) during measurements. Also marked in the figure is the approximate position of the excitations (F_{xyz}).	31
3.5.	Picture showing the locations where transfer functions were measured and in which direction the force was applied.	33
3.6.	Illustrating the cube and from where and in which directions the transfer functions were measured.	33
4.1.	Original signal plotted with the signal with added noise.	36

4.2. Comparing estimated forces, using LMS, with input signal in time domain.	36
4.3. Comparing estimated moments, using LMS, with input signal in time domain.	37
4.4. Comparing the spectra of the two methods with the original spectra for X-direction.	37
4.5. Comparing the spectra of the two methods with the original spectra for Y-direction.	38
4.6. Comparing the spectra of the two methods with the original spectra for Z-direction.	38
4.7. Comparing the spectra of the two methods with the original spectra for moment around X-axis.	39
4.8. Comparing the spectra of the two methods with the original spectra for moment around Y-axis.	39
4.9. Comparing the spectra of the two methods with the original spectra for moment around Z-axis.	40
4.10. Comparing the spectra of the two methods with the original spectra for X-direction when noise is added.	40
4.11. Comparing the spectra of the two methods with the original spectra for Y-direction when noise is added.	41
4.12. Comparing the spectra of the two methods with the original spectra for Z-direction when noise is added.	41
4.13. Comparing the spectra of the two methods with the original spectra for moment around X-axis when noise is added.	42
4.14. Comparing the spectra of the two methods with the original spectra for moment around Y-axis when noise is added.	42
4.15. Comparing the spectra of the two methods with the original spectra for moment around Z-axis when noise is added.	43
4.16. Comparing acceleration spectra plus added noise at one acceleration at X-direction.	43
4.17. Comparing the spectra of the two methods with the original spectra for X-direction when noise is added.	44
4.18. Comparing the spectra of the two methods with the original spectra for Y-direction when noise is added.	45
4.19. Comparing the spectra of the two methods with the original spectra for Z-direction when noise is added.	45
4.20. Comparing the spectra of the two methods with the original spectra for moment around X-axis when noise is added.	46
4.21. Comparing the spectra of the two methods with the original spectra for moment around Y-axis when noise is added.	46

4.22. Comparing the spectra of the two methods with the original spectra for moment around Z-axis when noise is added.	47
4.23. The measured and calculated pressure in time domain when exciting in Y-direction.	48
4.24. The difference between the measured and calculated spectral density when exciting in Y-direction.	49
4.25. Showing measured pressure and comparing it to spectra calculated from measured and calculated force. Excitation is in the centre of the wheel in Y-direction.	49
4.26. Showing the measured force and the calculated force in time domain when using an excitation mainly in Z-direction.. . . .	50
4.27. Showing the ESD of the calculated Force, IFRF and LMS, and the measured force when using an excitation mainly in Z-direction.	51
4.28. Showing the measured pressure spectra and comparing it to the spectra calculated from IFRF and LMS. The force was applied in the Z-direction..	51
4.29. Showing the dB difference between the calculated pressure for LMS and IFRF when force was applied in Z-direction.	52
4.30. Showing the two time domain signals for forces in Y and Z direction. . .	52
4.31. Showing the spectra of the measured pressure and comparing it to the spectra calculated from IFRF and LMS. The force was applied in an angle at the top corner, with mainly components in Z and Y direction	53
4.32. Showing the magnitude of the dB difference between the calculated pressure for LMS and IFRF when using an excitation at the top rim, with components mainly in Z and Y.. . . .	53
4.33. Calculated time signals for forces in the X,Y and Z directions when applying a force mainly in X-direction.	54
4.34. Calculated time signals for forces in the X,Y and Z directions when applying a force mainly in Y-direction.	55
4.35. Showing the spectra of the measured pressure and comparing it to spectra calculated from IFRF and LMS when excited applying a force mainly in X-direction.. . . .	55
4.36. Showing the spectra of the measured pressure and comparing it to spectra calculated from IFRF and LMS when excited applying a force mainly in Y-direction.	56
4.37. Showing the coherence for the different channels and directions used. Top is X-direction, followed by Y and lastly Z.	57
4.38. Calculated time signals when using an excitation divided between the three directions X,Y and Z.	58

4.39. Comparing calculated spectra for LMS and IFRF with the spectra measured when exciting the structure using a force evenly distributed over X,Y and Z direction.	58
4.40. Showing the magnitude of the dB difference between the calculated pressure for LMS and IFRF when using an excitation at an angle distributed over X, Y and Z directions.	59
4.41. Comparing the calculated spectra from IFRF and LMS to the measured spectra. Calculation was carried out using three equivalent forces placed at the cube in the centre of the wheel.	60
4.42. Showing the magnitude of the dB difference between the calculated pressure for LMS and IFRF using estimated equivalent forces. Structure was excited in Z-direction.	61
4.43. Showing the magnitude of the dB difference between the calculated pressure for LMS and IFRF using estimated equivalent forces. Structure was excited in Y-direction.	61
4.44. Showing the magnitude of the dB difference between the calculated pressure for LMS and IFRF estimated equivalent forces. excitation in mainly Z and Y-direction.	62
4.45. Showing a comparison between the spectra of the measured pressure and the calculated spectras, using an excitation in mainly Y-direction.	62
4.46. Showing a comparison between the spectra of the measured pressure and the calculated spectras, using an excitation in mainly Z and Y-direction.	63
4.47. Showing a comparison between the spectra of the measured pressure and the calculated spectras, using an excitation in mainly Y-direction at the wheel centre (When cube was not attached).	64
4.48. Showing the magnitude of the dB difference between the calculated pressure for LMS and IFRF estimated equivalent forces when excited in Y-direction at the center bolt.	64
4.49. Showing the spectra of the calculated and measured acceleration for the case with a steel obstacle. Position is at subframe and in X-direction.	65
4.50. Showing the spectra of the calculated and measured acceleration for the case with a aluminum obstacle. Position is at subframe and in X-direction.	66
4.51. Showing the spectra of the calculated and measured acceleration for the case with a steel obstacle. Position is at subframe and in Z-direction.	66
4.52. Showing the spectra of the calculated and measured acceleration for the case with a aluminum obstacle. Position is at subframe and in Z-direction.	67
4.53. Showing the spectra of the calculated and measured acceleration for the case with a aluminum obstacle. Position is at body and in X-direction.	67

4.54. Showing the spectra of the calculated and measured acceleration for the case with a aluminum obstacle. Position is at body and in Z-direction.	68
4.55. Showing measured pressure and comparing it to spectra calculated from IFRF- and LMS-forces via NTFs from the spindle (Car driven over obstacle (iii) at 30km/h).	70
4.56. Showing measured pressure and comparing it to spectra calculated from IFRF- and LMS-forces via NTFs from the spindle (Car driven over obstacle (iii) at 30km/h).	70
4.57. Showing measured pressure and comparing it to spectra calculated from IFRF- and LMS-forces via NTFs from the spindle (Car driven over obstacle (ii) at 30km/h).	71
4.58. Showing measured pressure and comparing it to spectra calculated from IFRF- and LMS-forces via NTFs from the spindle (Car driven over obstacle (ii) at 30km/h).	71
4.59. Showing the coherence for the different directions used.	72
4.60. Showing measured pressure and comparing it to spectra calculated from IFRF- and LMS-forces via FRFs to the bushings and NTFs into the car (Car driven over obstacle (iii) at 30km/h).	74
4.61. Showing measured pressure and comparing it to spectra calculated from IFRF- and LMS-forces via FRFs to the bushings and NTFs into the car (Car driven over obstacle (iii) at 30km/h).	74
4.62. Showing measured pressure and comparing it to spectra calculated from IFRF- and LMS-forces via FRFs to the bushings and NTFs into the car (Car driven over obstacle (ii) at 30km/h).	75
4.63. Showing measured pressure and comparing it to spectra calculated from IFRF- and LMS-forces via FRFs to the bushings and NTFs into the car (Car driven over obstacle (ii) at 30km/h).	75

Acknowledgements

We would like to thank all involved in making this thesis, and especially, Wolfgang Kropp at Chalmers University of Technology and Fredrik Bartholdsson, Penka Dinkova and Robert Nagy at Volvo Car Corporation.

Notations

Symbols

c	Speed of sound	[m/s]
f	Frequency	[Hz]
j	Imaginary number	$j = \sqrt{-1}$
ω	Angular frequency	$2\pi f$ [Hz]
p	Pressure	[Pa]
L_p	Sound pressure level	$L_p = 20 \log_{10} \left \frac{\tilde{p}}{p_{ref}} \right $ [dB]
N	Number of samples	
I	Number of filter coefficients	
μ	Convergence factor	
ζ	Mean square error	

Signals

$x(n)$	Input signal
$d(n)$	Desired signal
$e(n)$	Error signal
$y(n)$	Output signal

Abbreviations

NTF	Noise transfer function
FFT	Fast fourier transform
FIR	Finite impulse response
FRF	Frequency response function
IFRF	Inverse frequency response function
LMS	Least mean square

1. Introduction

As fewer model cars are built during the design/evaluation process more extensive Computer-aided engineering (CAE) is required in order to make better predictions. One of the areas that need improvement is the area of impact noise modelling. The aim of this master thesis work is to study the possibility of improving VOLVO Car Corporations possibilities of modelling the noise generated when driving over minor obstacles. One of the major problems with this type of modelling is the transient nature of the problem and that it involves forces that for different reasons can't be measured.

In order to determine the forces one can use what is commonly called inverse force identification. The idea is using measured results, such as accelerations and by knowing the transfer functions of the system one can use these to estimate the excitation forces. Once the forces are known, they can be used in the model to calculate other responses, and see how different changes will impact the end result.

The thesis has looked into two main ideas of force identification, these the first being the inverse frequency response functions, IFRF. And the second is using an LMS adaptive algorithm.

Initially a virtual study is conducted of the two methods, using known transfer functions a known force is applied to create a response. From this response the forces are recreated using the two methods. This will show how well the two methods estimated the excitation force as it is known.

The other two studies were of applying a force onto a structure and estimating the impact force from the actual responses. As this requires accelerations at a number of points on the hub, measurements were conducted. These were conducted both in a test rig where the vehicle were driven over two different obstacles. The second measurements were conducted with an impact hammer.

Using the results from these measurements, forces were calculated and used to compare the two methods with the actual measurements. This in order to establish, if possible, which of the two methods is most appropriate for the type of problem.

2. Theory

2.1. The Inverse Problem

Lets first assume we have some system, for example a structure, which can be described by some model. This system is excited in some way which causes a response. We can now identify two main problems, depending on the variable we seek. The forward problem and the inverse problem:

- (i) The forward problem means that the system is excited in some way and with the help of a model one seeks the response.
- (ii) The inverse problem means that the response of the system is known and with the help of the model one seeks the unknown excitation acting on the system [5].

This thesis will mainly concern the inverse problem. The two problems are illustrated schematically in figure 2.1. The inverse problem is most often used when it is impossible to directly measure forces with force transducers. This might due to lack of space or simply because the force is acting between two structures [6].

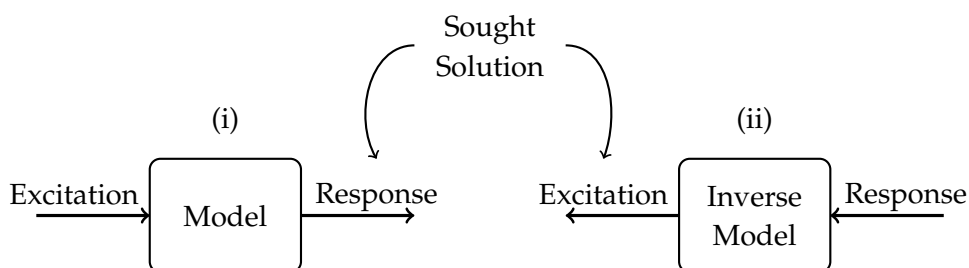


FIGURE 2.1. The direct problem (i) and the inverse problem (ii).

Solutions for the inverse problem has been around for ages, but all comes with its own set of problems. Many of these problems arise from inverting large matrices in the frequency domain, which is why many new methods strive to work in the time domain instead. This thesis aims to investigate one of these methods and its applicability to real world problems.

2.2. Force Identification

The problem of force identification is an extension of the inverse problem outlined in section 2.1. As the name suggests force identification is an inverse problem where the excitation is a force. Usually the measured response is a velocity or an acceleration of some kind. Different methods for force identification exists, and has traditionally been carried out in the frequency domain. In recent years however, several researchers have discovered the advantages of a time-domain analysis. The following sections will investigate the advantages and disadvantages of some of these methods.

2.2.1. Frequency Domain Methods

Possible frequency domain solutions to the linear system described in section 2.1 is clearly outlined by Stevens in [1], and some of it is recounted in the following. The system can be described in the frequency domain by the equation (2.1):

$$\mathbf{H}_{nm}(\omega)\mathbf{F}_m(\omega) = \mathbf{Y}_n(\omega) \quad (2.1)$$

where ω is the angular frequency and $\mathbf{H}_{nm}(\omega)$ is the $n \times m$ -sized frequency response matrix:

$$\mathbf{H}_{nm}(\omega) = \begin{bmatrix} H_{11}(\omega) & H_{12}(\omega) & \dots & H_{1m}(\omega) \\ H_{21}(\omega) & H_{22}(\omega) & \dots & H_{2m}(\omega) \\ \vdots & \vdots & \ddots & \vdots \\ H_{n1}(\omega) & H_{n2}(\omega) & \dots & H_{nm}(\omega) \end{bmatrix} \quad (2.2)$$

$\mathbf{F}_m(\omega)$ and $\mathbf{Y}_n(\omega)$ is the m -sized vector of exciting forces and the n -sized vector of responses, respectively:

$$\mathbf{F}_m(\omega) = \begin{bmatrix} F_1(\omega) & F_2(\omega) & \dots & F_m(\omega) \end{bmatrix}^T \quad (2.3)$$

$$\mathbf{Y}_n(\omega) = \begin{bmatrix} Y_1(\omega) & Y_2(\omega) & \dots & Y_n(\omega) \end{bmatrix}^T \quad (2.4)$$

$\mathbf{H}_{nm}(\omega)$ and $\mathbf{Y}_n(\omega)$ is assumed to be known and the problem becomes solving equation (2.1) with respect to $\mathbf{F}_m(\omega)$.

If $\mathbf{H}_{nm}(\omega)$ is square ($n = m$) and invertible, equation (2.1) can be inverted to obtain a solution in the form of:

$$\mathbf{F}_m(\omega) = \mathbf{H}_{nm}^{-1}(\omega)\mathbf{Y}_n(\omega) \quad (2.5)$$

where $\mathbf{H}_{nm}(\omega)^{-1}$ is the inverse of $\mathbf{H}_{nm}(\omega)$. In this case the number of responses is equal to the number of forces. In many cases however, this will not be the true. Instead the amount of forces to be determined will either be larger or smaller than the amount of measured responses. The former case is called under-determined and the latter over-determined. The over-determined system is preferred, since in this case averaging can remove some of the random errors in the system.

The solution to the over- and under-determined cases can be obtained with the so called Moore-Penrose pseudo inverse, as shown in equation (2.6).

$$\mathbf{F}_{est}(\omega) = \mathbf{H}_{nm}^+(\omega)\mathbf{Y}_n(\omega) \quad (2.6)$$

If the number of responses is larger than the number of forces there exists more than one solution. The problem then becomes to choose a force vector that fits to the already known response vector in some logical manner. There are several ways to do this, one of them is the least squares method, with which we obtain the solution to the pseudo inverse seen below.

$$\mathbf{H}_{nm}^+(\omega) = [\mathbf{H}_{nm}^T(\omega)\mathbf{H}_{nm}(\omega)]^{-1}\mathbf{H}_{nm}^T \quad (2.7)$$

where \mathbf{H}_{nm}^T is the hermitian transpose of \mathbf{H}_{nm} . Several other solutions exist, both for under- and over-determined cases, but since the main focus of the thesis is elsewhere, these will not be investigated further.

2.2.2. Single Value Decomposition

A common inversion method, used by computational software such as MATLAB, uses what is called single value decomposition. It's described in for example [18]. It uses the fact that a real $m \times n$ matrix \mathbf{A} can be decomposed on the form:

$$\mathbf{A} = \mathbf{U}\mathbf{\Sigma}\mathbf{V}^T \quad (2.8)$$

where $\mathbf{\Sigma}$ is a diagonal $m \times n$ matrix:

$$\mathbf{\Sigma} = \text{diag}(\sigma_1, \sigma_2, \dots, \sigma_p) = \begin{bmatrix} \sigma_1 & 0 & \dots & 0 & 0 \\ 0 & \sigma_2 & \dots & 0 & 0 \\ \vdots & \vdots & \ddots & \vdots & \vdots \\ 0 & 0 & \dots & \sigma_p & 0 \end{bmatrix} \quad (2.9)$$

The entries σ_p are the singular values of the matrix. \mathbf{U} is a $m \times m$ orthogonal matrix and \mathbf{V} is the transpose of a $n \times n$ orthogonal matrix examples of which is shown in equations (2.10) and (2.11), respectively.

$$\mathbf{U} = \begin{bmatrix} u_{11} & \dots & u_{1m} \\ \vdots & \ddots & \vdots \\ u_{m1} & \dots & u_{mm} \end{bmatrix} \quad (2.10)$$

$$\mathbf{V} = \begin{bmatrix} v_{11} & \dots & v_{1n} \\ \vdots & \ddots & \vdots \\ v_{n1} & \dots & v_{nn} \end{bmatrix} \quad (2.11)$$

In the case where \mathbf{A} is a square an non-singular $n \times n$ matrix \mathbf{A} can be inverted according to:

$$\mathbf{A}^{-1} = (\mathbf{U}\mathbf{\Sigma}\mathbf{V}^T)^{-1} = \mathbf{V}\mathbf{\Sigma}^{-1}\mathbf{U}^T \quad (2.12)$$

where

$$\mathbf{\Sigma}^{-1} = \text{diag}(\sigma_1^{-1}, \sigma_2^{-1}, \dots, \sigma_p^{-1}) = \begin{bmatrix} \sigma_1^{-1} & 0 & \dots & 0 & 0 \\ 0 & \sigma_2^{-1} & \dots & 0 & 0 \\ \vdots & \vdots & \ddots & \vdots & \vdots \\ 0 & 0 & \dots & \sigma_p^{-1} & 0 \end{bmatrix} \quad (2.13)$$

If \mathbf{A} on the other hand is singular or ill-conditioned the inverse of \mathbf{A} can be approximated by computing:

$$\mathbf{A}^{-1} = (\mathbf{U}\mathbf{\Sigma}\mathbf{V}^T)^{-1} \approx \mathbf{V}\mathbf{\Sigma}_0^{-1}\mathbf{U}^T \quad (2.14)$$

where

$$\Sigma_0^{-1} = \begin{cases} \sigma_p^{-1} & \text{if } \sigma_p > t \\ 0 & \text{if } \sigma_p < t \end{cases} \quad (2.15)$$

Where t is a very small value. In other words the smallest values of Σ_0^{-1} is substituted with zeroes. This somewhat remedies the fact that $\frac{1}{\sigma_p} \rightarrow \infty$ for very small values of σ_p , the cost is a certain loss of information.

2.2.3. Implementation of IFRF in MATLAB

The implementation of a IFRF method in MATLAB is very straight forward. The basic calculations are outlined in figure 2.2. Most steps does not warrant any comments, but a few things are worth mentioning about MATLABs built in functions and the consequence some of the steps have on the final result:

- (2) The function `pinv` is used, which calculates the moore-penrose pseudoinverse using SVD, mentioned in section 2.2.2. This was confirmed by calculating every step in the SVD not using built in functions, which yielded the same results.
- (4) Several impulses are cut but no windowing is applied according to the theories described in section 2.3.
- (6) The short durations of the impulses means that quite a bit of zero padding has to be used in order to get the signal the same length as the FRFs. This gives a spectra that seems to have a higher resolution than it actually have, since zero padding does not create any new information.

2.2.4. Limitations

The frequency domain method described above, although simple in its execution, comes with a number of problems. A problem widely discussed in literature is the problem of the matrix-inversion. This problem is ill-conditioned in the sense that small errors in the matrix pre-inversion might result in large errors after inversion. The primary sources for these small errors are measurement noise and errors that stem from the modeling of the system [1]. Because of the potential of these errors rendering the results meaningless, countless regularization methods, such as Tikhonov regularization, have emerged throughout the years.

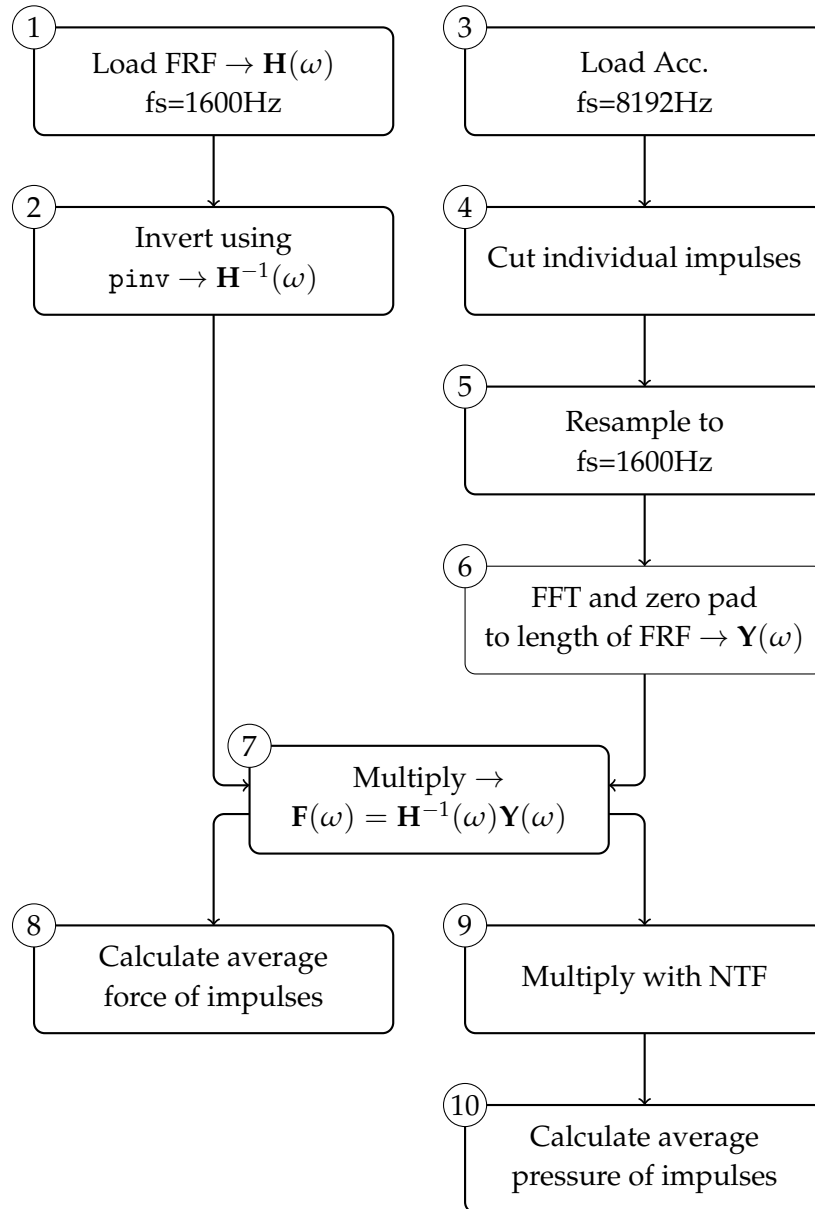


FIGURE 2.2. Rough outline of the implementation of the IFRF method in MATLAB. For further explanation of the notations used, see section 2.2.1.

2.2.5. Time Domain Methods

2.2.6. The LMS-algorithm

The use of the LMS algorithm for force identification was first presented by Kropp and Larson in [7]. The method involves a modification of the LMS-algorithm invented by Widrow and Hoff and which is thoroughly described in for example [2] and [4].

2.2.7. About the LMS-algorithm

Lets first take a look at the LMS-algorithm and how it functions. The purpose of the algorithm is to minimize the error so that the filter coefficients describes the system accurately. An adaptive algorithm is described schematically in figure 2.3, where $x(n)$ is the input signal, $d(n)$ is the desired signal and $y(n)$ is the output signal.

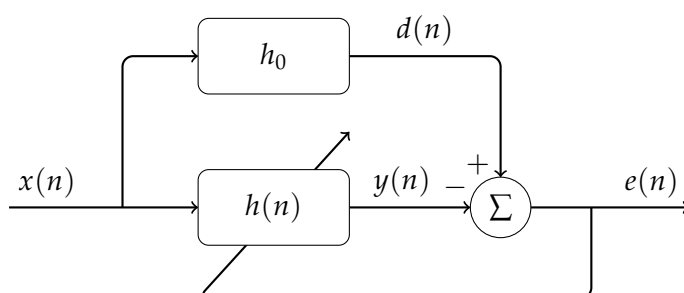


FIGURE 2.3. Block diagram of an adaptive controller.

The error signal is the difference between the output signal and the desired signal and can therefore be written as in equation (2.16).

$$e(n) = d(n) - y(n) \quad (2.16)$$

We can write the output signal $y(n)$, as:

$$y(n) = \sum_{i=0}^{I-1} h_i(n)x(n-i) = \mathbf{h}^T(n)\mathbf{x}(n) \quad (2.17)$$

where I is the length of the finite impulse response, $\mathbf{h}(n)$ is the vector containing the values of the impulse response at time step n and the input signal $x(n)$ is the input signal at time step n :

$$\mathbf{h}(n) = [h_0(n), h_1(n), \dots, h_{I-1}(n)]^T \quad (2.18)$$

$$\mathbf{x}(n) = [x(n), x(n-1), \dots, x(n-I+1)]^T \quad (2.19)$$

where T denotes the vector transpose.

The error function 2.16 can, together with 2.17 be rewritten as:

$$e(n) = d(n) - \mathbf{h}^T(n)\mathbf{x}(n) \quad (2.20)$$

The LMS function is based on the minimization of the mean square error $\zeta(n)$, which is defined as the statistical expectation of $e(n)$.

$$\zeta(n) = E [e^2(n)] \quad (2.21)$$

$$= E [(d(n) - \mathbf{h}^T(n)\mathbf{x}(n))^2] \quad (2.22)$$

$$= E [d^2(n) - 2\mathbf{h}^T(n)\mathbf{x}(n)d(n) + \mathbf{h}^T(n)\mathbf{x}(n)\mathbf{x}^T(n)\mathbf{h}(n)] \quad (2.23)$$

Clear at this point is that $\zeta(n)$ is a quadratic function dependent on the filter coefficients and the input signal. As physical system, it will be concave upward with a single minimum value. Thus, by moving down the negative gradient the optimal solution can be obtained [10]. The gradient can be found by differentiating $\zeta(n)$ with respect to $\mathbf{h}(n)$. We can therefore express the gradient as:

$$\nabla \zeta(n) = \frac{\partial \zeta(n)}{\partial \mathbf{h}(n)} = 2E \left[e(n) \frac{\partial e(n)}{\partial \mathbf{h}(n)} \right] = -2E [e(n)\mathbf{x}(n)] \quad (2.24)$$

From this we can devise an iterative method for updating the filter coefficients according to:

$$\mathbf{h}(n+1) = \mathbf{h}(n) - \mu \nabla \zeta(n) = \mathbf{h}(n) + 2\mu E [e(n)\mathbf{x}(n)] \quad (2.25)$$

were the coefficient \mathbf{h} is updated every time-step n by some amount μ . However, it is still problematic that the gradient is expressed as the ensemble average. But as shown by [3] the gradient can be estimated by substituting the function in (2.21) with $\zeta(n) = e^2(n)$ and thus, by differentiating in the same manner as shown before, we get the expression:

$$\mathbf{h}(n+1) = \mathbf{h}(n) + 2\mu e(n)\mathbf{x}(n) \quad (2.26)$$

This is, for the sake of simplicity, written as:

$$\mathbf{h}(n+1) = \mathbf{h}(n) + \alpha e(n)\mathbf{x}(n) \quad (2.27)$$

where $2\mu = \alpha$ is the convergence factor. The convergence factor controls the stability and the rate of adaption of the algorithm. It has been suggested that the optimal convergence factor can be determined by setting the constraints shown in equation (2.28) [7].

$$0 < \alpha < (IE [x^2(n)])^{-1} \quad (2.28)$$

2.2.8. The LMS-algorithm as a Force Identification Method

In order to use the LMS-algorithm for force identification, it needs to be modified slightly. Instead of seeking to model an impulse response, we now seek the input signal, i.e. the force applied to a certain structure.

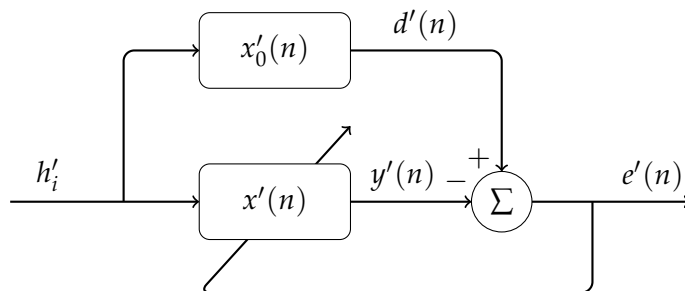


FIGURE 2.4. Block diagram of a modified controller.

Since convolution is commutative the input vector $\mathbf{x}(n)$ and $\mathbf{h}(n)$ in equation (2.17) can be interchanged. Updating equation (2.25), we thus obtain:

$$\mathbf{x}(n+1) = \mathbf{x}(n) - \mu \nabla \xi(n) = \mathbf{x}(n) + 2\mu E [e(n)\mathbf{h}(n)] \quad (2.29)$$

In section 2.2.6 it was shown that the ensemble average could be substituted with the instantaneous value, and eventually the system would converge towards a minimum value. In this case however, this process is problematic. At time n the values of (2.30) are updated and at time $n+1$ the values of (2.31) are updated (and so forth).

$$\mathbf{x}(n) = [x(n), x(n-1), \dots, x(n-I+1)]^T \quad (2.30)$$

$$\mathbf{x}(n+1) = [x(n+1), x(n), \dots, x(n-I+2)]^T \quad (2.31)$$

Thus the input values can only be updated I times. It is unlikely that this is sufficient in order to allow the system to converge to its optimal value. To remedy this constraints (i) and (ii) are introduced:

- (i) Only N values of the input signal $x(n)$ and the desired signal $d(n)$ is considered.
- (ii) The series of filter coefficients are assumed to be periodic with the period length N . This is also true for the desired signal $d(n)$.

The final expression for the modified LMS-algorithm becomes:

$$\mathbf{x}(n+1) = \mathbf{x}(n) + 2\mu e(n)\mathbf{h}(n) \quad \text{for } I \leq n \leq N \quad \forall \quad N \geq 2 \cdot I \quad (2.32)$$

where

$$e(n) = d(n) - \sum_{i=0}^{I-1} x(n-i)h(i) \quad (2.33)$$

The constraint $N \geq 2 \cdot I$ is necessary since the first I values of $d(n)$ are influenced by values of $x(n)$ outside the observation window $[0, \dots, N]$. As a consequence the first I values will be inaccurate. This is illustrated by figure 2.5. To use the LMS-algorithm for force identification, one needs to make sure that the area of interest is outside this area.

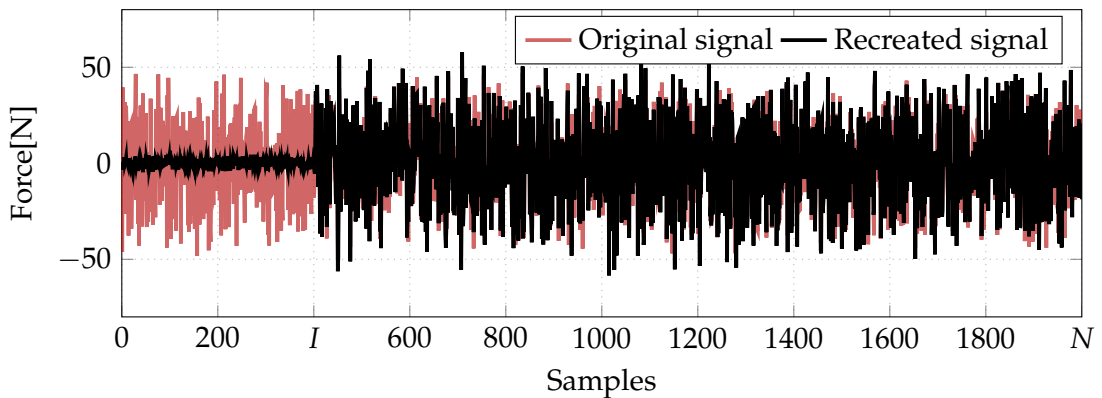


FIGURE 2.5. Example of the original force and the force recreated by an LMS-algorithm.

As in previously described cases, μ need to be under certain constraints in order to ensure stability and a sufficient rate of adaptation. The following constraints has been suggested as suitable:

$$0 < \mu < \left(\sum_{i=0}^{l-1} |h(i)|^2 \right)^{-1} \quad (2.34)$$

This is the constraint used throughout the work carried out in this thesis, although others exists.

In order to estimate how well the algorithm has converged and create a stopping criteria for the algorithm one can set up a relative error according to [7]:

$$e_{rel} = \frac{\sum_{i=L+1}^N e(n)^2}{\sum_{i=L+1}^N d(n)^2} \quad (2.35)$$

Where N is the total length of the segment studied and L signifies the length of the impulse response.

2.2.9. Implementation of LMS method in MATLAB

The LMS algorithm can easily be implemented in MATLAB. The basic steps are outlined in figure 2.6 and further explanations of some of the steps involved are listed below:

- (3) How the step size is calculated depends on the type of system investigated. Depending on the number of responses the step size can be calculated either according to equation (2.34) or (2.38).
- (4) An in-signal $\mathbf{y}(n)$ is calculated for every force and moment taken into account.
- (8) An individual error signal $\mathbf{e}(n)$ is updated for each force and moment.
- (9) Since the force can't be updated for an infinite time, conditions for terminating the iteration process is set. These conditions can either be that the error, $\mathbf{e}(n)$, is sufficiently small or that the number of iterations are high enough that no additional improvement can be expected.
- (10) The manner in which the force is updated varies depending on the type of system. For a SISO system the force is updated as described as in section 2.2.8. With several

outputs the force is updated according to equation (2.37), where an average of the resulting error is taken.

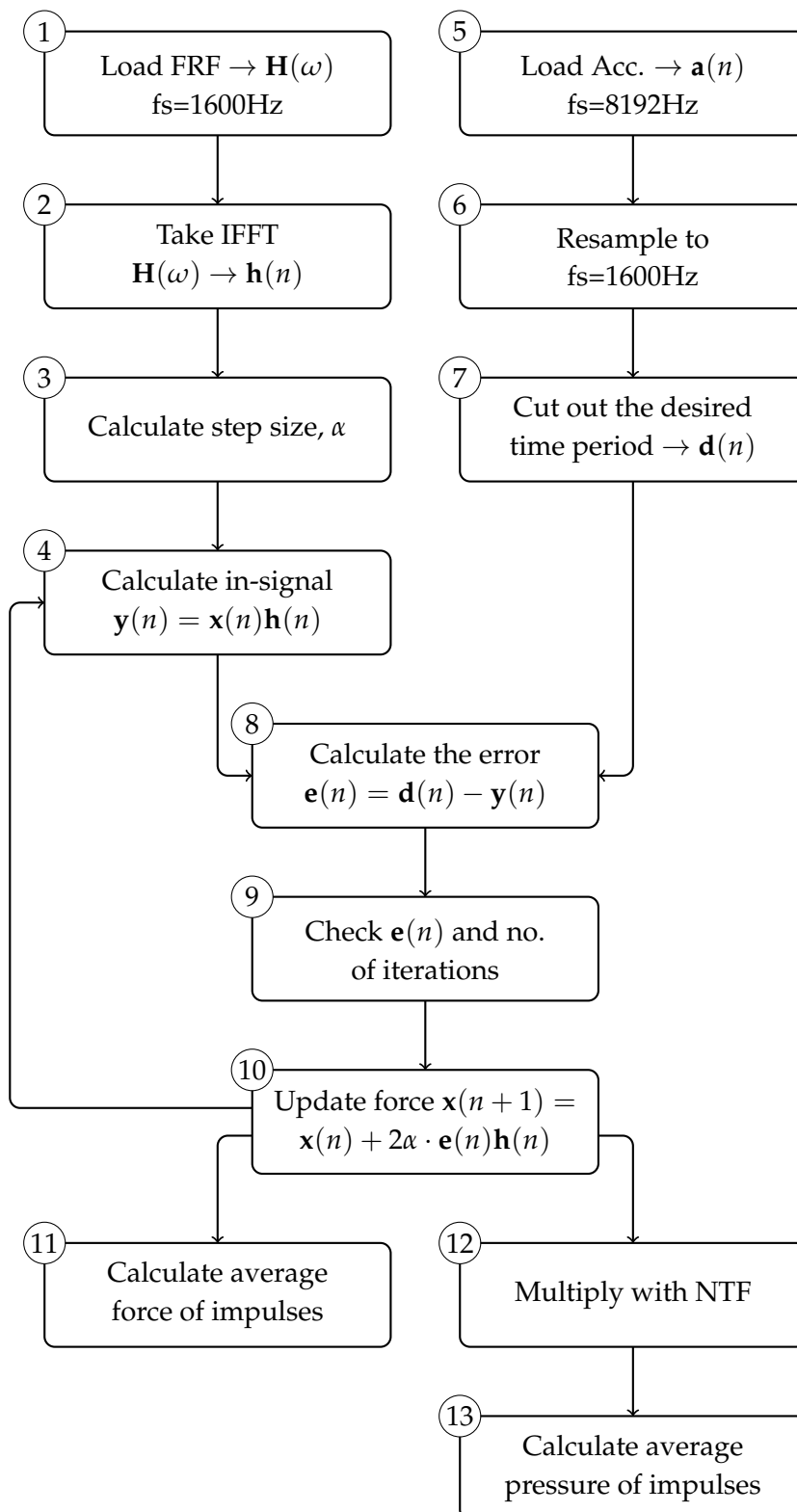


FIGURE 2.6. Rough outline of the implementation of the LMS method in MATLAB.

2.2.10. MISO-System

When the tyre hits an obstacle, the system will have not one but two points of excitation. And what's more is that at each point the impact force will consist of the forces acting in X,Y and Z direction and the moments acting around each of these axes. This calls for an LMS algorithm which can handle the multiple input - multiple output system, MIMO. We start by using the algorithm for the single input single - output system, SISO. If we study one point of excitation and one force we will have the system previously shown in figure 2.4.

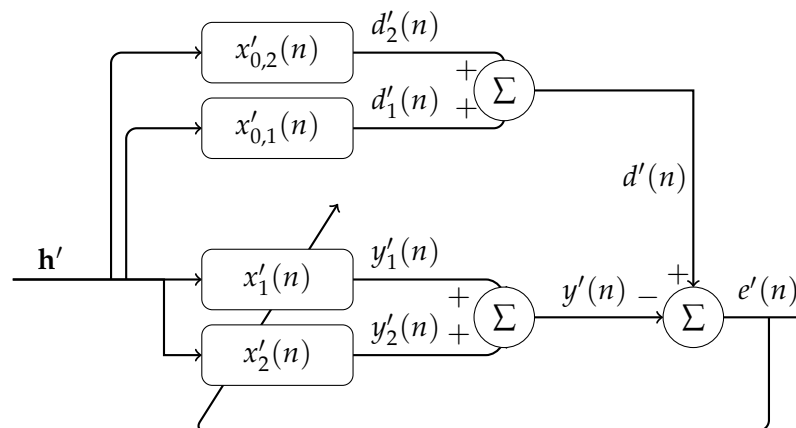


FIGURE 2.7. Block diagram of a MISO system.

If another force is added we will get the system in figure 2.7. The difference in the algorithm will be that the two forces both contribute to the response at that position. Which in turn means that the error calculated is dependent on both these forces, and in order to calculate the excitation forces, this has to be related to the two forces somehow. The relation is found in the impulse responses belonging to each force - response path. So in order to calculate the result one simply has to multiply the error with the corresponding impulse response and stepsize according to 2.36. The stepsize is calculated like before in 2.34.

$$F_m(n) = F_m(n) + e(n)\mu_m h(i); \quad m = 1,2; \quad (2.36)$$

2.2.11. SIMO

From this it is clear that the algorithm is easily adapted to handle multiple input systems. But there is still a need to relate multiple input to multiple output, in order to clarify

how this is done one can continue with studying a system for single input - multiple output, SIMO. One such system is shown in figure 2.8.

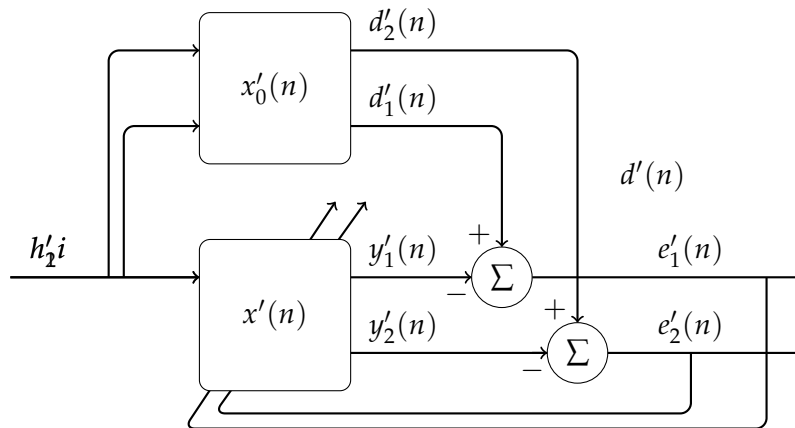


FIGURE 2.8. Block diagram of a MISO system.

The excitation will influence the two response positions, and two separate errors will be found. Now one needs to relate these errors to the calculation of the excitation force, which will be similar to the process in a SISO system, where the excitation is found by relating the error to the impulse response and step size. Now however the errors are multiplied with the corresponding impulse responses and then an average is formed, so we get the average force exciting this position see equation 2.37.

$$F(n) = F(n) + \mu \cdot \sum_{m=1}^{m=M} e_m h_m \frac{1}{M} \quad (2.37)$$

where M is equal to the total number of response positions. But in order to do this properly, the step-size is calculated as an average from the impulse responses according to equation 2.38 described by [7].

$$\mu = M \left(\sum_{m=1}^M \sum_{i=0}^{I-1} |h_m(i)|^2 \right)^{-1} \quad (2.38)$$

where M is equal to the total number of response positions and I is the filter length, i.e. the number of samples in the impulse response. h denotes the value of the filter coefficients at each time sample.

2.2.12. MIMO

With the algorithms for SIMO and MISO ready, an algorithm for a MIMO system can be formed. For each of the exciting forces F_n , there is a response at position m d_{nm} . Linearity is assumed so that the response d_m from all forces at response position m , is equal to the sum of the responses d_{nm} from each of the exciting forces. At each of the response positions there will be an error e_m that is the error between the measured signal y_m , and the calculated response d_m .

The block diagram for a 2 input. - 2 output system is shown in figure 2.9, it already becomes a complicated system when illustrating with block diagrams.

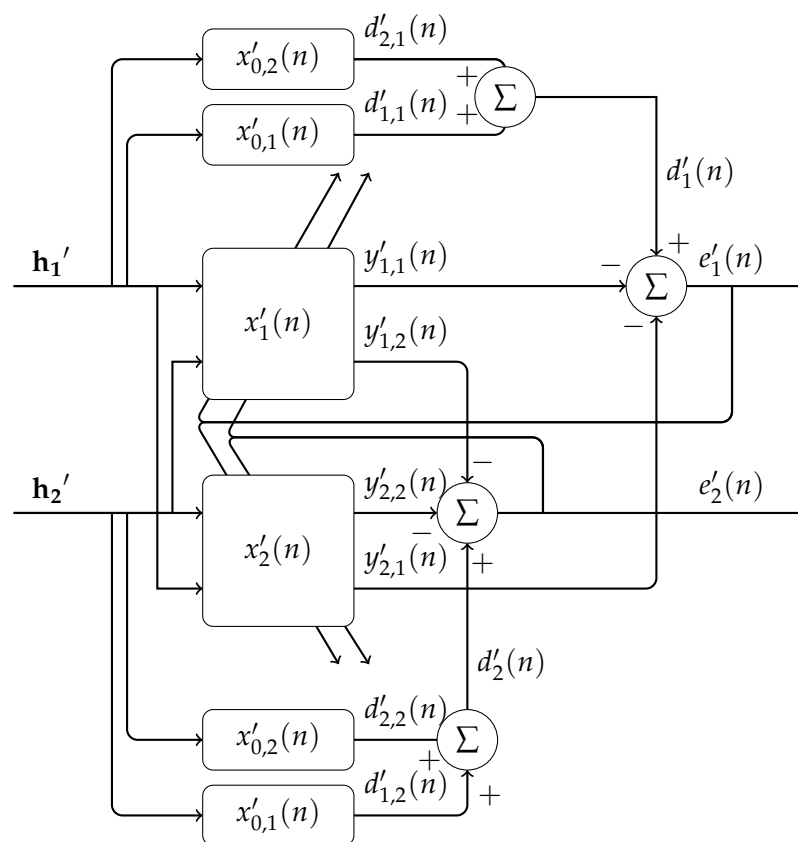


FIGURE 2.9. Block diagram of a MIMO system.

Using the error signal at all positions, the forces of excitation can be calculated by relating the error at the response position, to the impulse response belonging to the excitation position - response path. This is the correction of the force at time instance n . For a MIMO system this will yield several corrections, and by averaging these and multiplying with the step size, the new force estimate at time instance n can be calculated according

to equation 2.37.

Once calculated this procedure is repeated for the next time sample, over the whole interval of interest. In order for the algorithm to converge, the process needs to be repeated over the same interval for a number of iterations, this in order to reach a convergence.

2.3. Short on transients

Before leaving for the section concerning simulations, some short information regarding transients and the analysis of such will be brought up. A transient signal is as the name suggests transient, that is, it disappears within some given time. The measurable duration of the signal will depend on the system in which it is measured. The amount of damping in the system is one important parameter deciding how long the transient is noticeable. As with any signal, theoretically speaking the energy will remain in the system for an infinite time.

But that energy is of no interest since it will neither be measurable nor give rise to any vibrations or sound. This happens as soon as the levels are beneath the noise floor, another important aspect. In order to observe the transient, it has to be above the noise floor.

2.3.1. Windowing and the ESD

While studying random or periodic processes it is common to analyse the power spectral density, or PSD. The procedure is generally as follows: N consecutive samples of the signal is chosen. This sequence of the signal usually ends at a discontinuity at the end, and to avoid the effects of leakage a window is applied. After which the FFT is taken over the length of the segment, after which the components of the FFT are scaled accordingly.

$$S_{xx}(n) = S_p |X(n)|^2 \quad (2.39)$$

$$G_{xx}(n) = \begin{cases} S_{xx}(n) * 2 & \text{if } n = 1, 2, \dots, N/2 \\ S_{xx}(n) & \text{if } n = 0 \end{cases} \quad (2.40)$$

Where $X(n)$ is the Fourier transform of the segment, S_{xx} is the double sided spectra and G_{xx} is the single sided spectra. S_p is a window correction factor that is applied in order

to compensate for the applied window. According to Brandt [17], there are problems using the Welch's estimation described above, especially when dealing with entirely random signals, however as the focus in this thesis is on transient signals, this discussion is not something that will be delved into.

Instead let us consider a transient signal, dealing with impact, it will consist of one or more peaks and decay after some given time, t_{decay} . After this time and before the time of impact there will be the noise floor, if the energy of the transient signal is assumed to be well above the energy of the noise floor, the levels of the spectral components of the signal will not be affected much by this noise.

This will in turn mean that there is no need for any windowing, as the leakage will be small in comparison to the energy in the transient. But it is still important to make sure that at the truncation the levels are, if not zero, very close to zero. While handy, this poses a problem when analyzing the spectral components.

Due to the limited duration, there will only be a limited number of samples describing the transient. While one could add an infinite amount of samples to the signal, the frequency resolution of the signal will not be increased. While it may appear that this is the case, one is merely interpolating the samples in between the original, low resolution estimation.

While the PSD is used for periodic or random signals, the ESD, energy spectral density, is used for transient signals. The ESD is similar to the PSD but the main difference is the scaling. The scaling is performed according to Brandt [17] as shown in equations 2.41 and 2.42.

$$S_{xx}(n) = \frac{T}{\Delta f} \left| \frac{X(n)}{N} \right|^2 = (\Delta t)^2 |X(n)|^2 \quad (2.41)$$

$$G_{xx}(n) = \begin{cases} S_{xx}(n) * 2 & \text{if } n = 1, 2 \dots N/2 \\ S_{xx}(n) & \text{if } n = 0 \end{cases} \quad (2.42)$$

where T signifies the period time, Δf is the frequency resolution, Δt is the time resolution and N is the amount of samples. S_{xx} is the double sided spectra and G_{xx} is the single sided spectra.

One of the big advantages is of course that zero padding the transient is nothing that will alter the spectra, as the energy will be unaffected by such operations.

2.4. Defining a System of Coordinates

Throughout this thesis, when investigating the forces acting upon a tyre a certain system of coordinates is used. In this system the zero point for each axis is in the absolute center of the tyre. Assuming a horizontal ground surface, the z-axis is perpendicular to the ground plane, the x-axis is parallel to the ground plane and its positive end pointed towards the driving direction and the y-axis is also parallel to the ground plane but perpendicular to the x- and z-axis. The directions relative to a tyre can be seen in figure 2.10.

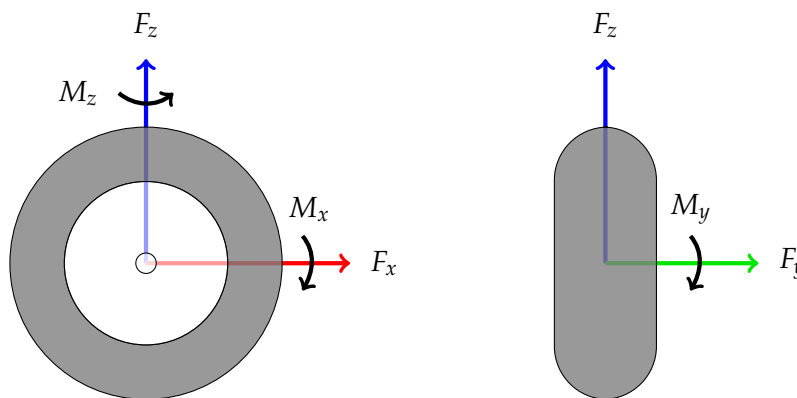


FIGURE 2.10. Definitions for the forces and directions.

From these coordinates we can decompose the forces and moments acting on the tyre into three distinct forces and three moments [14]:

- F_x - Longitudinal force - The force acting along the x-axis opposite the driving direction.
- F_y - Lateral force - The force acting along the y-axis in the direction from the front right wheel to the left.
- F_z - Normal force - The force acting along the z-axis in the direction from the ground plane.
- M_x - Roll moment - The moment about the x-axis.
- M_y - Pitch moment - The moment about the y-axis.
- M_z - Yaw moment - The moment about the z-axis.

These can then be used to characterize the excitation of the tyre during some process. The definitions of these forces will be the same throughout the thesis, both when looking at forces acting on tyres and at other points on the car.

2.5. Noise Generation

Mechanisms generating noise from vehicles are abundant, and ranges from friction noise to aerodynamic noise. In this thesis however, the structural vibrations caused by road discontinuities are of primary importance, therefore the focus is on the noise generation processes crucial in that specific case.

2.5.1. Wave Propagation in Tyres

Three kinds of waves can be identified when a tyre is excited: the first wave type is acting as a membrane wave at low frequencies and as a bending wave at slightly higher frequencies. The second is a longitudinal wave. The third wave type is what is referred to as a rotational wave. This is a wave where the layers of the tyre is moving out of phase [13]. These waves are illustrated in figure 2.11.

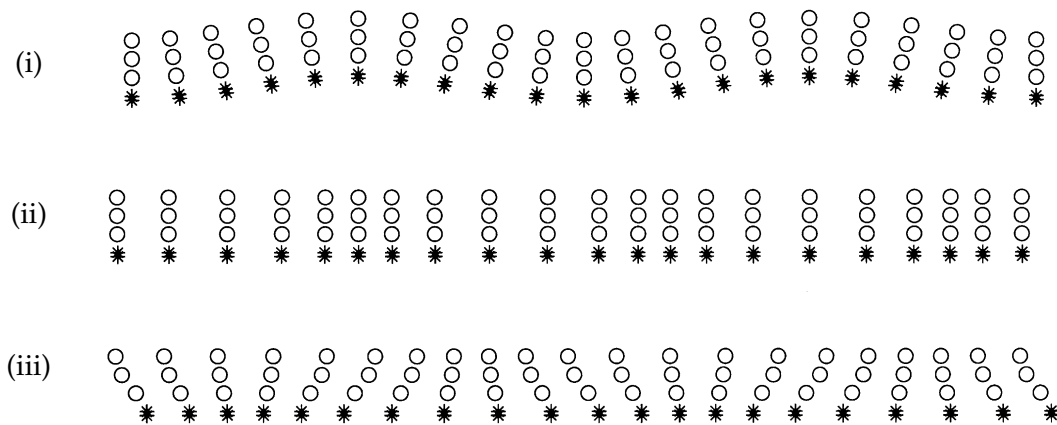


FIGURE 2.11. Wave types propagating on a tyre: Bending wave (i), longitudinal wave (ii) and rotational wave (iii) (Taken from [13]).

At certain frequencies there will be constructive interference from waves traveling in different directions. This will cause standing wave patterns on the tyre. Circumferential resonances appear when the circumference of the tyre equals an integer n times the wavelength λ . This modal behavior appears mainly below 500Hz. At higher frequencies, the high damping of the tyre causes waves propagating from the excitation point to decay quickly, thus preventing standing wave patterns [12].

For the purpose of future analysis it is useful to identify the first few modes of the wheel. The exact frequency at which these occur varies from wheel to wheel and from

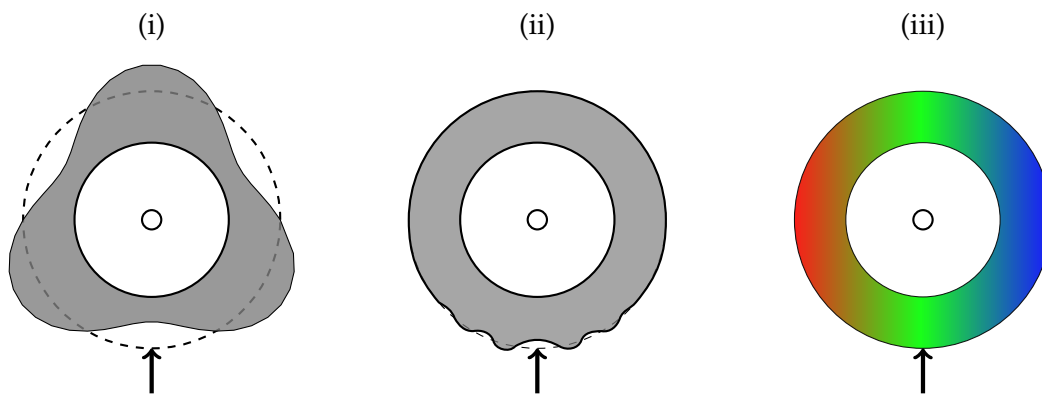


FIGURE 2.12. Modal (i) and non-modal (ii) behavior of a tyre. (iii) shows the cavity resonance of the cavity and \uparrow denotes the point of excitation.

circumstance to circumstance and depending on excitation some modes will not be present. Hopefully however, a general behavior can be established. For the sake of understanding, let's look at a unconstrained case first, i.e. where the wheel is freely suspended and not constrained by the road. The naming convention in the following text is taken from [12].

The first few modes are rigid. In other words, there is no deformation of the belt, but the tyre vibrates around one of its axes. Four rigid modes can be identified:

- (i) The axial mode: The tyre vibrates rigidly along the y-axis.
- (ii) The torsional mode: The tyre vibrates rigidly around the y axis.
- (iii) (1,0)-mode: The tyre vibrates rigidly in the zx-plane.
- (iv) (1,1)-mode: The tyre vibrates rigidly around the z-axis in the zx-plane.

These modes differ slightly when constrained by a road surface. The constraint makes the axial mode ((i)) impossible, and will cause these modes to change. At what's called the (1,1) horizontal and (1,1) vertical modes the tyre mainly rotates around the y and z-axis, respectively. At the (1,0) horizontal and (1,0) vertical modes the tyre mainly vibrates along the x and z axis, respectively. When the tyre is constrained by the road, the tyre will show effects of torsional motion around the y axis at the (1,0) horizontal mode.

The frequencies at which these occur will obviously differ greatly between different car models and tyres. In [12] the frequencies at which the first constrained modes occur for a particular model is at 52, 65, 82 and 98 Hz.

2.5.1.1. Cavity Resonance

The structural vibrations on the tyres are also coupled with the pressure inside the tyre cavity. At certain frequencies, just like on the surface of the tyre, constructive interference will occur within the tyre cavity, creating standing wave patterns. The very first cavity resonance usually occurs around 200-250Hz for a passenger car tyre. This resonance is significant for the structural vibrations transmitted into the car. The higher cavity resonances are less significant for transferring vibrations into the car. The very first resonance can be seen on figure 2.12.

Thomson [15] presented a simplified model for the air cavity in an undeflected tire that assumes that it can be modeled as a unwrapped torus at low frequencies where the wavelength is much larger than the cross section of the cavity. Also assuming that the cavity is rigid, an estimate of the first cavity resonance can be calculated according to:

$$f_c = \frac{c}{L_c} = \frac{2c}{\pi(D + d)} \quad (2.43)$$

where c is the speed of sound and L_c is the median length of circumference for the cavity, d is the inner diameter of the cavity and D is outer diameter of the cavity. This method works well up to the point where the wavelength becomes the length of the cross-section.

As one wave travel in the rolling direction and another in the opposite direction, the doppler effect causes this resonance to split into two resonances. In other words the two resonances are calculated by putting $c = c \pm c_R$ in equation (2.43), where c_R is the rolling speed [11].

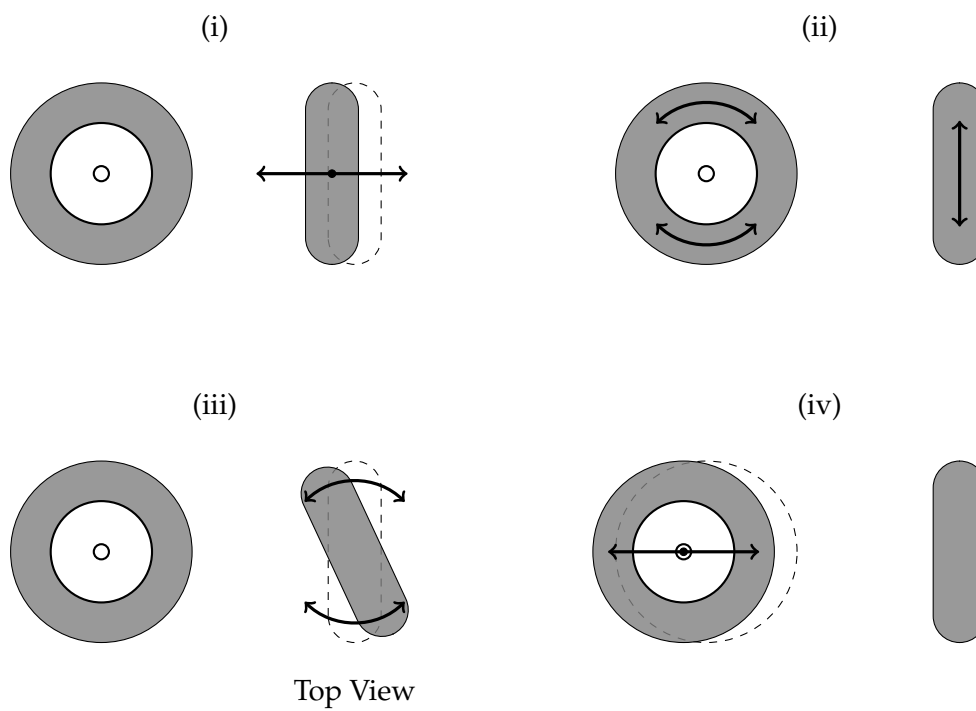


FIGURE 2.13. The four first modes of an unconstrained tire.

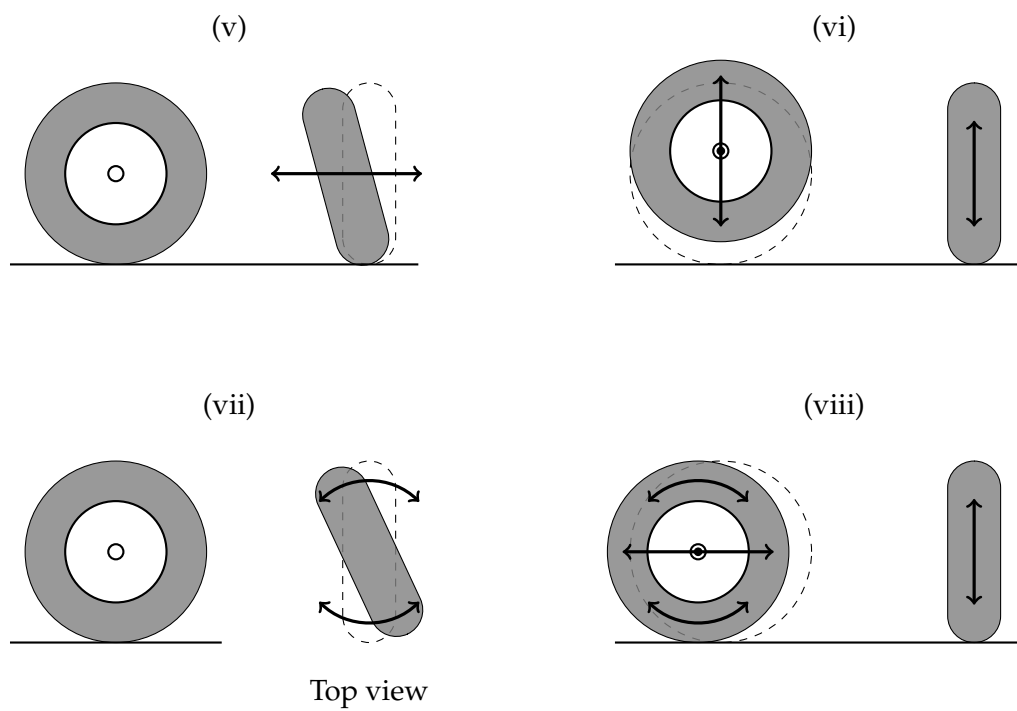


FIGURE 2.14. The four first modes of a tire constrained by a road surface.

3. Measurements

Measurements were conducted at Volvo PV in Torslanda, Sweden. The purpose of the measurements were to investigate the structural response of a car to minor obstacles.

3.1. Drum Measurement Setup

To investigate the response to minor obstacles while avoiding the influence of other noise sources such as wind noise, road noise, engine noise and so forth, a method using a laboratory drum facility were used. The facilities used consists of two smooth steel drums mounted underneath an acoustically isolated floor in a semi anechoic chamber. The drums have diameters of 1.6 meters and are driven by an electric motor located underneath the floor.

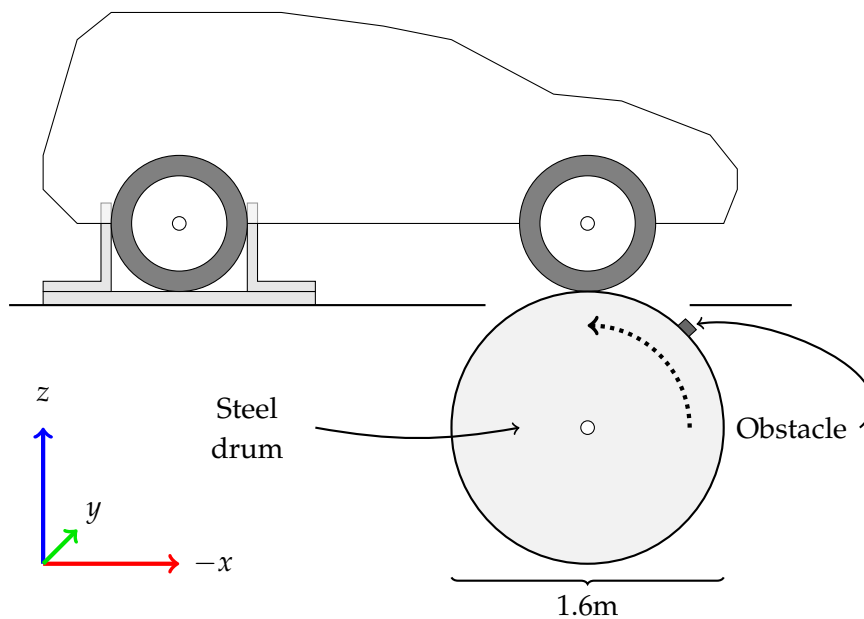


FIGURE 3.1. The setup of the measurements conducted at Volvo PV.

During the measurements the front wheels of the car is placed on the steel drum while

the the rear wheels are clamped still. The front wheels are driven by the steel drum with the car engine turned of in order to avoid other influence than that of the tires. A basic sketch of the setup can be seen in figure 3.1.

To investigate the influence of road discontinues, small obstacles were mounted on the steel drum. The measurements were conducted using obstacles of different shapes and sizes in order to investigate the influence of various excitations. The different obstacles, labeled (i) to (iii), can be seen in figure 3.2. Out of these (i) and (ii) are made out of steel while (iii) is made out of aluminum.

To investigate the structural response to different driving speeds, the steel drums were driven at 1, 5, 10, 15, 20, 25, and 30 km/h. Higher speeds were not possible, because of the limited circumference of the drum. At higher speeds the impulses bled into each other, partly ruining them.

The tires used during the measurement were of the model 275/45R20 manufactured by Michelin. According to standard notation 275 is the width of the tire, 45 is the ratio between the height and the width of the tire expressed in percent, R denotes a radial tire and 20 is the rim diameter in inches [14]. The tire was inflated to a pressure of 2.4 bar.

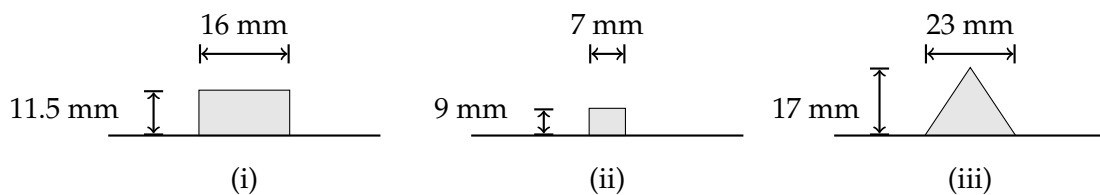


FIGURE 3.2. Obstacles used in measurements.(i) and (ii) are made out of steel while (iii) is made out of aluminum

3.1.1. List of Equipment

The following equipment were used during the measurements:

- 12 tri-ax PCB accelerometers model HT356A15 [10mV/g]
- 1 Laptop containing LMS measurement system.
- Scadas Mobile 40 channel front end
- 2 Microphones Brüel & Kjær model 4189-A-021
- Cables

3.1.2. Notes About the Method

Measurements conducted in a lab environment such as described above, will obviously differ somewhat from measurements conducted in a more realistic situation. The primary advantage of a laboratory environment is the possibility to repeat the conditions of the measurements.

An obvious advantage of a drum method is the possibility to exclude most unwanted noise sources such as wind noise and engine noise. Since the surface of the drum is almost completely flat the influence of road noise can be excluded as well. Therefore, the signal of the obstacle passing underneath the tire can be measured without much unwanted noise. On the other hand noise from the motor driving the drum might influence the measurements and this needs to be accounted for. It is however unlikely that this will influence velocity measurements in any significant way.

One disadvantage of mounting obstacles on a steel drum is that the angle of excitation and the pressure distribution on the tire will be slightly different than if mounted on non curved surface. Part of the procedure involves attaching straps in order to keep the car from rolling away, which in turn will alter the actual forces of the impact. As such the forces acting in a tire in a real world situation is therefore expected to differ somewhat from the forces acting on the tire driven by the steel drum.

3.1.3. Measurement Points

Measurements were made using accelerometers at a variety of points on the car. Measurements of the spindle accelerations were made at four points: Knuc:291, knuc:292, knuc:293 and knuc:294. The positions of these can be seen in figure 3.3. The point on the knuckle are the ones most referenced throughout the thesis, but measurements were made at 6 more points. All measurement points are listed in table 3.1.

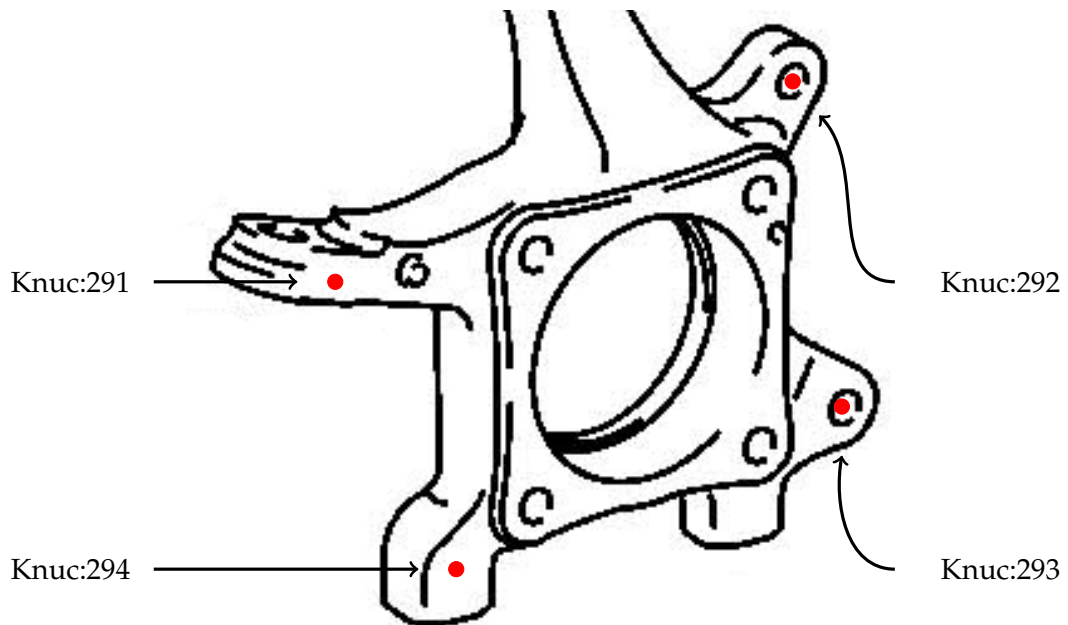


FIGURE 3.3. Accelerometer positions on the knuckle. The positions of the accelerometers are indicated by ● (Modified from [19]).

TABLE 3.1. List of measurements positions used during the measurements.

Position no.	Position name	Description
1	Knuc:291	See figure 3.3.
2	Knuc:292	See figure 3.3.
3	Knuc:293	See figure 3.3.
4	Knuc:294	See figure 3.3.
5	Body:202	At bushing connecting body and subframe.
6	SubF:202	At the subframe close to the bushing.
7	Body:241	At the Bushing connecting the top of the front shock absorbers with the body.
8	Strut:241	At the top of the shock absorber.
9	Steering wheel	Accelerometer mounted at the very top of the steering wheel.
10	St:11	Accelerometer mounted beneath the driving seat.

3.2. Impact Measurements

In order to study calculated responses without the influence of bias from simulated frequency response functions, measurements were conducted with an impact hammer.

3.2.1. Impact Measurement Setup

The setup was as follows, four accelerometers were placed at positions at the knuckle. The placement was specified out of the centre of the wheel, with one accelerometer in each quadrant of the x - z plane. Another accelerometer was placed on a bolt connecting the subframe with the body with the last accelerometer placed at the connection between seat and body.

In addition one microphone was placed in the compartment, at the position of the drivers left ear. The devices were connected to the front end which was placed in the righthand back seat of the compartment. The positions of the accelerometers and the microphone are marked in figure 3.4.

In order to enable measurement of transfer functions in three separate directions, a cube of aluminum was glued onto the bolt at the centre of the wheel. This can be seen in figure 3.6.

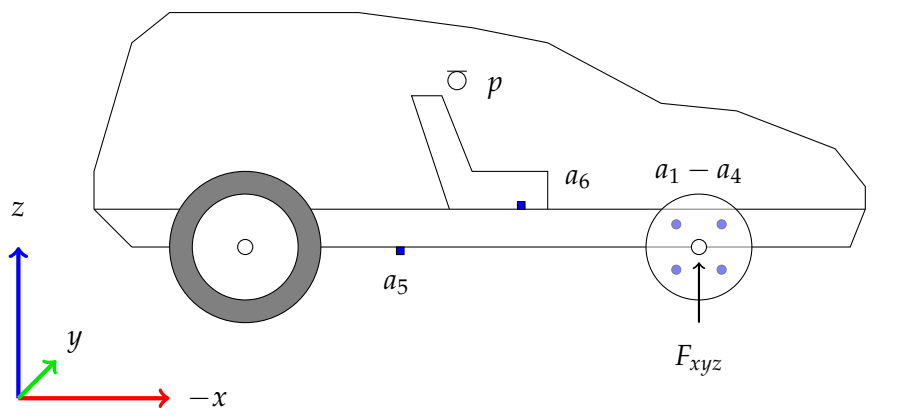


FIGURE 3.4. Approximate locations of accelerometers ($a_1 - a_6$) and microphone (p) during measurements. Also marked in the figure is the approximate position of the excitations (F_{xyz}).

The FRFs and NTFs are determined by well known relations seen in equations 3.1 and 3.2, respectively.

$$\mathbf{H}(\omega) = \frac{\mathbf{Y}_n(\omega)}{\mathbf{F}_n(\omega)} \quad (3.1)$$

$$\mathbf{H}(\omega) = \frac{\mathbf{P}(\omega)}{\mathbf{F}_n(\omega)} \quad (3.2)$$

where \mathbf{Y}_n and \mathbf{P} are the responses from the accelerometers and the microphone, respectively.

3.2.2. List of Equipment

The following equipment were used during the measurements:

- 6 tri-ax DYSTRAN accelerometers model 3023M23 [10mV/g]
- 1 Laptop containing LMS Impact measurement system.
- Scadas Mobile 40 channel front end
- 1 Microphone Brüel & Kjær model 4189-A-021
- 1 Impact Hammer Brüel & Kjær [0.21mV/N]
- Cables

3.2.3. Measurements

Using the impact hammer and tapping the cube, the transfer function for a force acting in X,Y and Z direction was measured. A total of 20 averages was collected for each direction. The response was measured with a sampling frequency of 4096 kHz and a frequency resolution of 0.5 Hz.

Once the transfer functions were measured, using the impact hammer, a number of impulses and the responses at different positions was measured. The response to a force in X,Y and Z direction was measured as well as different combinations of these directions, e.g. tapping in the corner exciting the different directions somewhat evenly or at a side with a 45 degree angle.

In addition, due to problems with coherence, measurements of transfer functions was measured at three more positions. One was in the Y direction of the hub centre, without the cube, marked as y_2 in figure 3.5. The other two was at the top of the wheel disc, in Y and Z direction, marked as y_1 and z_1 in figure 3.5. Like previously the impact hammer was used to create different impulses at the positions.

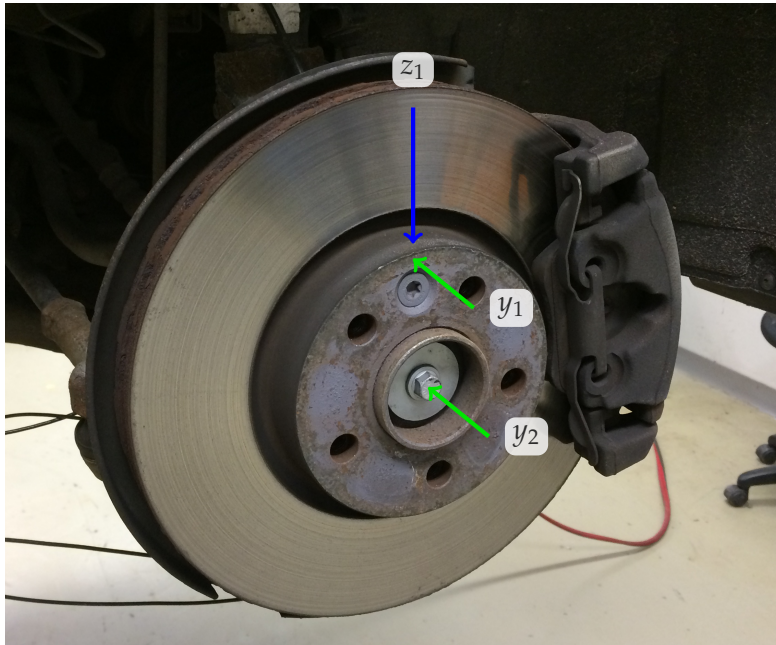


FIGURE 3.5. Picture showing the locations where transfer functions were measured and in which direction the force was applied.

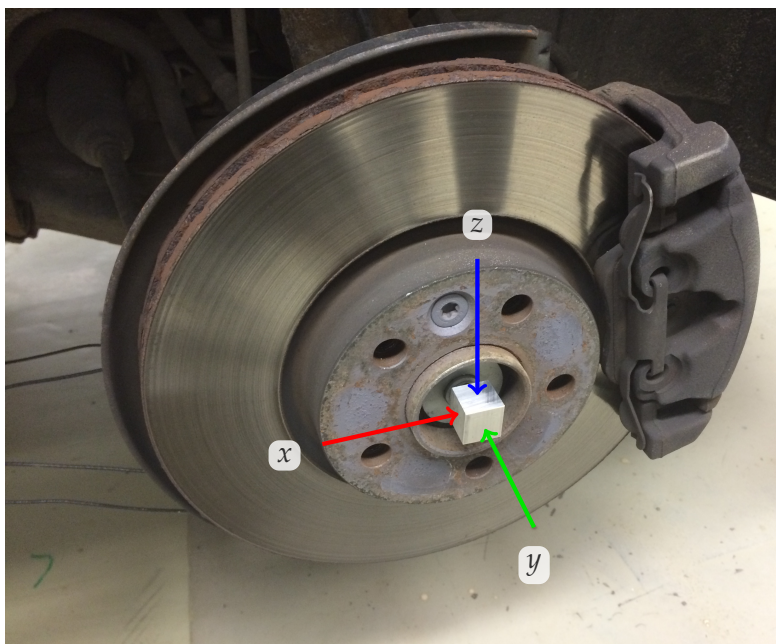


FIGURE 3.6. Illustrating the cube and from where and in which directions the transfer functions were measured.

4. "Simulations"

Several simulations were conducted over the course of the thesis, starting with very simple simulations. The first simulations were conducted using known input forces, combining sinusoidals and exponential functions, and using these to create acceleration responses. These results showed great promise and the work was carried on to analyse results from actual measurements.

4.1. Virtual Simulation

As an illustration of how the two methods compare, a virtual study will follow. Using forces estimated from a measurement on the drum with a cleat fastened on the right hand side. In the simulation a total of 3 forces are applied together with 3 moments. Using this excitation accelerations were calculated at 4 tri-axial accelerometer positions.

Then using the same transfer functions and these simulated accelerations, the forces were calculated using the IFRF method and the LMS algorithm. Two cases are studied, one using the unaltered signal and one using the signal with 5% noise added. The noise was estimated from the largest impulse, using 5% of the RMS amplitude and multiplying it with a random signal. The modified signal can be seen with the original signal in figure 4.1.

4.1.1. Verification of Method

Studying the signal with no noise, it is apparent that the LMS algorithm is very capable of finding the original excitations. The main differences exist in the weaker signals and at some frequencies, and in the moment around Z-axis. It is apparent from the figures 4.2 - 4.3, that the estimation in time domain is very accurate. The relative error, calculated using equation 2.35, is less than 0.2%. However, studying the spectra in figures 4.4 - 4.9 it is apparent that despite this, there are large differences at certain frequencies. This was found by M. Sturm et. al [9].

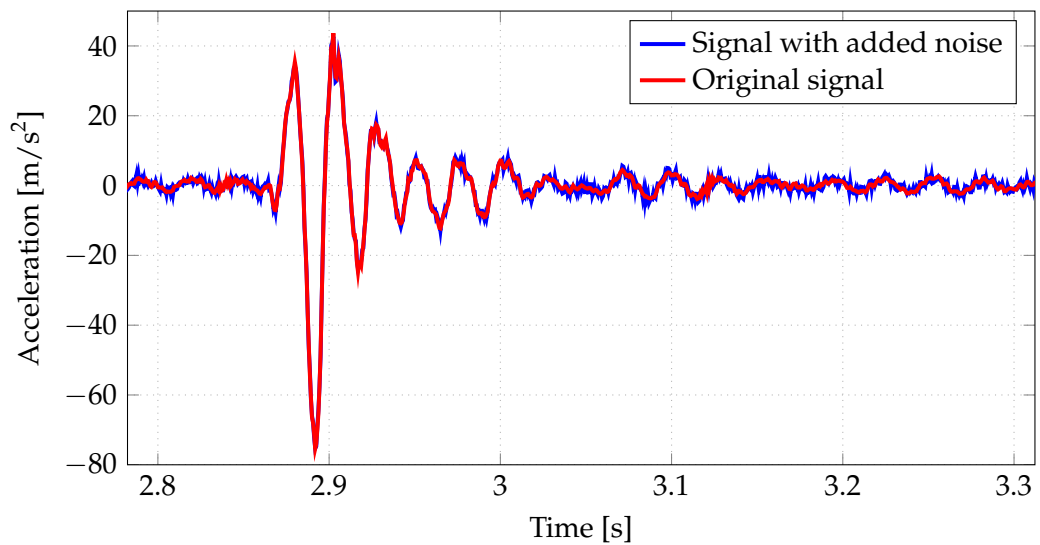


FIGURE 4.1. Original signal plotted with the signal with added noise.

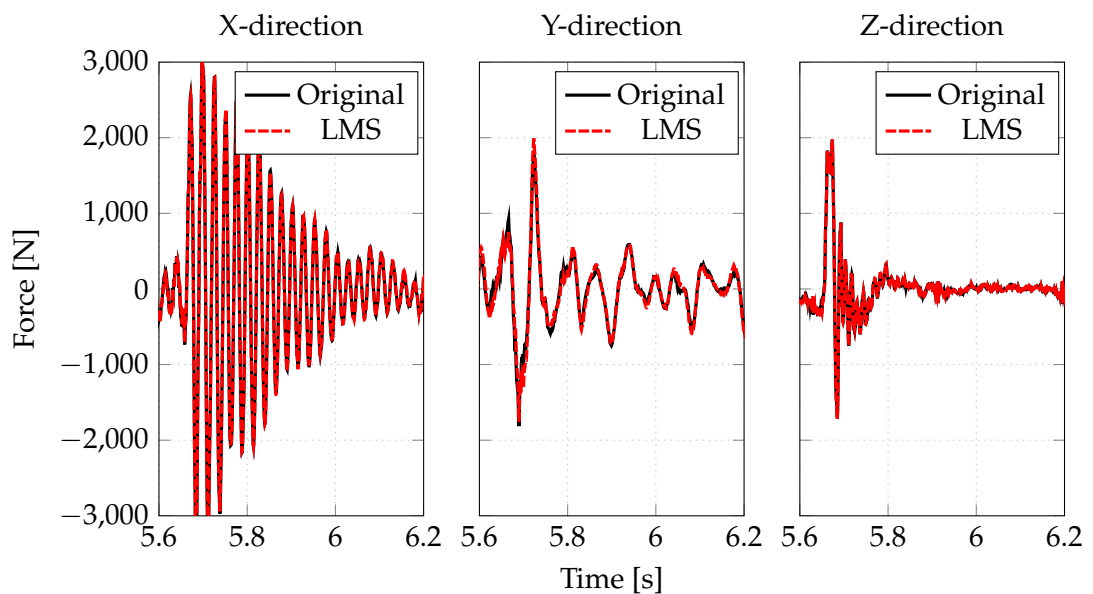


FIGURE 4.2. Comparing estimated forces, using LMS, with input signal in time domain.

It is a different situation when applying noise, especially at higher frequencies shown in figures 4.10 - 4.15. However, it is clear that the peaks are identified by the method, and that the overall trend is clearly visible. It is clear studying the results that it is in fact the regions that have the highest power spectral density that are accurately found. This is understandable studying the frequency spectra of the noise applied, as the levels at

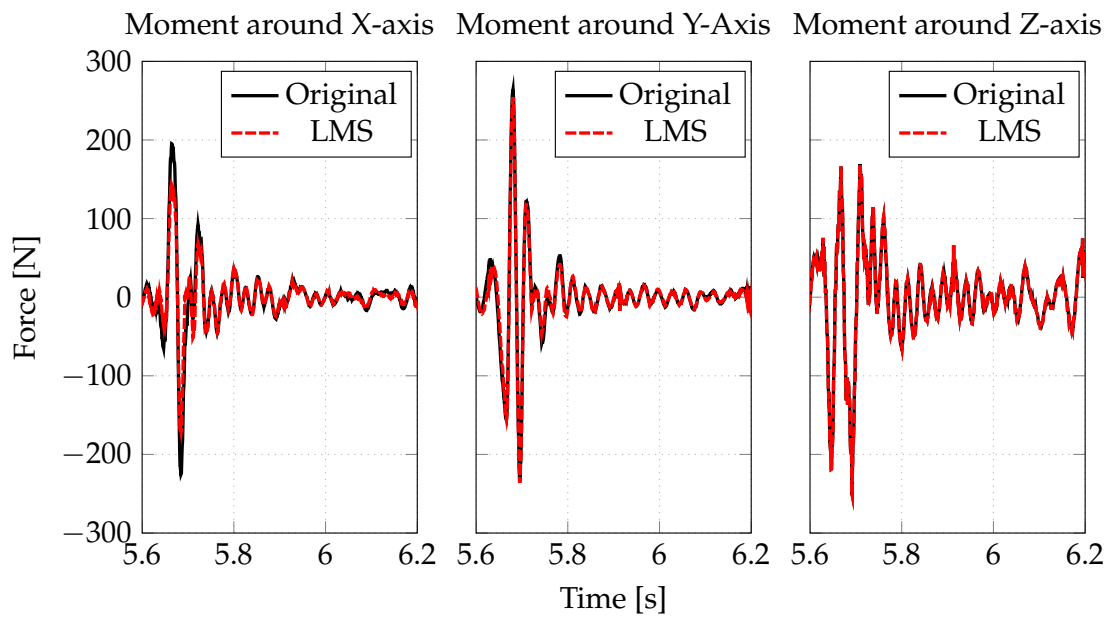


FIGURE 4.3. Comparing estimated moments, using LMS, with input signal in time domain.

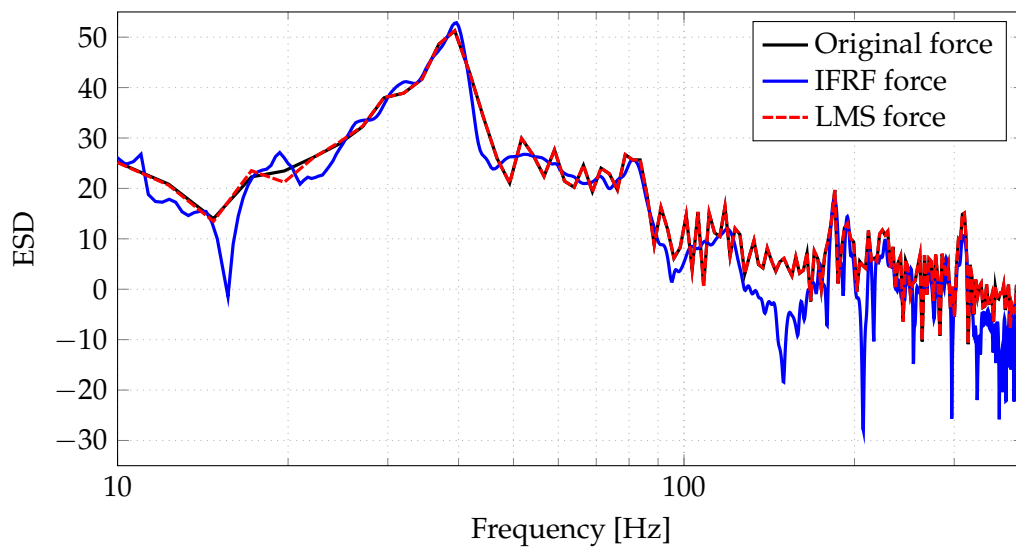


FIGURE 4.4. Comparing the spectra of the two methods with the original spectra for X-direction.

higher frequencies are of the same magnitude, see figure 4.16.

In theory however, as the noise should be uncorrelated. And indeed, checking the

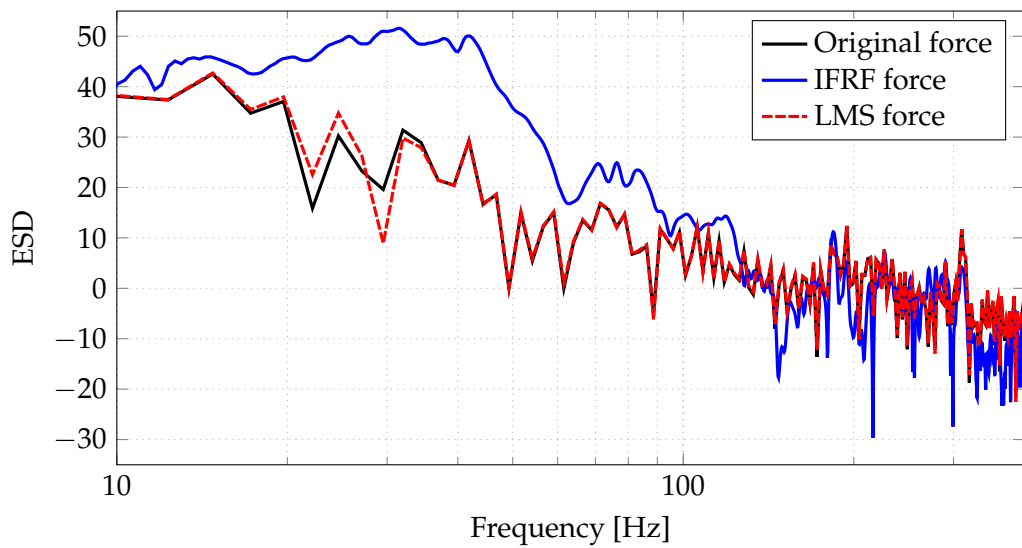


FIGURE 4.5. Comparing the spectra of the two methods with the original spectra for Y-direction.

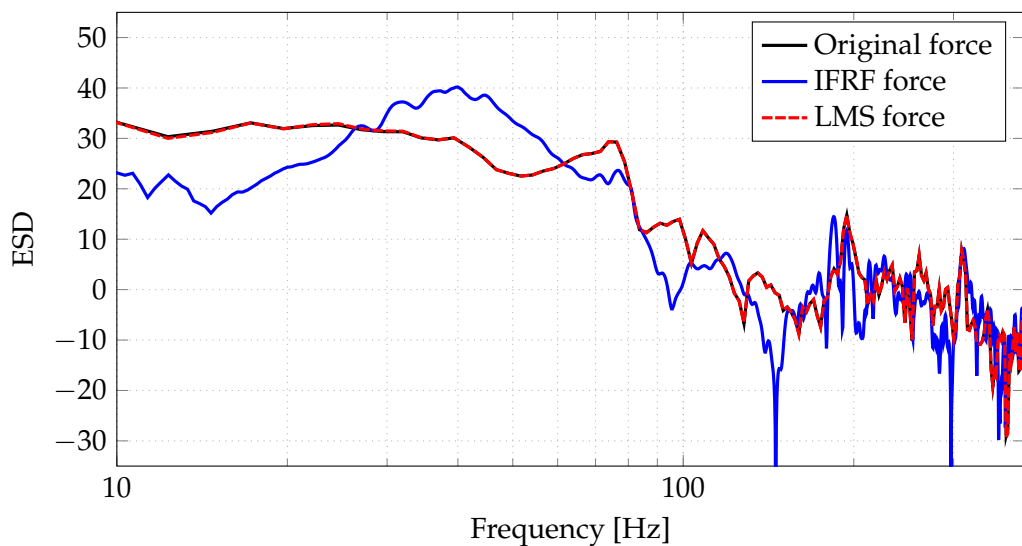


FIGURE 4.6. Comparing the spectra of the two methods with the original spectra for Z-direction.

cross-correlation of the noise proves it has very little, close to no correlation. As a result it should be averaged out. Let us therefore see how the result compares to the IFRF method.

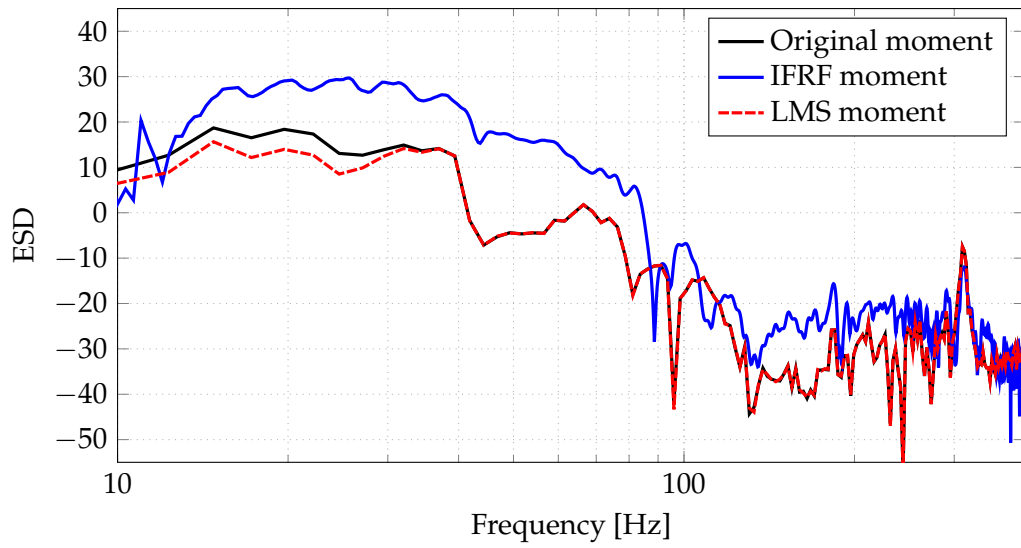


FIGURE 4.7. Comparing the spectra of the two methods with the original spectra for moment around X-axis.

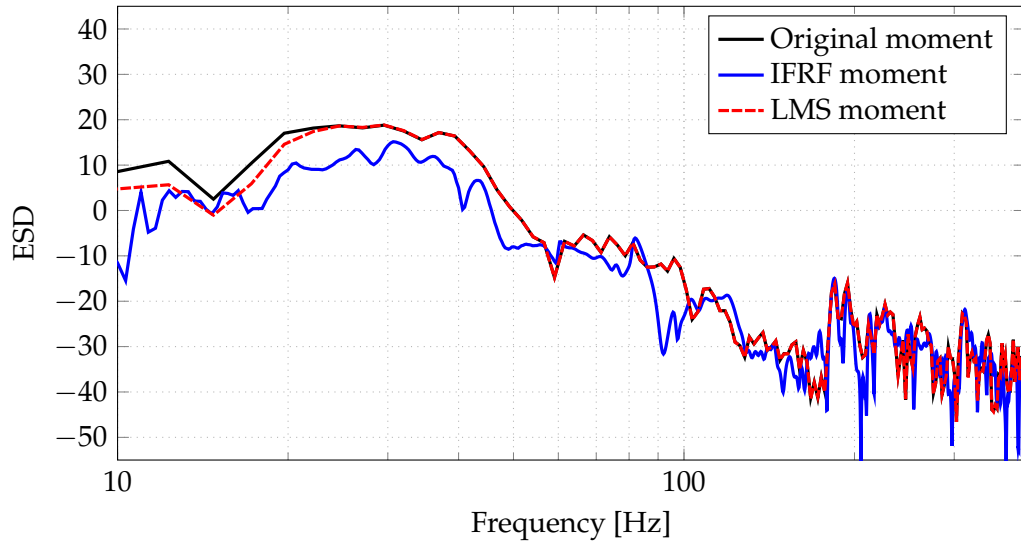


FIGURE 4.8. Comparing the spectra of the two methods with the original spectra for moment around Y-axis.

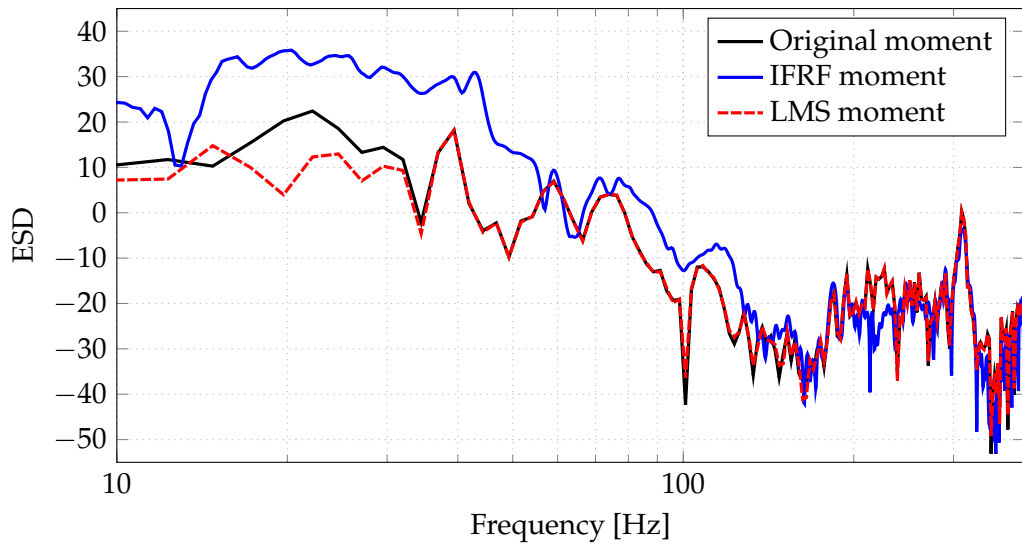


FIGURE 4.9. Comparing the spectra of the two methods with the original spectra for moment around Z-axis.

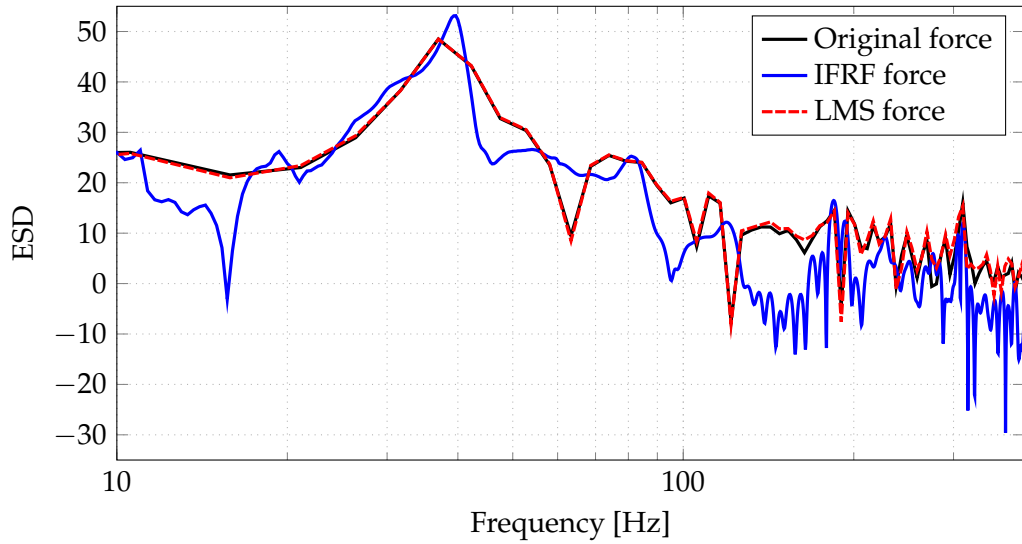


FIGURE 4.10. Comparing the spectra of the two methods with the original spectra for X-direction when noise is added.

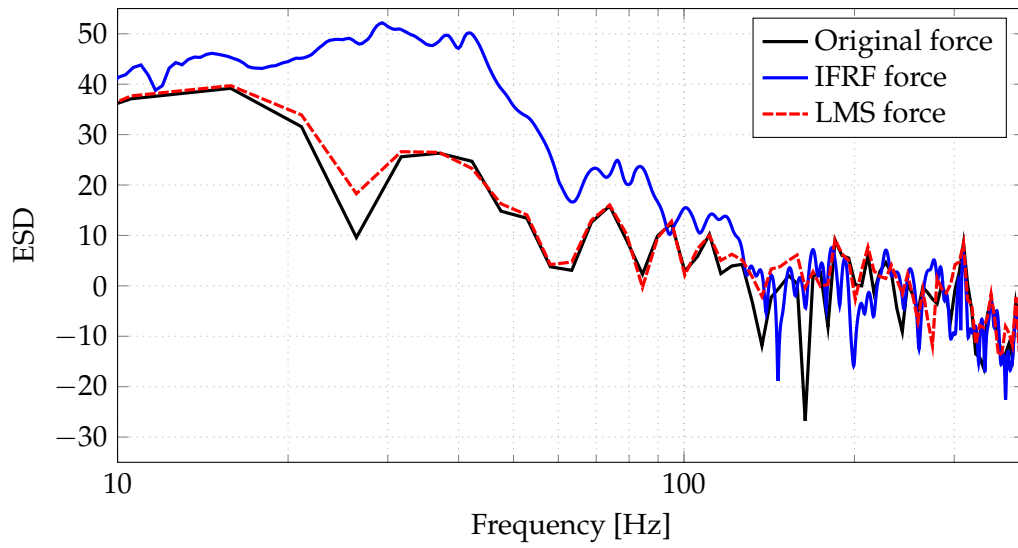


FIGURE 4.11. Comparing the spectra of the two methods with the original spectra for Y-direction when noise is added.

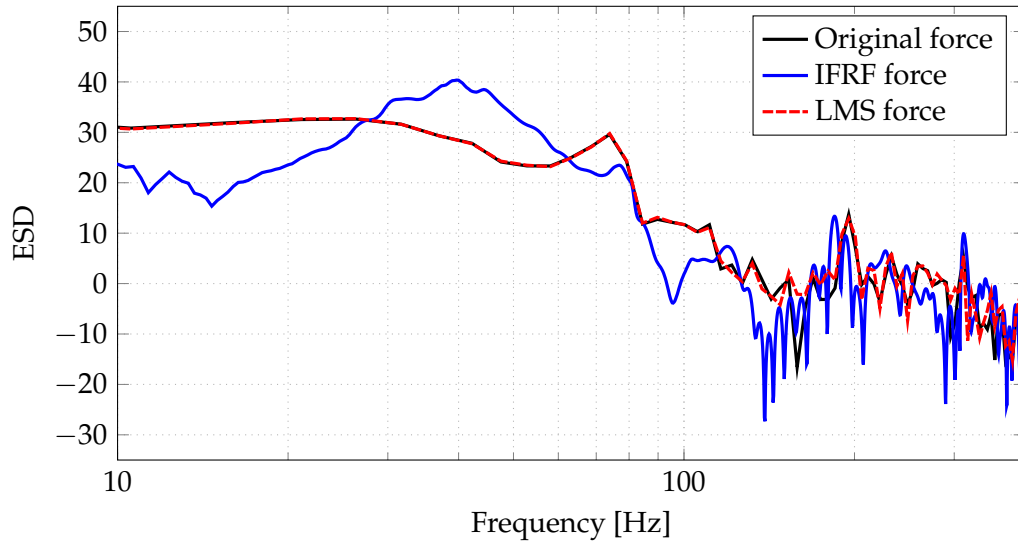


FIGURE 4.12. Comparing the spectra of the two methods with the original spectra for Z-direction when noise is added.

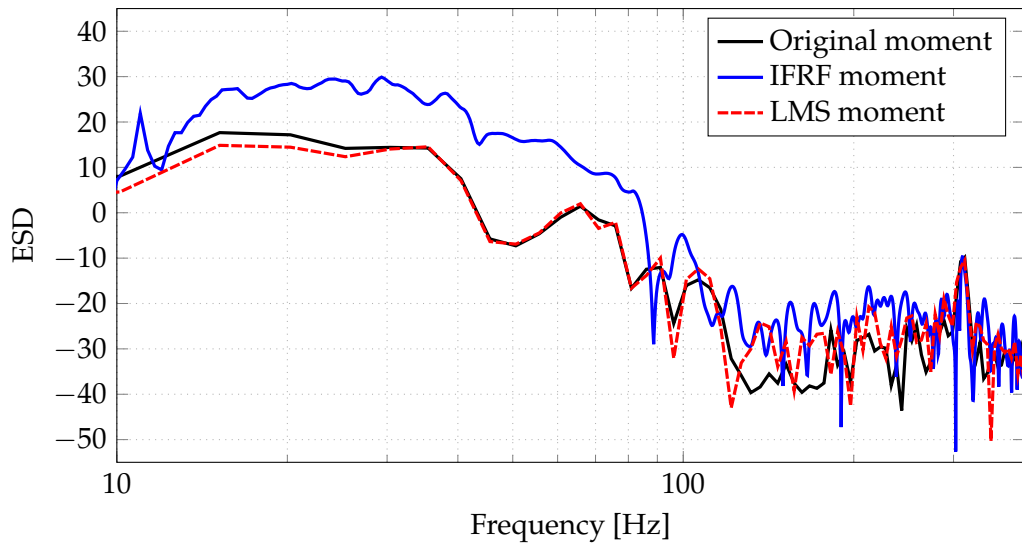


FIGURE 4.13. Comparing the spectra of the two methods with the original spectra for moment around X-axis when noise is added.

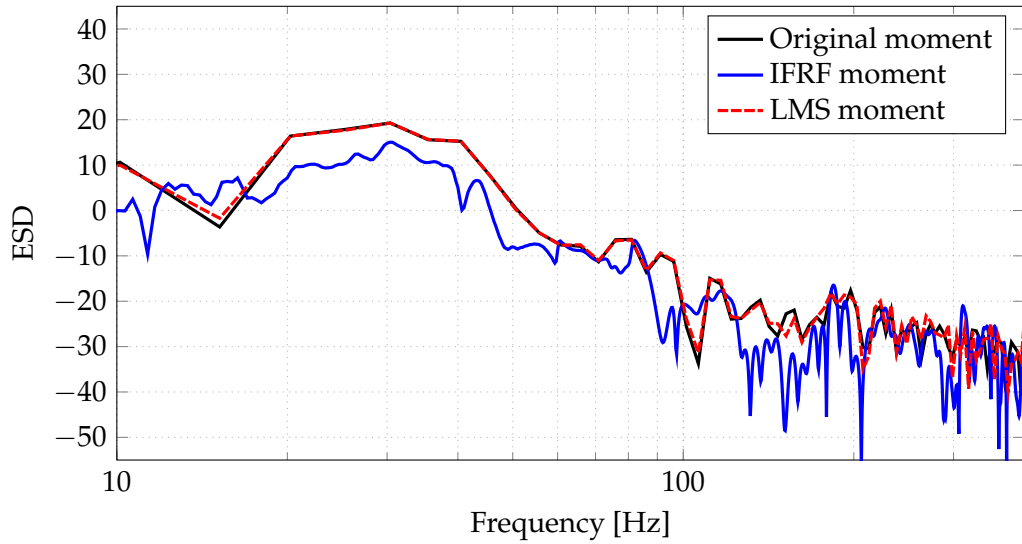


FIGURE 4.14. Comparing the spectra of the two methods with the original spectra for moment around Y-axis when noise is added.

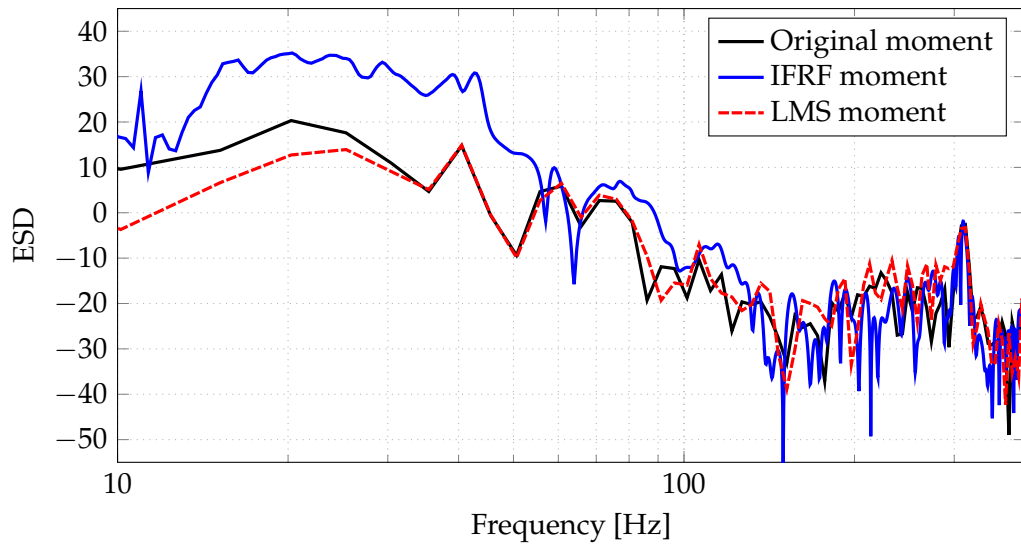


FIGURE 4.15. Comparing the spectra of the two methods with the original spectra for moment around Z-axis when noise is added.

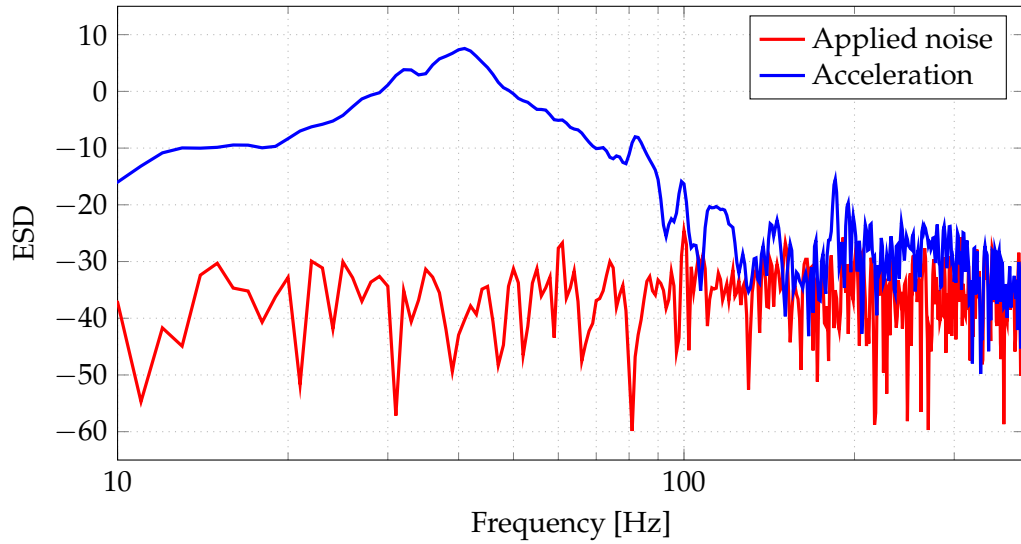


FIGURE 4.16. Comparing acceleration spectra plus added noise at one acceleration at X-direction.

4.1.2. Comparison with IFRF

In figures 4.2 - 4.3 the results from the different methods are compared, while the results for the force in X-direction look good for both methods, the results for the IFRF method is not as accurate when comparing the other directions. The reasons as to why this is could be manifold. But surely there are several reasons as to why the difference exists.

Further the IFRF method requires the force spectra to consist of an equal amount of frequency components. This will require zero padding or reducing the spectral components in the transfer function. In this calculation zero padding was applied, something that is not necessary for the LMS. Seeing as how the transients have a short duration, the frequency resolution will suffer, and in order to compare the methods, a 6th octave band calculation may yield something that is more easily compared.

The figures 4.17 to 4.22 show the 6th octave band levels for the calculated forces. Something that is easily seen in the 6th octave band levels is that the estimation by the LMS algorithm accurately finds the peaks, and that the largest deviations are found in the areas with low ESD in the weaker forces and moments.

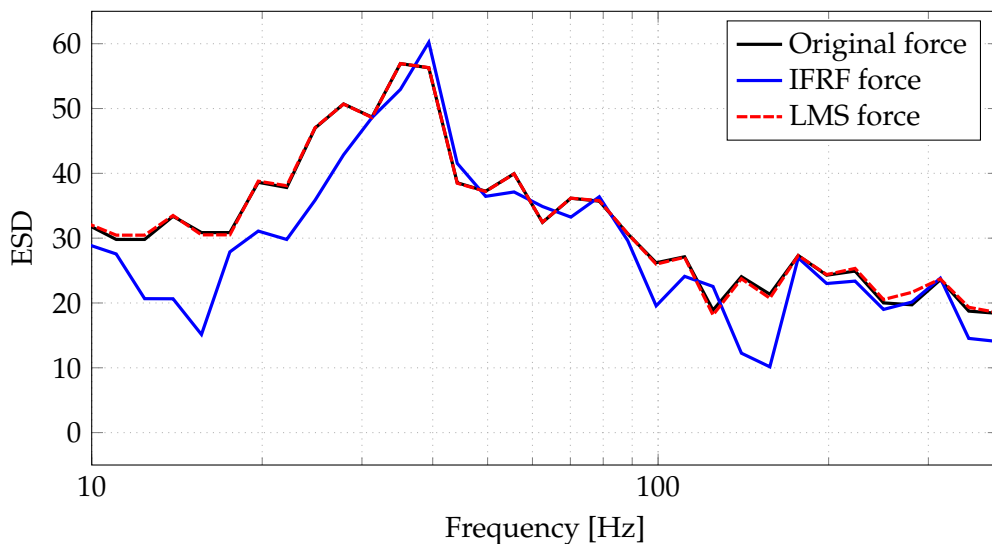


FIGURE 4.17. Comparing the spectra of the two methods with the original spectra for X-direction when noise is added.

Adding noise does lower the accuracy of the LMS algorithm, especially at the higher frequencies for the moments and forces that are of the lowest magnitude, but the stronger forces and moments still are quite accurately found. This appears to be less true for the IFRF method, where one can see a degradation of the results even for these forces and moments. These results seem to show that if uncorrelated noise is introduced, the

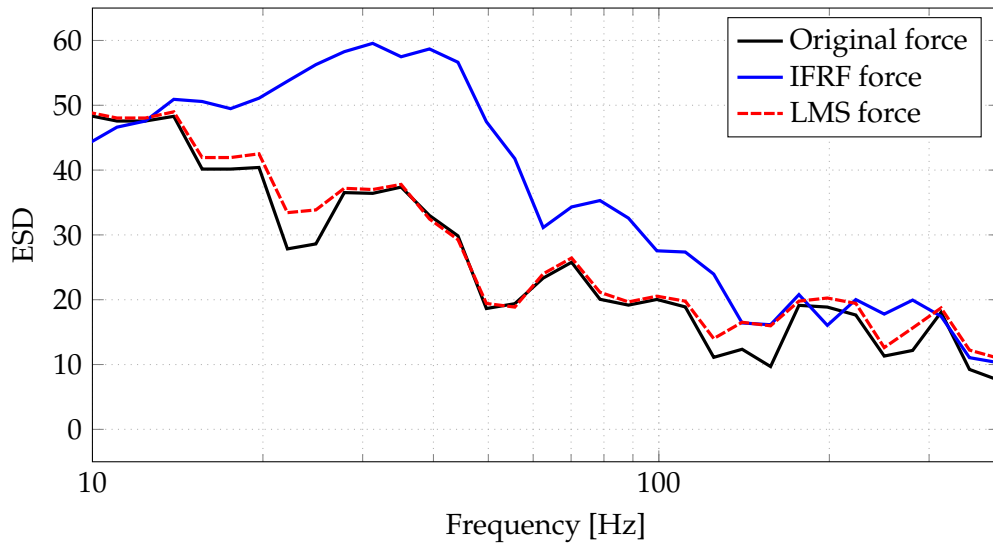


FIGURE 4.18. Comparing the spectra of the two methods with the original spectra for Y-direction when noise is added.

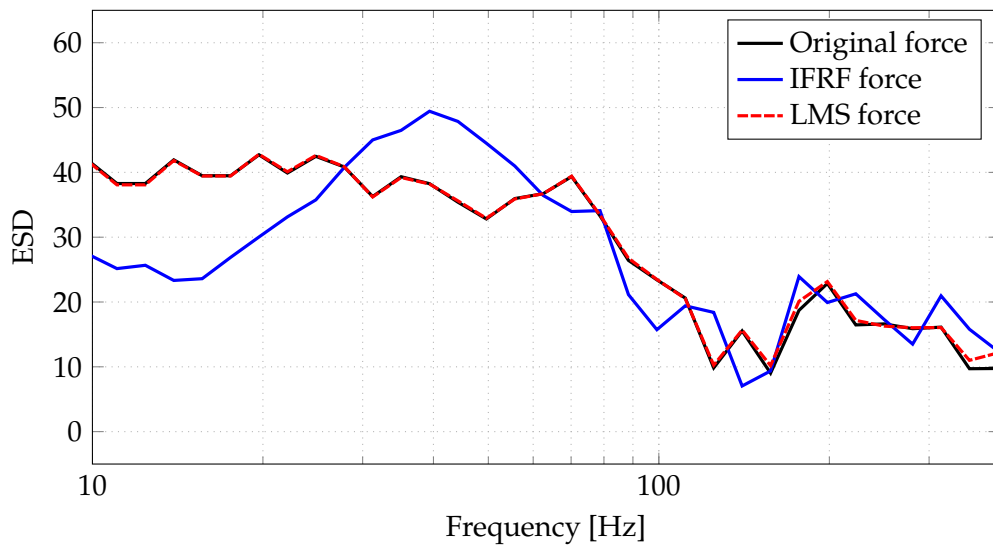


FIGURE 4.19. Comparing the spectra of the two methods with the original spectra for Z-direction when noise is added.

method handles this rather well.

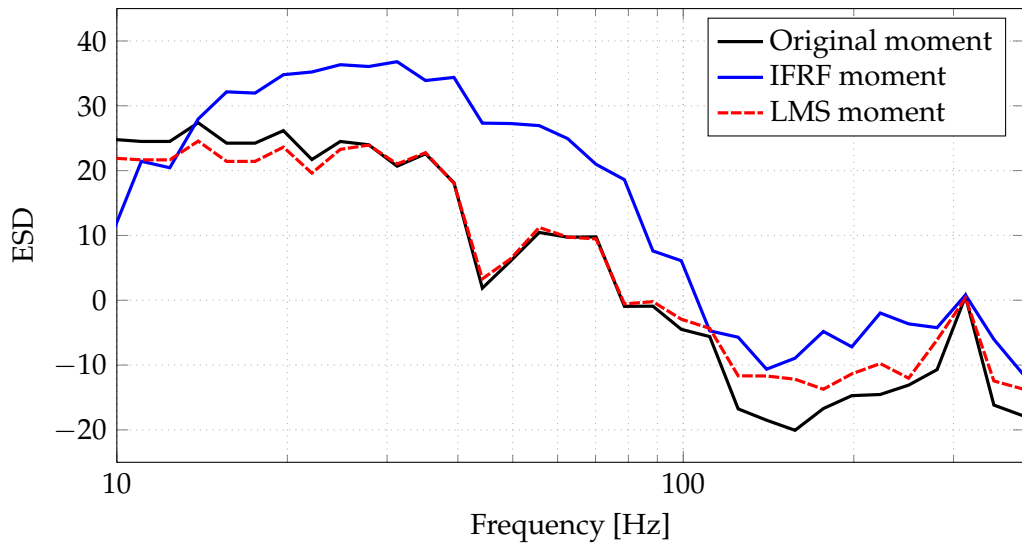


FIGURE 4.20. Comparing the spectra of the two methods with the original spectra for moment around X-axis when noise is added.

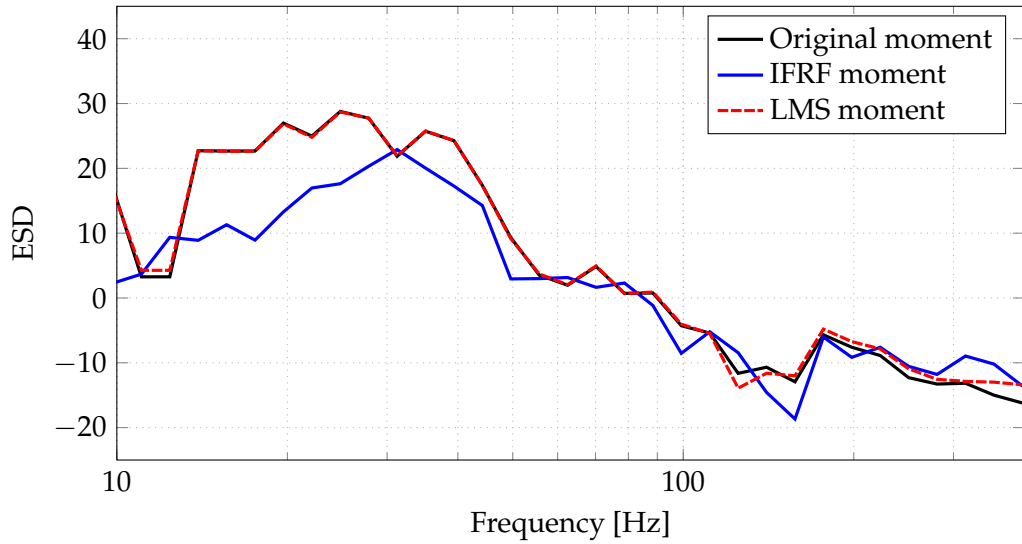


FIGURE 4.21. Comparing the spectra of the two methods with the original spectra for moment around Y-axis when noise is added.

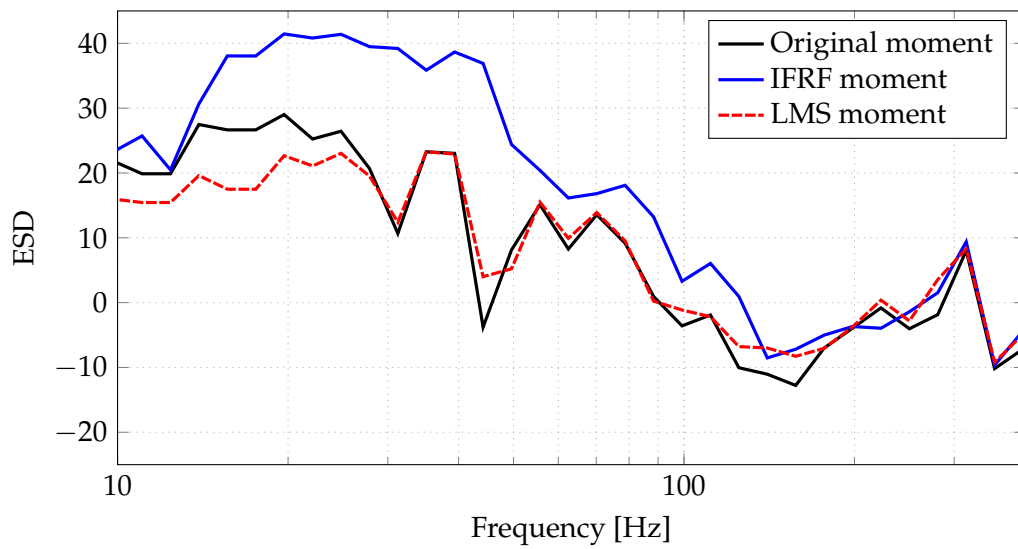


FIGURE 4.22. Comparing the spectra of the two methods with the original spectra for moment around Z-axis when noise is added.

4.2. Impact Hammer Simulations

Using the results from the measurements conducted with the impact hammer, results have been procured using both IFRF and the LMS algorithm. The results will be displayed for each of the measurement cases that was described in section 3.

4.2.1. SIMO Simulation

The first results come from a simple excitation in Y-direction, assuming that there is just one force acting upon the structure. As can be seen from studying the pressure in figure 4.23 there is an underestimation in comparison to the measured pressure. This can be seen in the frequency domain as well. The difference between the measured and calculated spectral density are shown in figure 4.24.

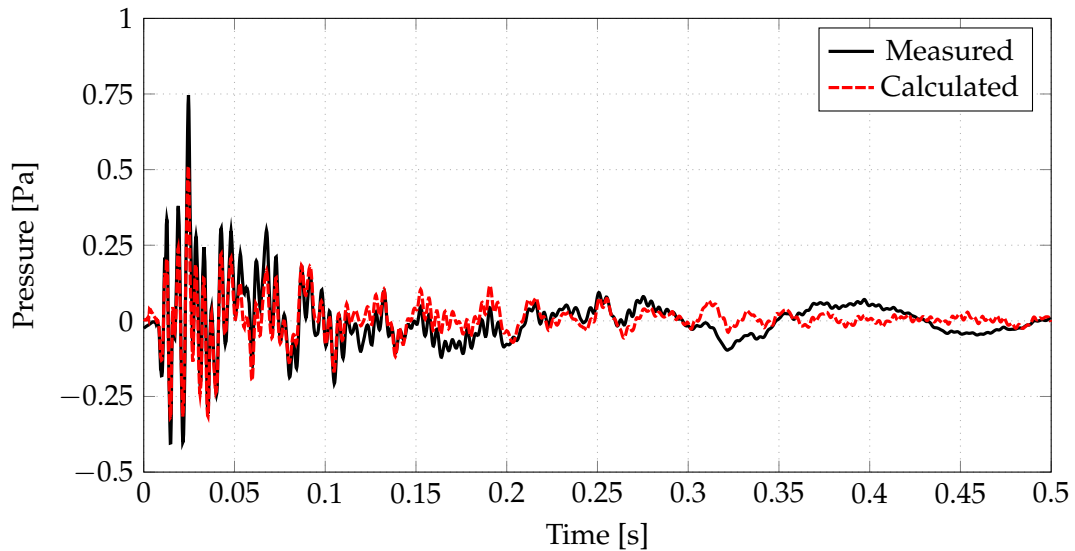


FIGURE 4.23. The measured and calculated pressure in time domain when exciting in Y-direction.

One important aspect is that the measured force is in fact measured, and a lack of time resolution and sensitivity may influence the measurement. This can be seen if one uses the measured force to calculate the sound pressure at the microphone, seen in figure 4.25. While some of it may be due to background noise, after all the levels in the mic are low. Even if adding the spectra of the background noise, the levels are lower.

But one can use the measured force and compare the pressure it creates, to the pressure gained from the estimated force, the results are indeed very similar, though the under

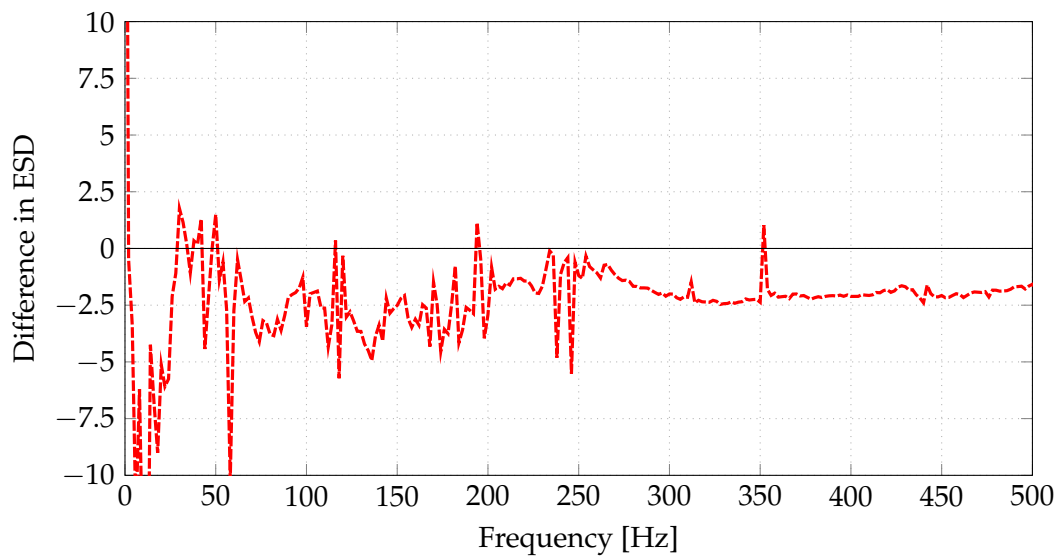


FIGURE 4.24. The difference between the measured and calculated spectral density when exciting in Y-direction.

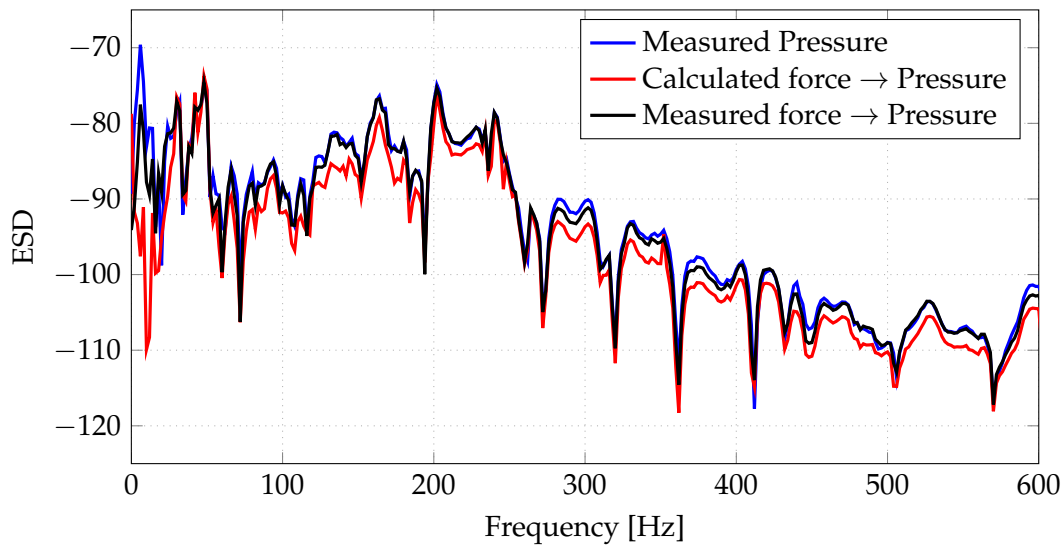


FIGURE 4.25. Showing measured pressure and comparing it to spectra calculated from measured and calculated force. Excitation is in the centre of the wheel in Y-direction.

estimation is still visible.

4.2.2. MIMO Simulation

When the exciting force is at an angle to the rim, the excitation can be split into two forces, one in Z-direction and one in Y-direction. Using the impulse responses for these two directions, at positions close to the excitation, the force can be estimated. This will of course not be entirely accurate, as the transfer functions will be somewhat different from the ones at the excitation position, but it should be sufficiently similar. Something that the results that will follow seems to suggest.

4.2.2.1. Results From Two Impact Forces

When exciting the structure in one direction, this time in Z direction, the results are obtained shown in figure 4.26. The force is accurately estimated, and what's more, the algorithm identifies the Z direction as the point of excitation. Looking at the frequency spectra of the impact, figure 4.27 the results are very good indeed. With levels within 1 dB for large parts of the spectra.

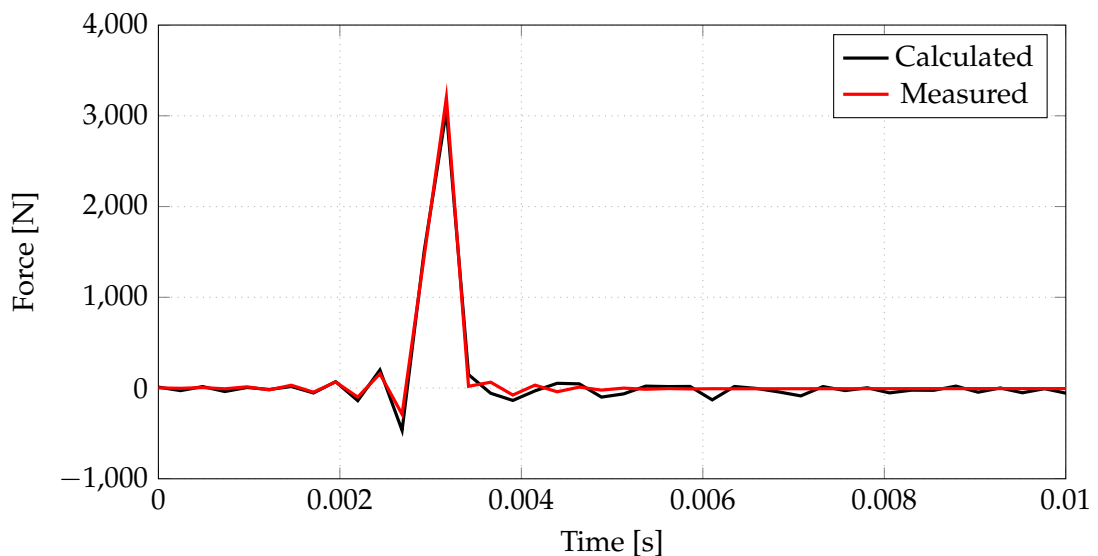


FIGURE 4.26. Showing the measured force and the calculated force in time domain when using an excitation mainly in Z-direction..

But as previously mentioned, the measured force is not necessarily completely accurate, and therefore the measured pressure is important to compare. Shown in figure 4.28 the calculated spectra very closely resembles the measured, at many of the frequencies within 0.5 dB of the measured spectra. Using the IFRF to do the same estimation yields

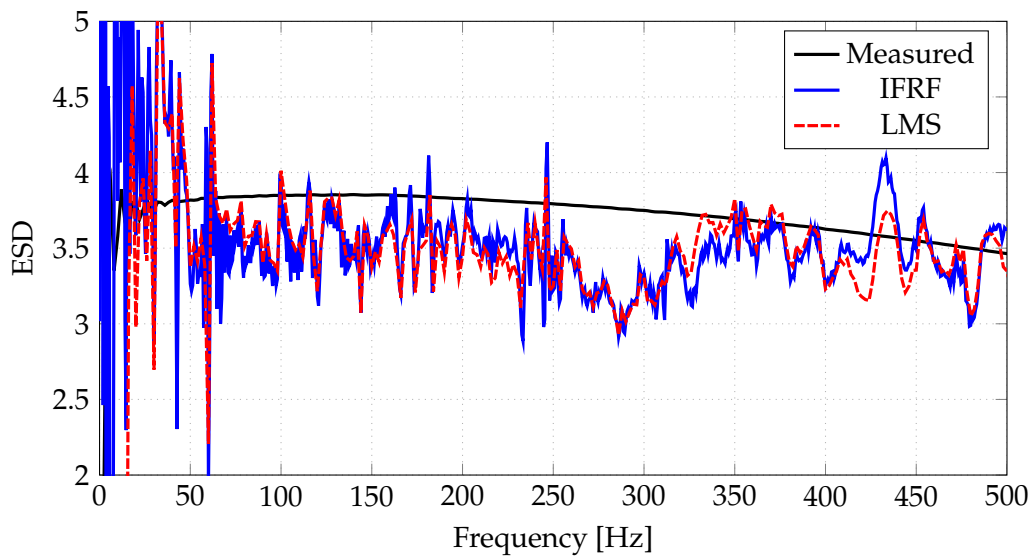


FIGURE 4.27. Showing the ESD of the calculated Force, IFRF and LMS, and the measured force when using an excitation mainly in Z-direction.

similar results, and in order to really study the differences the dB difference is shown in figure 4.29.

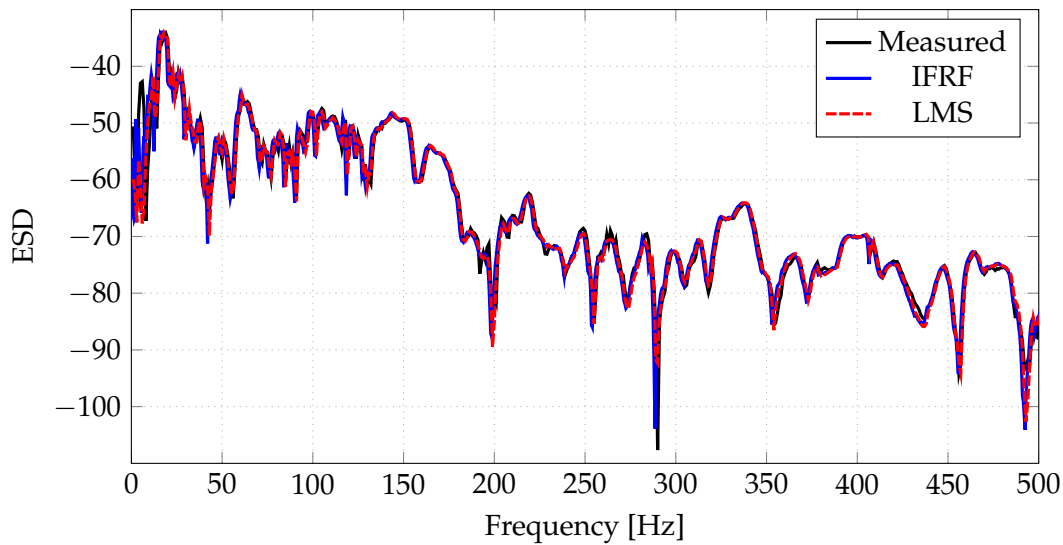


FIGURE 4.28. Showing the measured pressure spectra and comparing it to the spectra calculated from IFRF and LMS. The force was applied in the Z-direction..

Interestingly, the results does not differ much from the IFRF and the LMS, though there

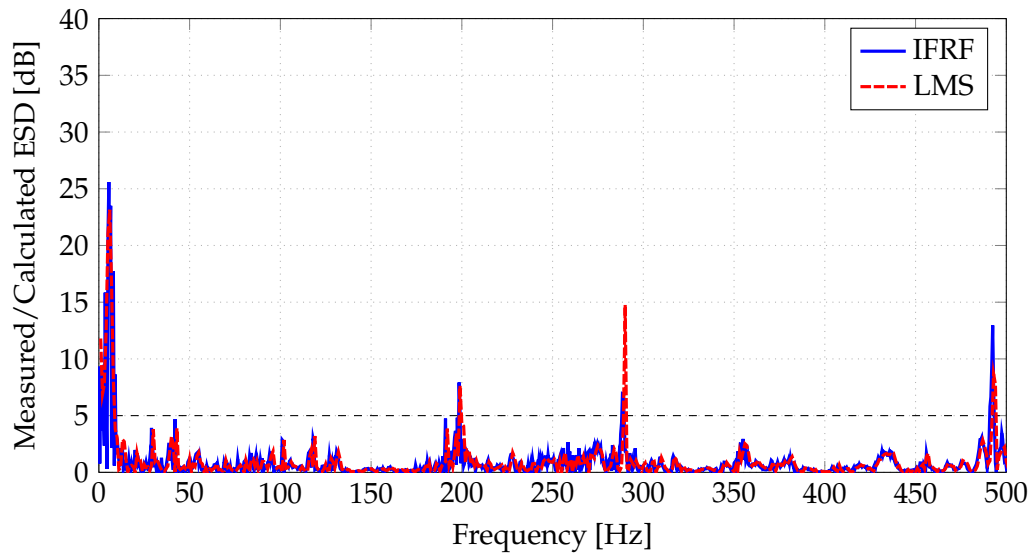


FIGURE 4.29. Showing the dB difference between the calculated pressure for LMS and IFRF when force was applied in Z-direction.

are some frequencies where both the IFRF and LMS loses accuracy. Though the LMS only really loses accuracy at the larger dips, whereas the IFRF seem to lose accuracy at frequencies of higher magnitudes. But overall, both methods produce good results.

If the excitation is instead at the rim, at an angle, the forces are of a more equal magnitude, figure 4.30. Assuming that the measured force could be flawed, the best way of measuring the results is comparing with the microphone pressure.

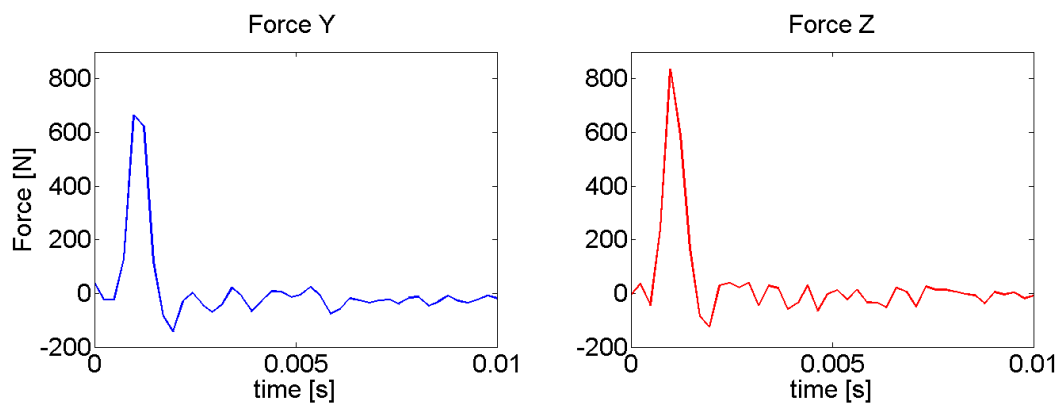


FIGURE 4.30. Showing the two time domain signals for forces in Y and Z direction.

In figure 4.31 the ESD for the microphone pressure is compared. Both methods produce good results, however as shown in figure 4.32, the LMS have frequency ranges where

the estimation is better.

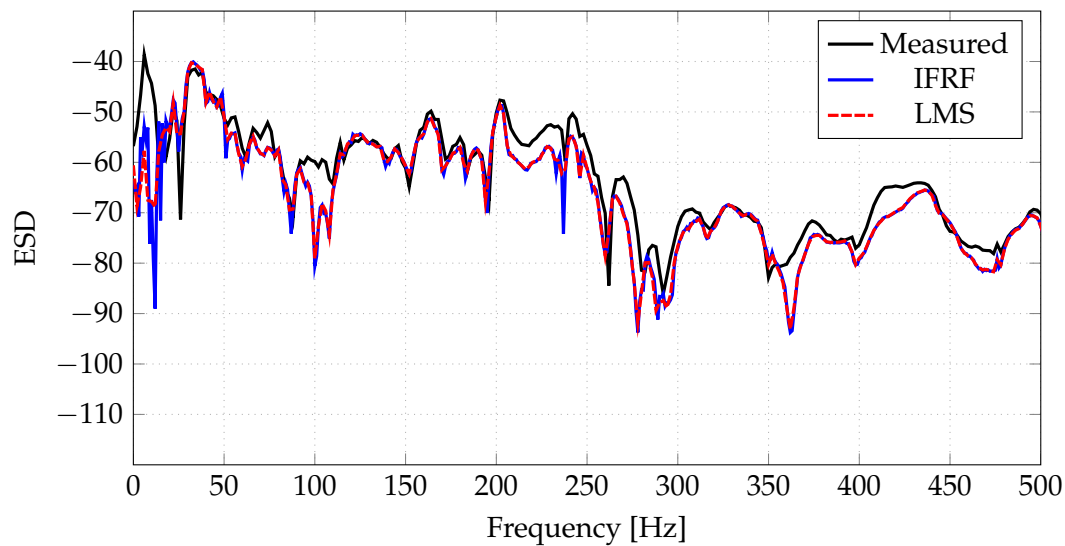


FIGURE 4.31. Showing the spectra of the measured pressure and comparing it to the spectra calculated from IFRF and LMS. The force was applied in an angle at the top corner, with mainly components in Z and Y direction

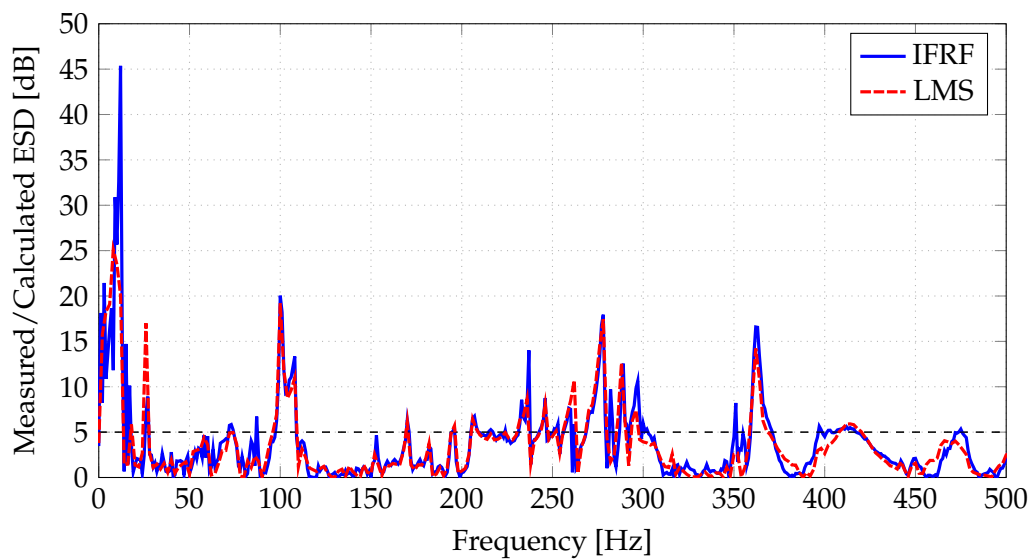


FIGURE 4.32. Showing the magnitude of the dB difference between the calculated pressure for LMS and IFRF when using an excitation at the top rim, with components mainly in Z and Y..

4.2.2.2. Results From Three Impact Forces

The next application of the algorithm is applying it to the case when an aluminum cube is placed at the wheel hub. Like previously the simulation can be conducted for an excitation mainly in one direction, and the results are shown in figures 4.33 - 4.34. Like before the algorithms identifies mainly a force in the excitation direction.

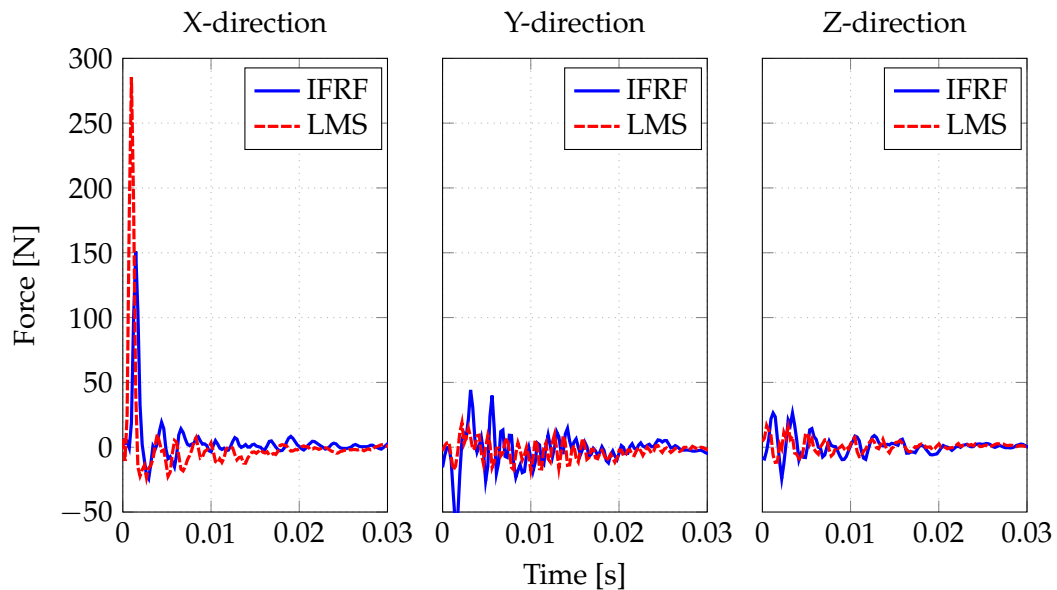


FIGURE 4.33. Calculated time signals for forces in the X,Y and Z directions when applying a force mainly in X-direction.

Studying the spectra of the estimated pressure one clearly note one thing, figures 4.35-4.36, the worst estimation is at frequencies where there is little power. This is not surprising, considering that this was the case found in the virtual study as well. But like before, if using the measured force to estimate the pressure, there is similar accuracy. This could suggest that the problem is with the measured transfer functions more than anything.

What is more, the IFRF is showing larger differences at frequencies compared to the LMS. If comparing to previous results, they no longer follow the same trends.

Studying the coherence, this does not seem unlikely, it is low over large portions of the frequency range, see figure 4.37. And this is only for the pressure, the situation is similar for the transfer functions measured to the accelerometers.

Using an excitation at one corner yield three forces in the same order of magnitude, see figure 4.38. From these forces the pressure at the mic is as before close to the measured,

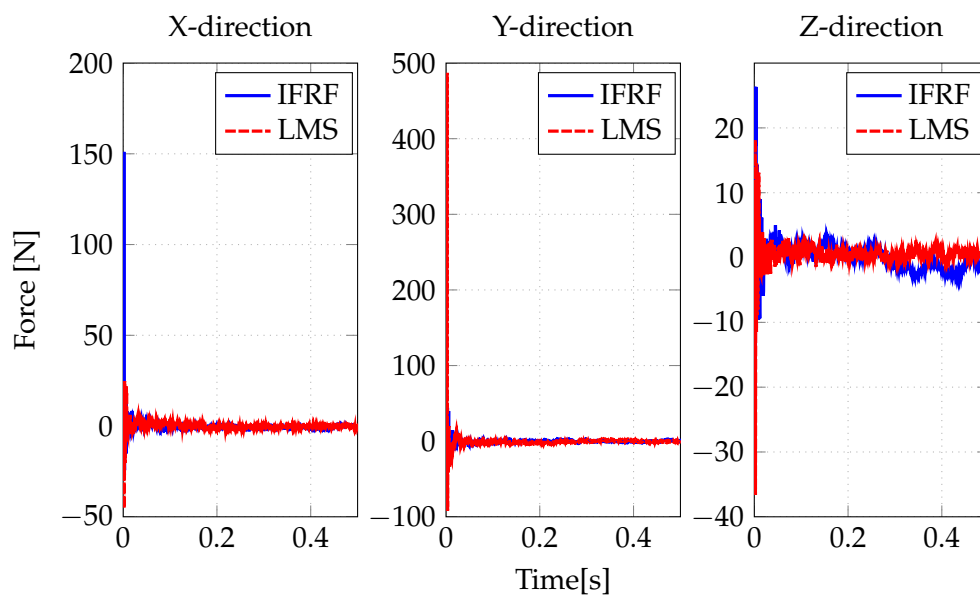


FIGURE 4.34. Calculated time signals for forces in the X,Y and Z directions when applying a force mainly in Y-direction.

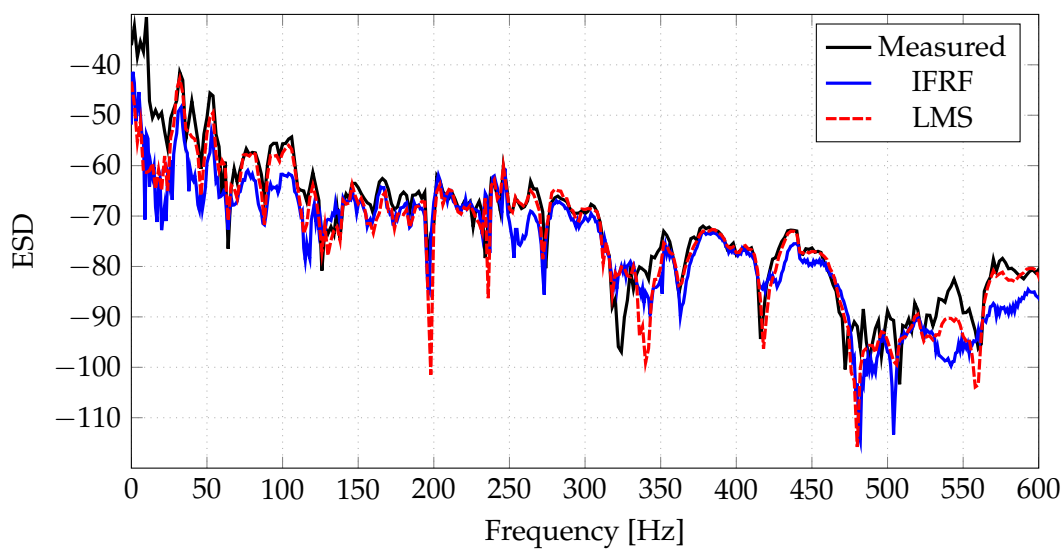


FIGURE 4.35. Showing the spectra of the measured pressure and comparing it to spectra calculated from IFRF and LMS when excited applying a force mainly in X-direction..

figure 4.39 and 4.40.

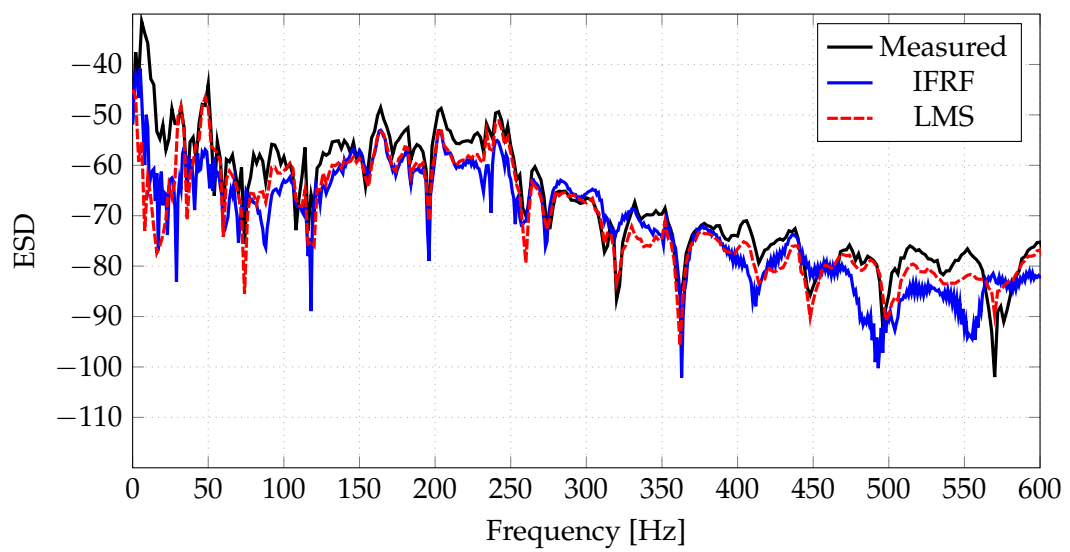


FIGURE 4.36. Showing the spectra of the measured pressure and comparing it to spectra calculated from IFRF and LMS when excited applying a force mainly in Y-direction.

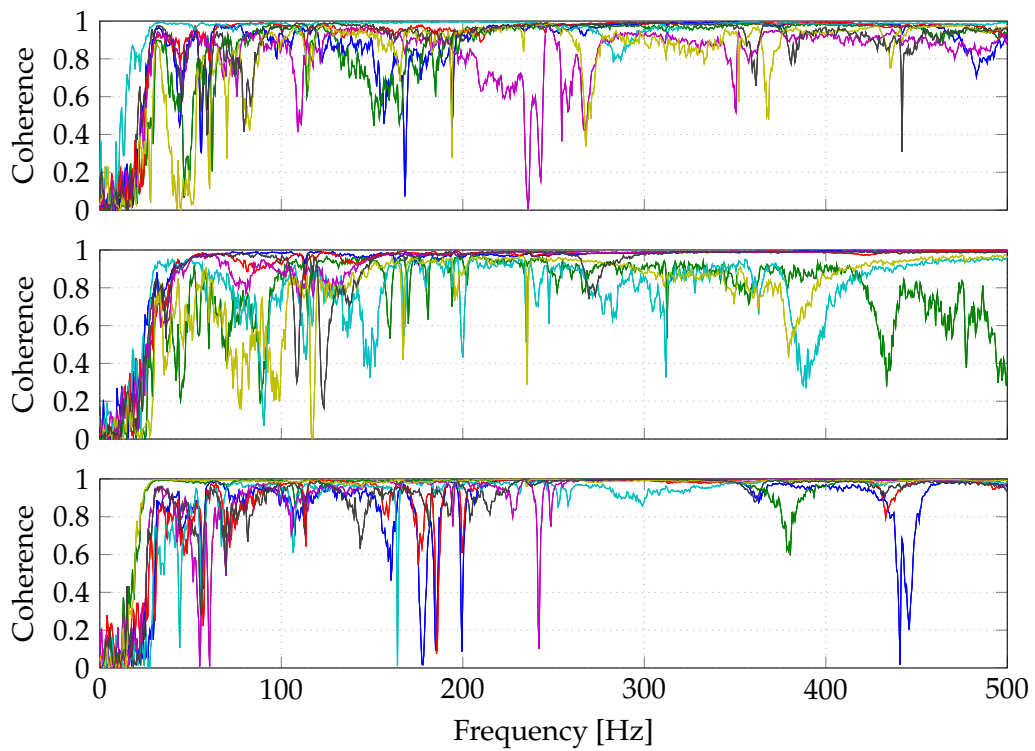


FIGURE 4.37. Showing the coherence for the different channels and directions used. Top is X-direction, followed by Y and lastly Z.

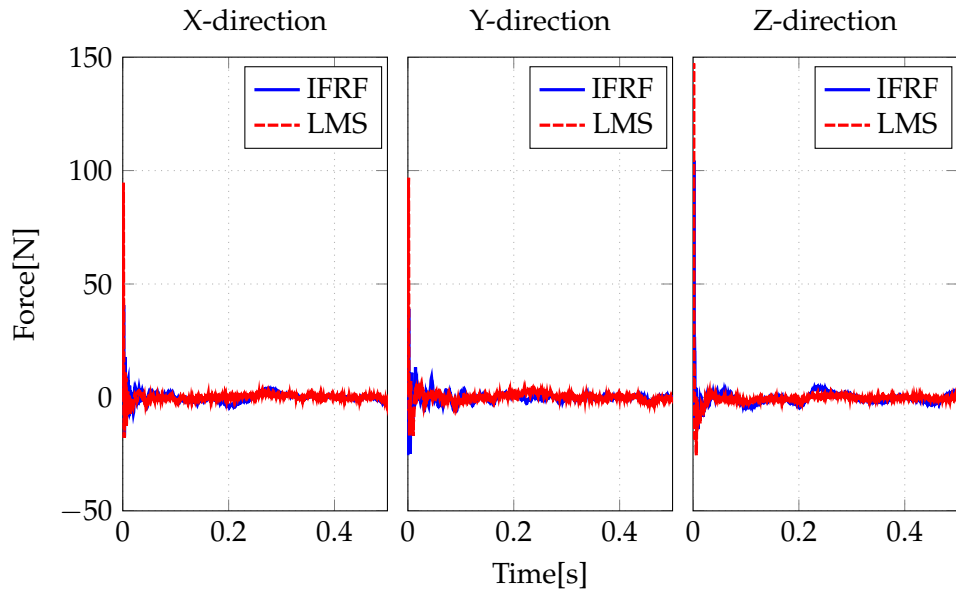


FIGURE 4.38. Calculated time signals when using an excitation divided between the three directions X,Y and Z.

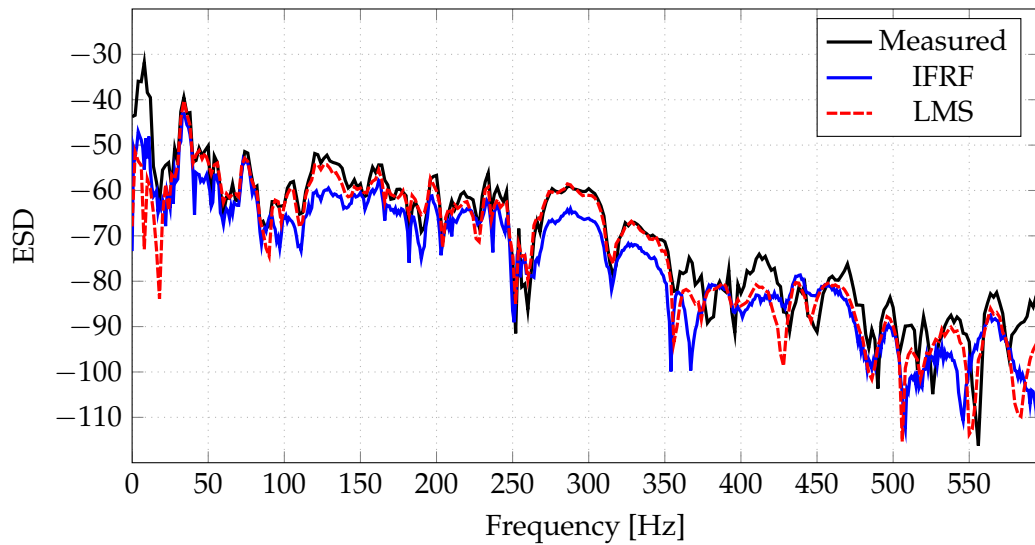


FIGURE 4.39. Comparing calculated spectra for LMS and IFRF with the spectra measured when exciting the structure using a force evenly distributed over X,Y and Z direction.

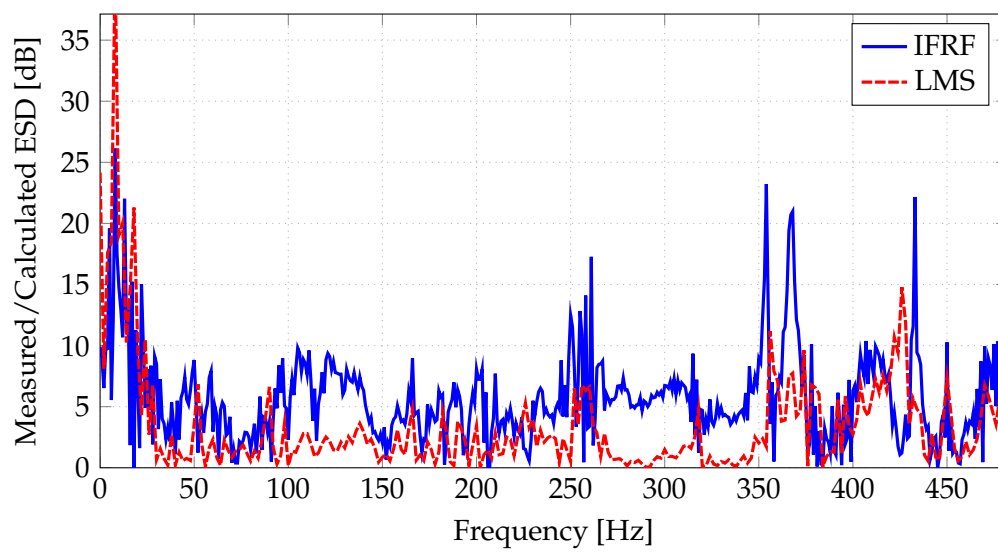


FIGURE 4.40. Showing the magnitude of the dB difference between the calculated pressure for LMS and IFRF when using an excitation at an angle distributed over X, Y and Z directions.

4.3. MIMO Equivalent Forces

The idea in this section is that if the transfer functions from a position, different to the excitation position, to all the measurement positions is known, one can calculate the forces at this position which will yield the same excitation. Taking this one step further, one can calculate the response at other positions using these calculated forces as long as the transfer function is known.

More interesting results come from using the transfer functions measured using the cube to create forces yielding equivalent accelerations at the measurement positions. The first case studied is using the excitation in Z-direction at the top of the wheel. Then using the measured accelerations to calculate excitation forces at the hub, one gets the results shown in figure 4.41. Interestingly, if comparing to some of the previous results, there is a difference between the two methods, while the LMS is at large better at estimation, see figure 4.42.

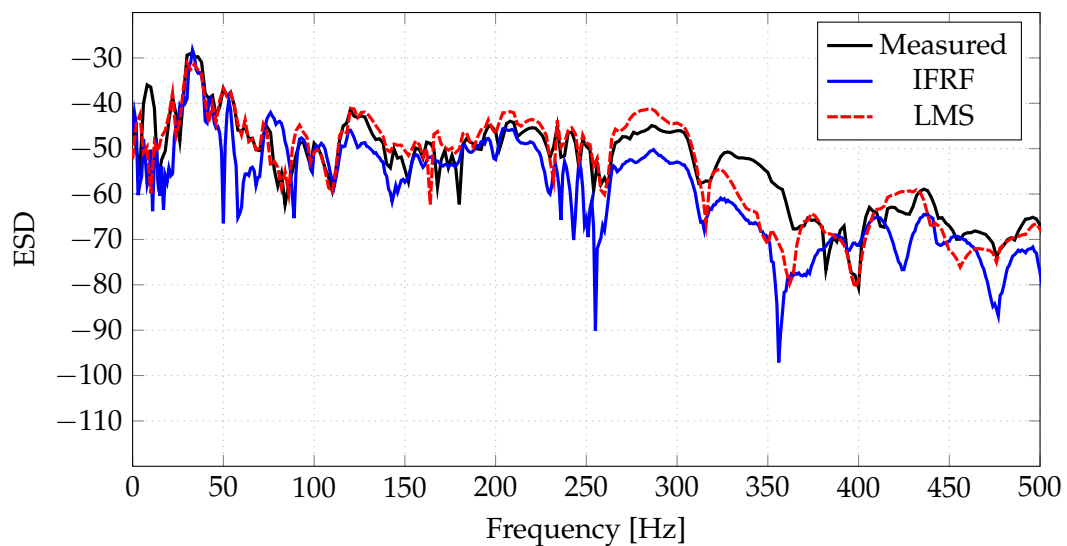


FIGURE 4.41. Comparing the calculated spectra from IFRF and LMS to the measured spectra. Calculation was carried out using three equivalent forces placed at the cube in the centre of the wheel.

The results differ some when using excitation in either ZY or Y direction at the top of the wheel. There are different frequency regions that are better estimated by different methods. Something that is easily seen in figures 4.43 and 4.44.

This is interesting and also studying the spectra shows some interesting details, figures 4.45 and 4.46. The spectra no longer only differ in mostly magnitude, but in some

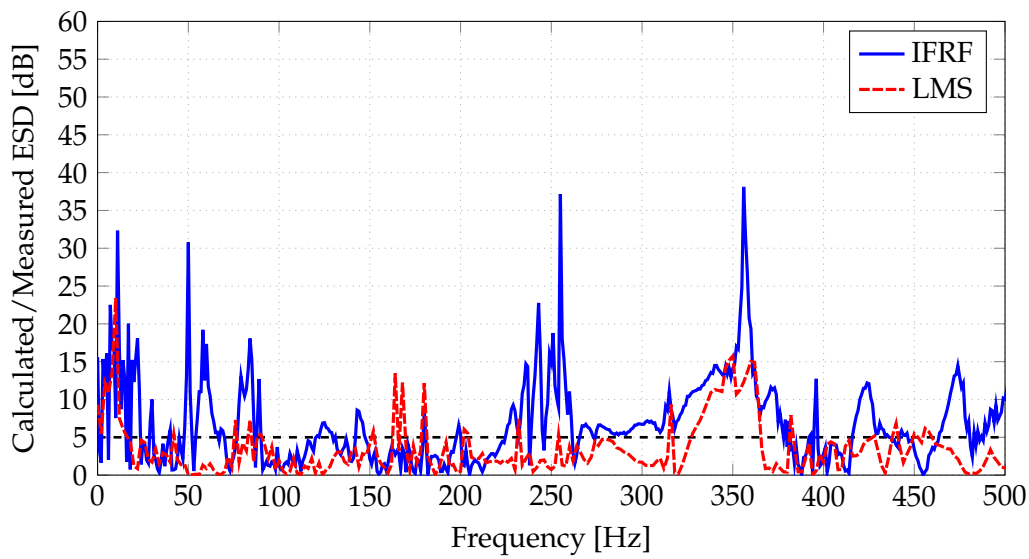


FIGURE 4.42. Showing the magnitude of the dB difference between the calculated pressure for LMS and IFRF using estimated equivalent forces. Structure was excited in Z-direction.

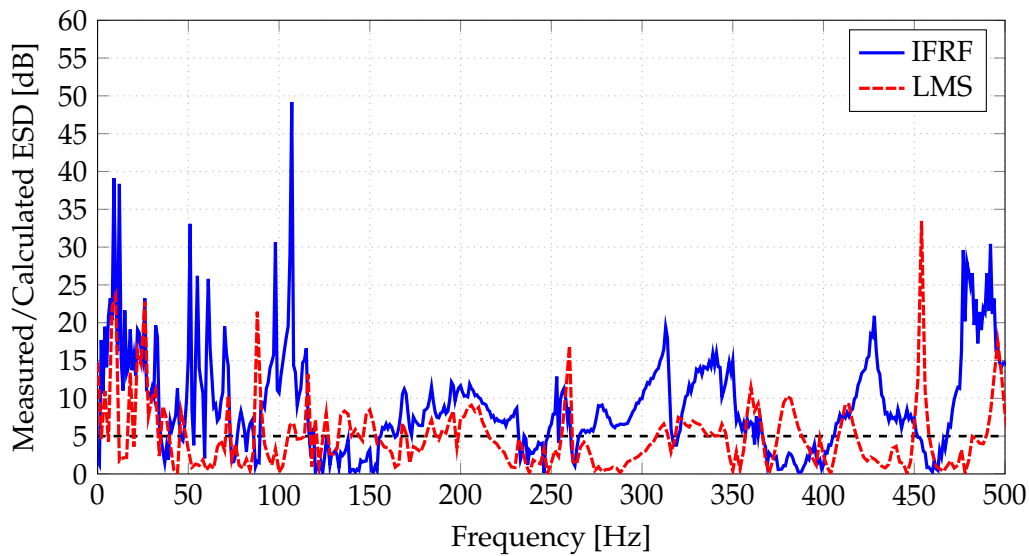


FIGURE 4.43. Showing the magnitude of the dB difference between the calculated pressure for LMS and IFRF using estimated equivalent forces. Structure was excited in Y-direction.

frequency regions the overall shape of the spectra is different. Which gives some clues

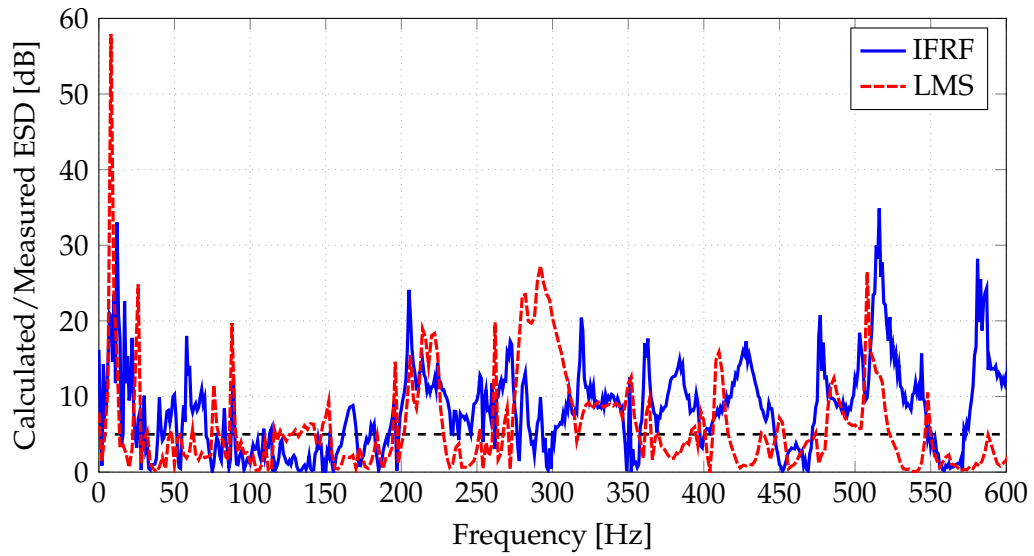


FIGURE 4.44. Showing the magnitude of the dB difference between the calculated pressure for LMS and IFRF estimated equivalent forces. excitation in mainly Z and Y-direction.

as to what is in fact happening. But before speculating let us also study the excitation at the centre of the wheel using equivalent forces.

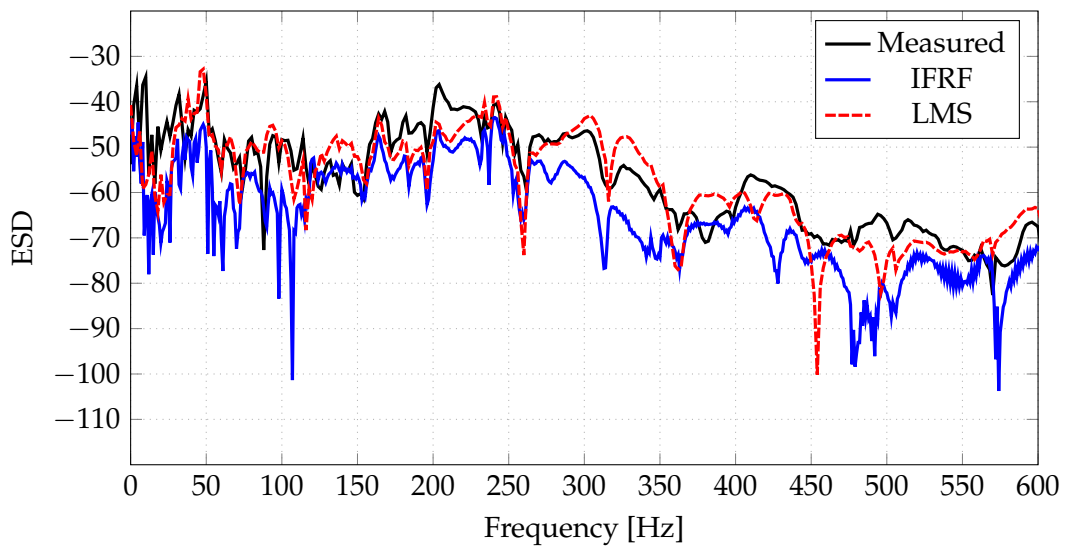


FIGURE 4.45. Showing a comparison between the spectra of the measured pressure and the calculated spectra, using an excitation in mainly Y-direction.

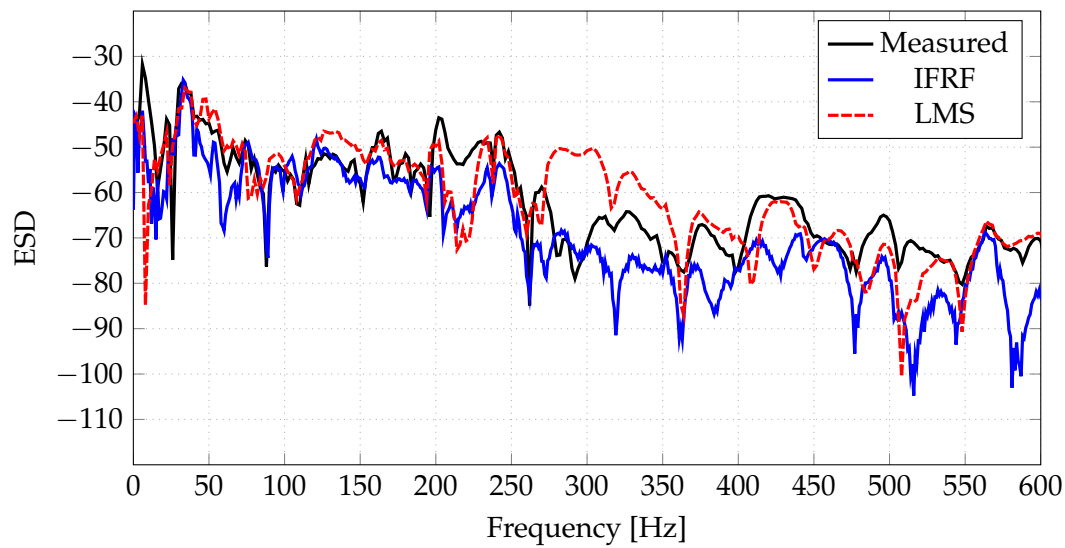


FIGURE 4.46. Showing a comparison between the spectra of the measured pressure and the calculated spectras, using an excitation in mainly Z and Y-direction.

The last results show the calculated pressure using an excitation at the center bolt of the structure in Y. From this excitation equivalent forces are calculated and from these the resulting pressure is estimated. Once again the LMS shows a better estimation for the larger part of the spectra, see figure 4.47 and 4.48.

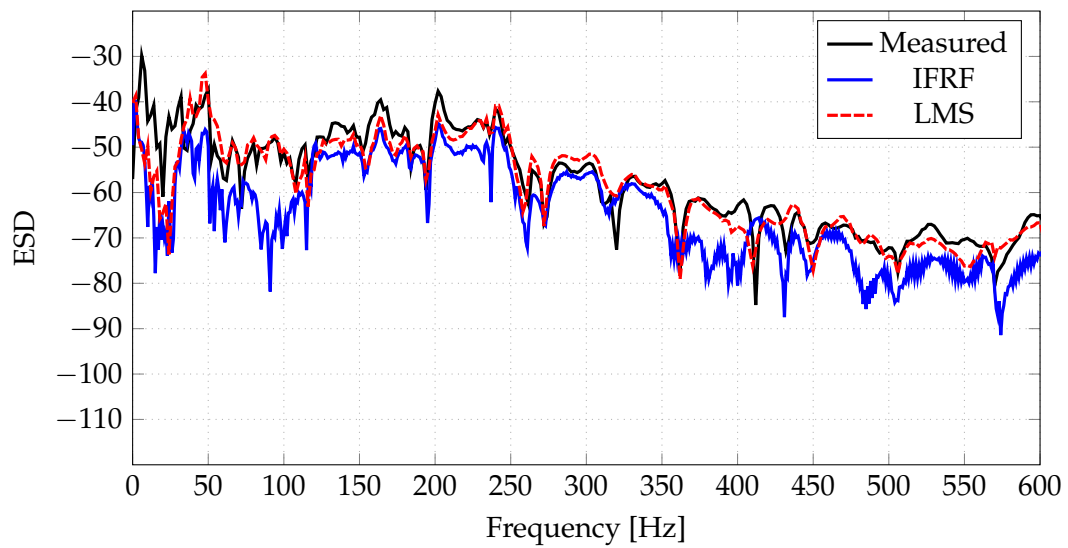


FIGURE 4.47. Showing a comparison between the spectra of the measured pressure and the calculated spectras, using an excitation in mainly Y-direction at the wheel centre (When cube was not attached).

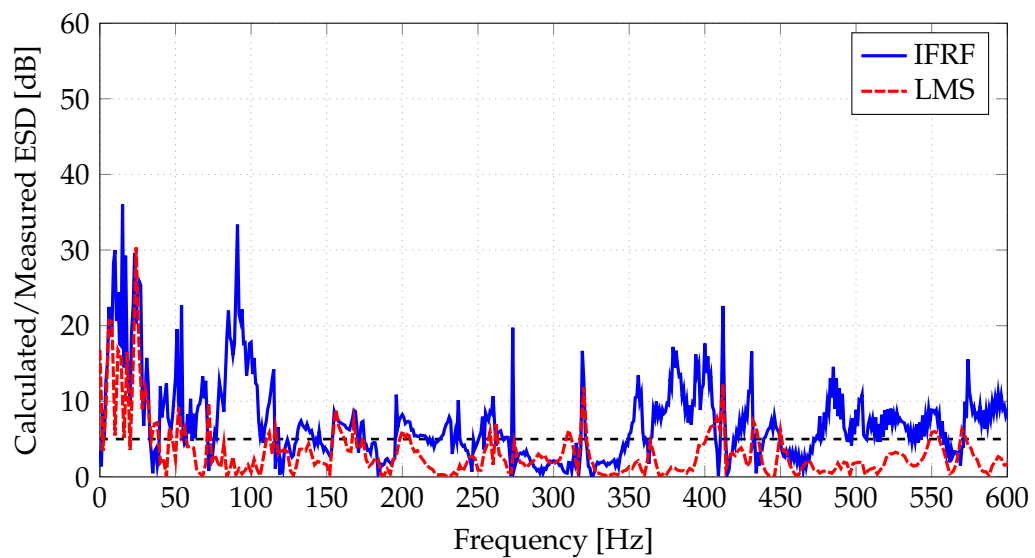


FIGURE 4.48. Showing the magnitude of the dB difference between the calculated pressure for LMS and IFRF estimated equivalent forces when excited in Y-direction at the center bolt.

4.4. Drum Measurement Simulations

The drum measurements were conducted for two of the obstacles, and at different speeds, as described in the measurements section. In the following sections however, only two cases will be studied. These are using the triangular aluminum obstacle and the smaller steel obstacle mounted on the right hand side, and rotating the drum at a speed of 30kph.

And the idea is like the previous section, to use forces giving rise to equivalent excitations, but at a position differing from the excitation position.

4.4.1. Calculation of Accelerations

The results from the calculations of accelerations show varying results, there are no large differences between the results between the two different obstacles. With this in mind the results will mostly be presented for the aluminum, or triangular, obstacle.

The first results show a comparison between the measured subframe accelerations and the calculated accelerations. Figures 4.49 to 4.52 show the results in X and Z direction for the two cases.

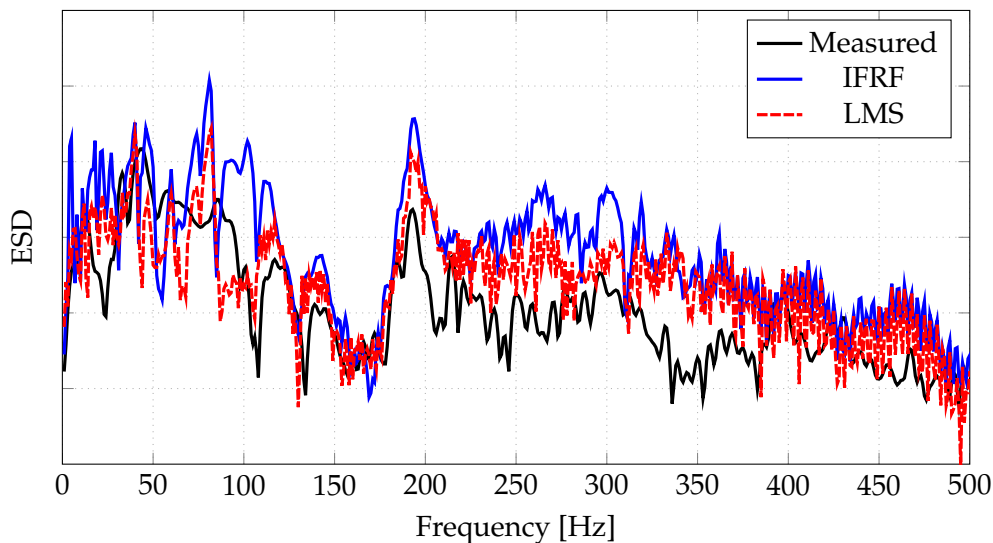


FIGURE 4.49. Showing the spectra of the calculated and measured acceleration for the case with a steel obstacle. Position is at subframe and in X-direction.

The results for the acceleration measured at bushing connecting subframe to the body is shown, for the case with aluminum triangular obstacle is shown in figures 4.53 and 4.54

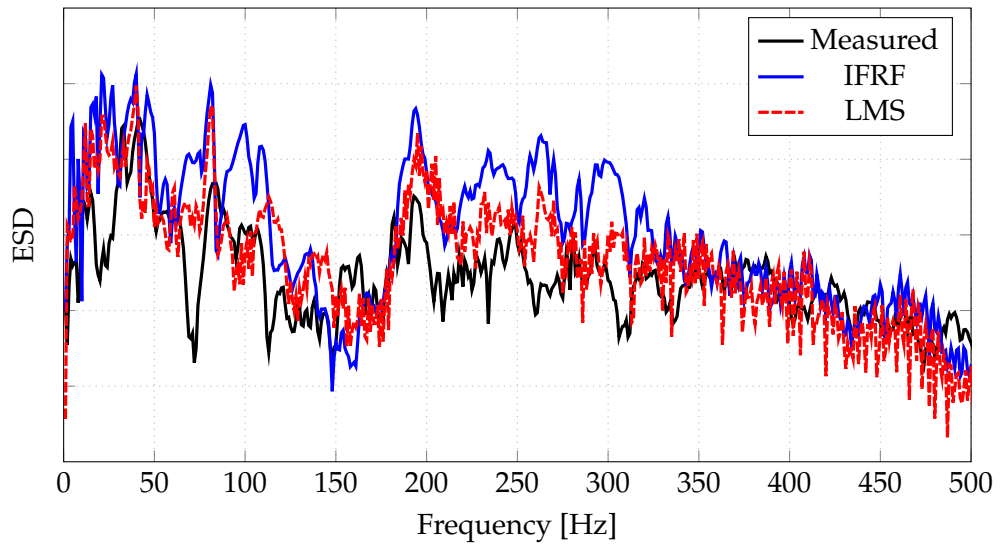


FIGURE 4.50. Showing the spectra of the calculated and measured acceleration for the case with a aluminum obstacle. Position is at subframe and in X-direction.

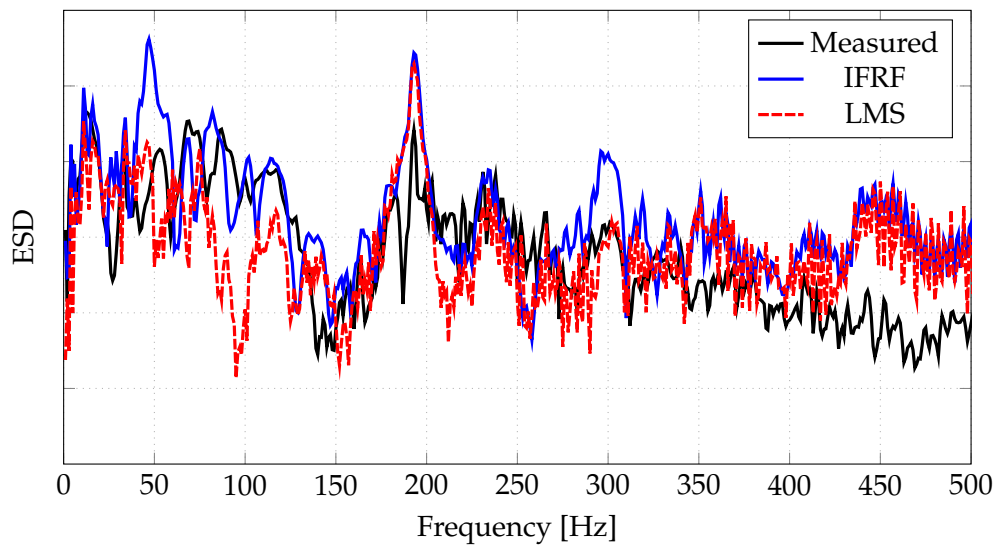


FIGURE 4.51. Showing the spectra of the calculated and measured acceleration for the case with a steel obstacle. Position is at subframe and in Z-direction.

which show the accelerations in X and Z direction respectively.

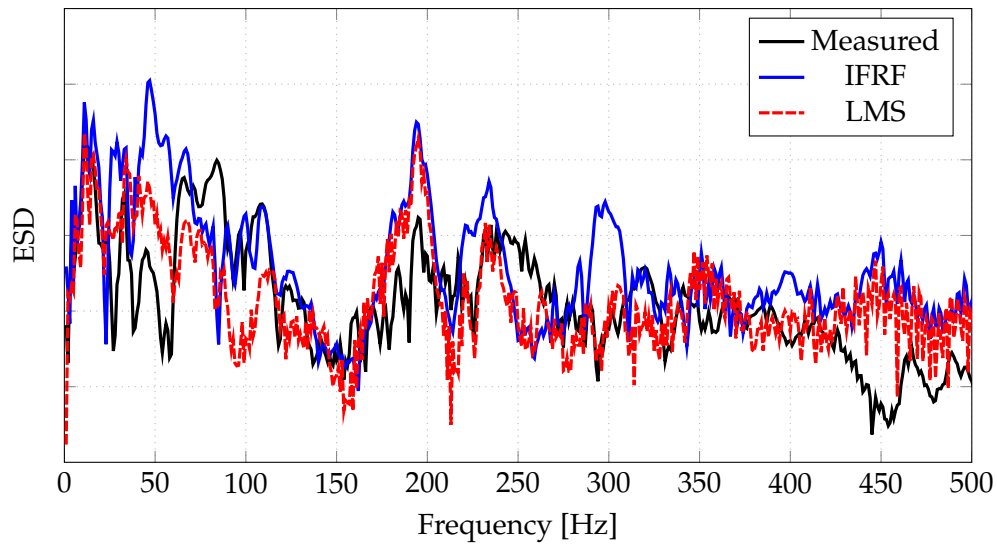


FIGURE 4.52. Showing the spectra of the calculated and measured acceleration for the case with an aluminum obstacle. Position is at subframe and in Z-direction.

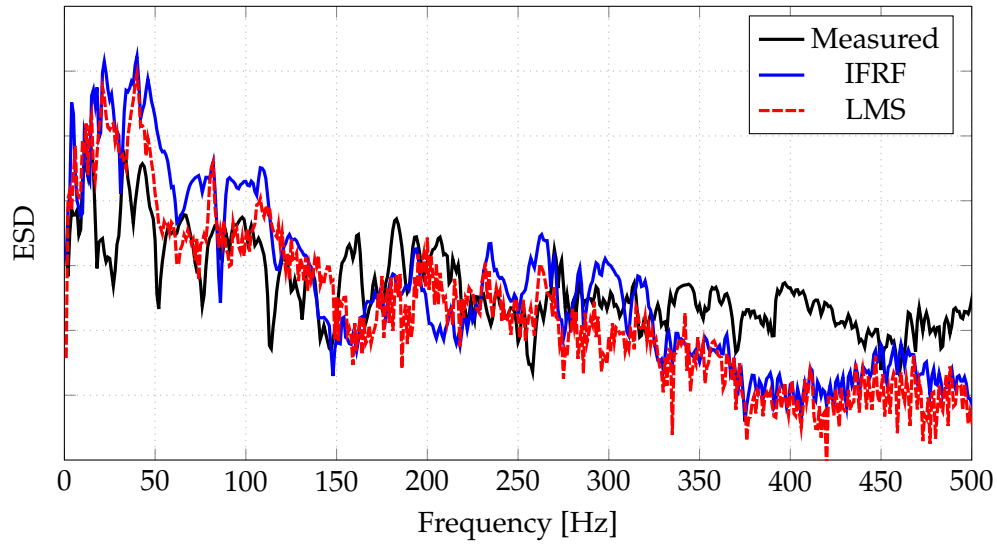


FIGURE 4.53. Showing the spectra of the calculated and measured acceleration for the case with an aluminum obstacle. Position is at body and in X-direction.

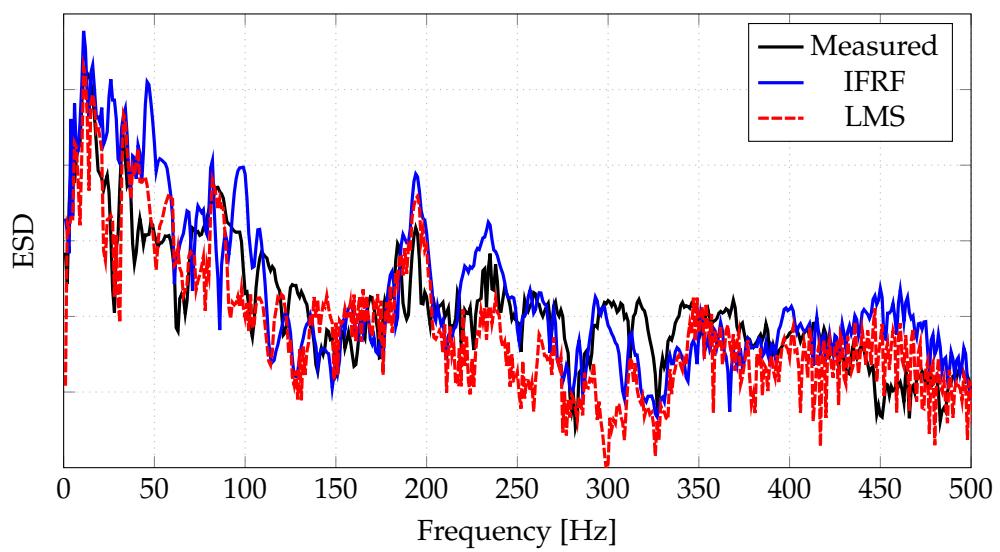


FIGURE 4.54. Showing the spectra of the calculated and measured acceleration for the case with a aluminum obstacle. Position is at body and in Z-direction.

4.4.2. Calculation of Pressure

In order to calculate pressure from the estimated forces two approaches were used. The first involved using noise transfer functions, NTF, measured at the center of the hub to the compartment. These relate only the spindle forces in X,Y and Z direction to the created sound pressure within the compartment.

The second alternative was using measured NTF's from the bushings in contact with the body. So in order to use these NTF's, the forces need to be calculated at the bushing positions, using all the excitation forces and moments, these are then used with the measured NTF's to yield pressure in the compartment. The last step is adding these contributions and using an RSS summation to average 3 separate impacts.

4.4.2.1. NTF From Spindle

Starting with the the pressures calculated with NTFs from the spindle, yields some interesting results. Figures 4.55 and 4.56 shows the measured and calculated spectra inside the compartment when the test car was driven over obstacle (iii) described in section 3.1. Both methods shows deviations from the measured pressure over the entire frequency range. The LMS-method gives a generally better approximation, especially at certain frequencies where the IFRF gives deviations up to 50dB.

The results driving over the second obstacle (ii) at the same speed yields similar results, which are displayed in figures 4.57 and 4.58. The deviations are slightly smaller in certain frequency areas but largely similar to the previous case.

The coherence for the ntf's used to calculate the pressure from the spindle is shown in figure 4.59

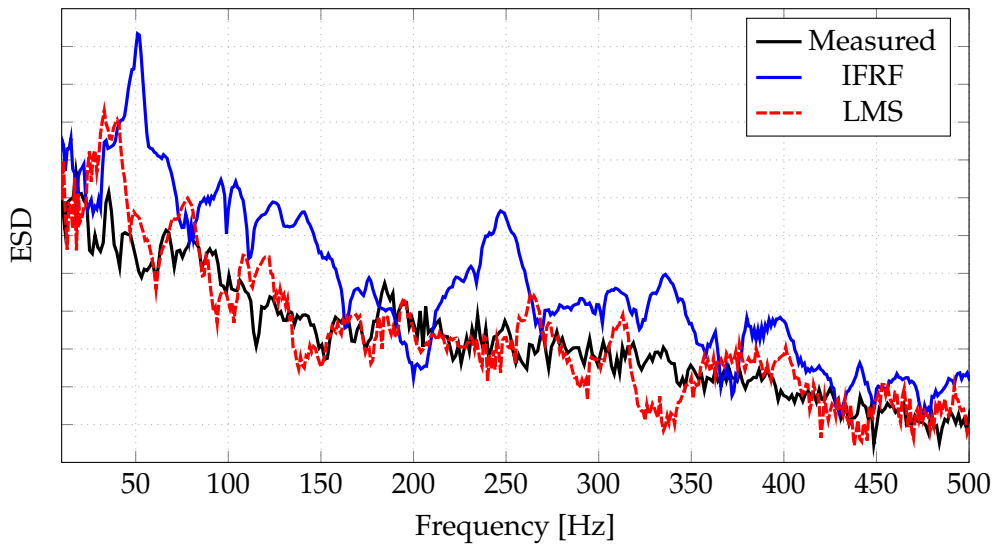


FIGURE 4.55. Showing measured pressure and comparing it to spectra calculated from IFRF- and LMS-forces via NTFs from the spindle (Car driven over obstacle (iii) at 30km/h).

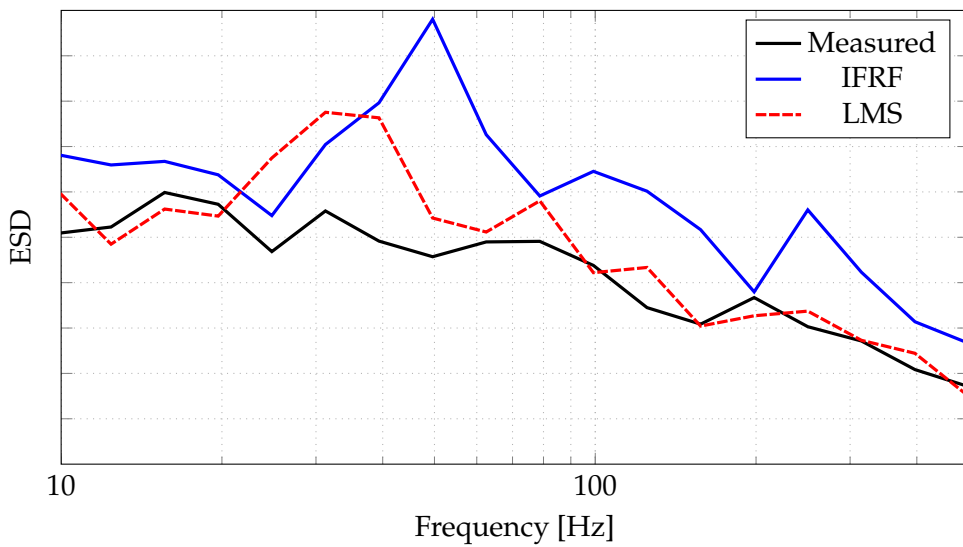


FIGURE 4.56. Showing measured pressure and comparing it to spectra calculated from IFRF- and LMS-forces via NTFs from the spindle (Car driven over obstacle (iii) at 30km/h).

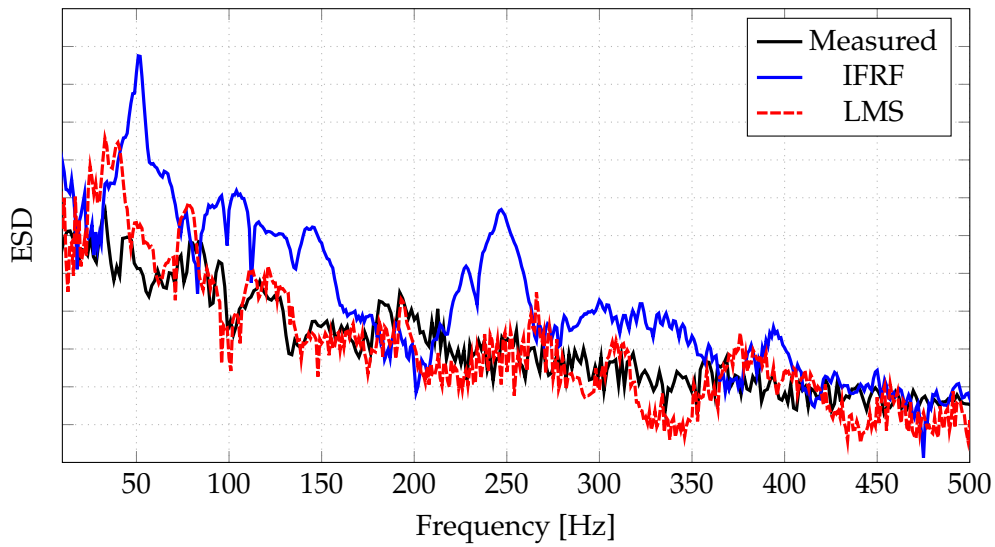


FIGURE 4.57. Showing measured pressure and comparing it to spectra calculated from IFRF- and LMS-forces via NTFs from the spindle (Car driven over obstacle (ii) at 30km/h).

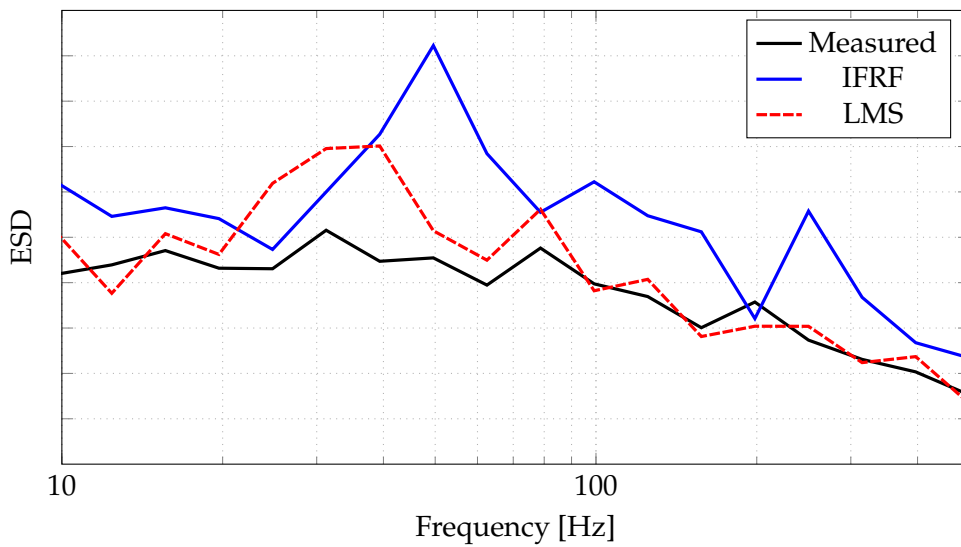


FIGURE 4.58. Showing measured pressure and comparing it to spectra calculated from IFRF- and LMS-forces via NTFs from the spindle (Car driven over obstacle (ii) at 30km/h).

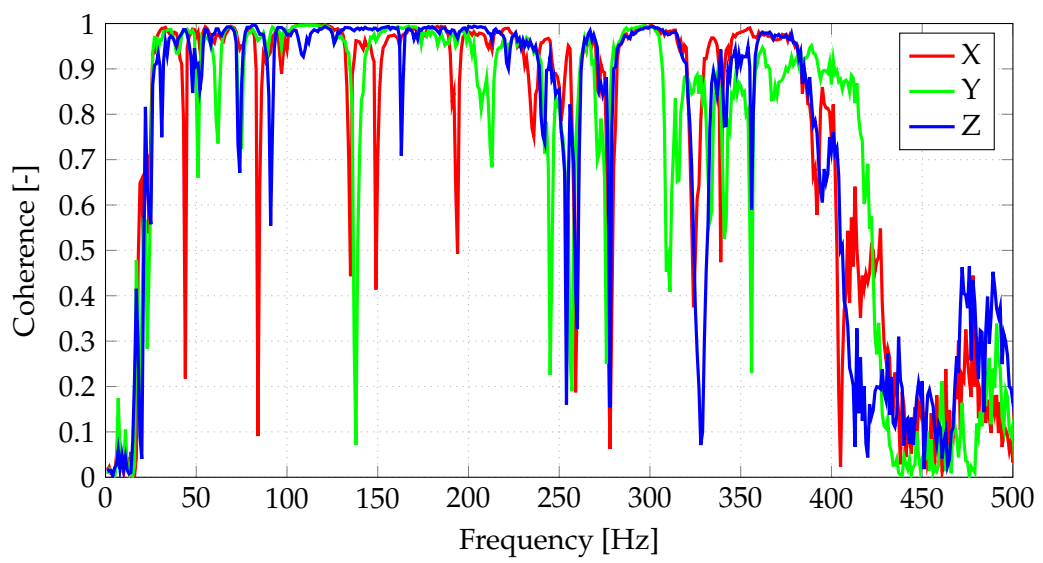


FIGURE 4.59. Showing the coherence for the different directions used.

4.4.2.2. NTF From Various Bushing Positions

Looking at the pressures calculated with NTFs from the bushings, the results are very interesting, especially compared to the results presented in the previous section. The first noticeable thing is the large improvement of the IFRF when calculating in this manner. Slight improvements can also be seen for the LMS method, especially at frequencies where calculations in the previous section were there were large deviations from measured values. Overall the forces calculated with the LMS-algorithm gives a better estimation.

A likely reason for this large improvement is that the moments are taken into account further into the chain of calculations, compared to using NTFs from the spindle. These are likely very important for the resulting pressure inside the compartment.

4.4.3. Comments On Drum Measurements

Looking at the spectra of the impulses presented in sections 4.4.1 and 4.4.2, there are few things one would expect to see, some of which is investigated in section 2.5. The cavity resonances for the tyre used in the measurements mounted to a car traveling at 30kph is according to equation (2.43):

$$f_{c1} = \frac{2 \cdot (c - 30)}{\pi \cdot (20 \cdot 2.52/100 + (20 \cdot 2.52/100 + 0.275 \cdot 0.45))} = 187\text{Hz} \quad (4.1)$$

$$f_{c2} = \frac{2 \cdot (c + 30)}{\pi \cdot (20 \cdot 2.52/100 + (20 \cdot 2.52/100 + 0.275 \cdot 0.45))} = 196\text{Hz} \quad (4.2)$$

These resonances can clearly be seen to have an effect on calculated accelerations and the resulting pressure in all measurements.

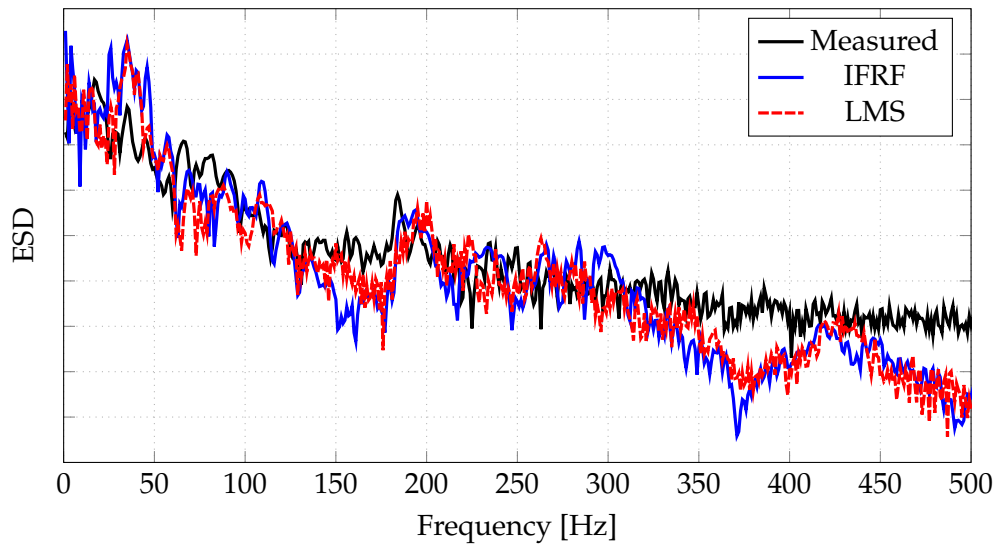


FIGURE 4.60. Showing measured pressure and comparing it to spectra calculated from IFRF- and LMS-forces via FRFs to the bushings and NTFs into the car (Car driven over obstacle (iii) at 30km/h).

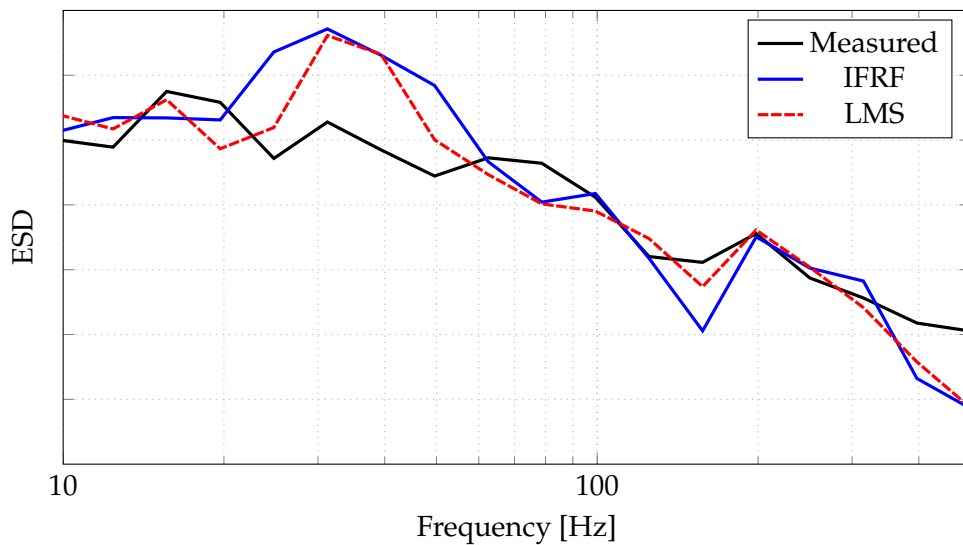


FIGURE 4.61. Showing measured pressure and comparing it to spectra calculated from IFRF- and LMS-forces via FRFs to the bushings and NTFs into the car (Car driven over obstacle (iii) at 30km/h).

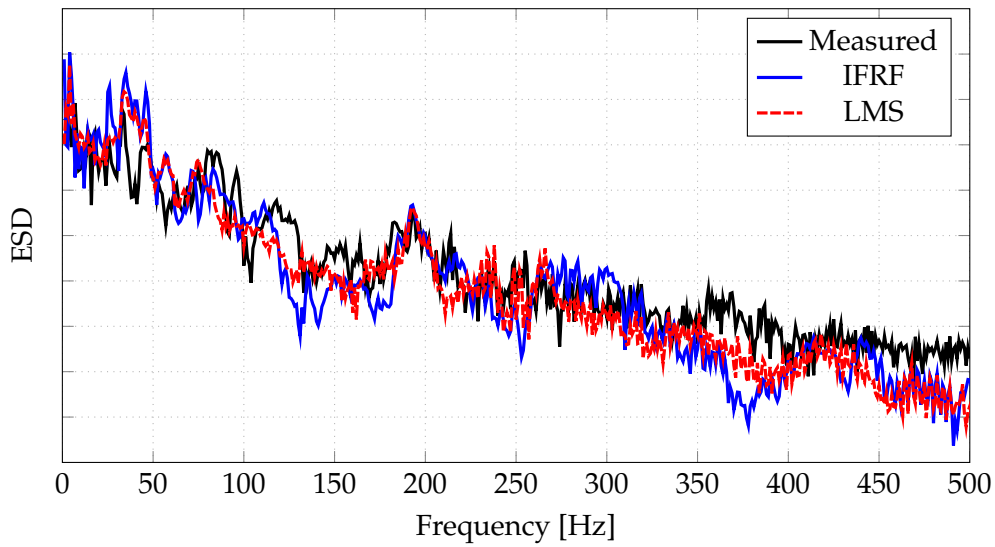


FIGURE 4.62. Showing measured pressure and comparing it to spectra calculated from IFRF- and LMS-forces via FRFs to the bushings and NTFs into the car (Car driven over obstacle (ii) at 30km/h).

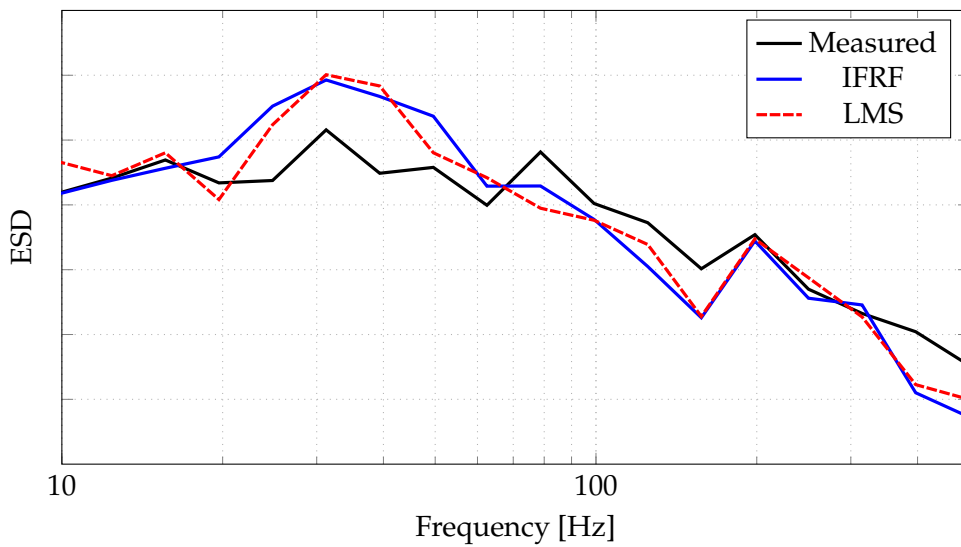


FIGURE 4.63. Showing measured pressure and comparing it to spectra calculated from IFRF- and LMS-forces via FRFs to the bushings and NTFs into the car (Car driven over obstacle (ii) at 30km/h).

5. Conclusions

The results obtained from the calculations vary from the different cases examined, and as such the cases will be commented separately at first so that some overall conclusions can be put in as concluding remarks.

5.1. Virtual simulations

As can be seen in figures 4.4 - 4.9 and 4.10 - 4.12 there is generally a good agreeance between LMS estimated forces and the original force when the exact transfer functions are known. Surprisingly, the estimation of the IFRF is rather different, especially at low frequencies, where the estimation is rather good for the LMS.

This suggests that the IFRF is less efficient when studying multiple excitations, as it uses a method of least squares to estimate the excitation force. The LMS on the other hand merely relates the derivate of the mean square error cost function to the impulse responses belonging to each individual force.

5.2. Impact Hammer Simulations

As previously stated, the IFRF seems to be less efficient when estimating several excitation forces. In these simulations, the estimation was almost identical for the two methods, until the estimation was made using three excitation forces. Then the IFRF lost some accuracy and the LMS proved to be a better alternative. Once again the answer is likely in the IFRF, and more specifically the pseudo inverse used to estimate the forces.

One can clearly see that shifting excitation position heavily affects the LMS. One possible reason to this would be that the excitation at the upper rim, gives rise to large moments, which in turn cause large accelerations. However, the moments does not affect the interior sound to the same extent as a force acting in X,Y or Z direction would. This could be due to different wave types being excited and when the algorithm tries to

estimate the excitations using equivalent force excitation, and as a result there is an overestimation at certain frequency regions.

The excitation in Y-direction at the centre of the wheel, figure 4.48, yields some results which could strengthen this assumption. The results are close to the measured, which in turn could be attributed to the fact that the excitation contains no major moment components, and as a result equivalent excitation forces can be determined from the transfer functions measured from the cube.

Perhaps it would be suitable to use other positions from which one calculate excitation forces and possibly more than one position. If chosen correctly, the position could improve the estimation. Firstly, moving the excitation position away from the centre of the hub to positions further away would mean that moments would be included in the equivalent force. This is beneficial since it would be easier to validate between measured forces and simulated forces. Which could be problematic due to difficulties in estimating the transfer functions for the pure acting moments.

5.3. Drum simulations

5.3.1. Accelerations

Studying the measured accelerations and comparing them to the calculated spectra, shows good results at some frequencies, while at others it is off by more than 10 dB. There is some difference depending on direction. But in general there is a better estimation depending on position. And the body bushing accelerations are in general estimated better.

The regions of better estimation are also the ones that prove to have better estimation when studying the pressure spectra as well. However, there is more of an overestimation made by the IFRF at these accelerations than is showed in the pressure spectra calculated from the NTF's at the bushings.

Part of the error is like before a result of the low frequency resolution, which suggests that looking at octave band levels will tell one more of the actual results obtained. And as before there are large errors at especially the lower frequencies.

5.3.2. Pressure

Studying the resulting pressure spectra, which ultimately is the end goal, there are two main interesting parts. First off, the estimation using LMS does produce more

reasonable results when only using the calculated forces in X,Y and Z direction. The large differences could be due to inaccurate phase information, but likely the issue is in the estimation of the forces itself.

Looking at the virtual simulations, the estimation of forces differed from the actual forces, especially at lower frequencies, where the IFRF tended to over estimate the excitation. If there is large phase differences between the moments and forces these would to a certain extent cancel each other out. But if the moments then are removed, the overestimation becomes clear.

This could be the explanation as to why there is no longer such a difference between the two methods when using all the excitations. The ESD show that the methods both are able to estimate the frequency content of the impulses. However, listening to the actual results indicate that while the ESD is similar, there is large differences in the time domain. This suggests that when studying random spectra, where the time domain is of little interest, the IFRF is sufficient at making the estimation.

5.4. Concluding Remarks

As discussed in the above sections, the LMS proves to be an accurate method when the actual transfer functions are known. Due to the excitation forces being estimated by their own excitations, this holds true for multiple force excitation. However it is clear that in order to produce a good estimation, the transfer functions of all forces and moments need to be known when estimating an excitation at a position differing from the actual excitation position.

This calls for one to ask whether to use another position of excitation and perhaps even several positions. This could make it easier in validating simulations to measurements.

While both methods could estimate the ESD spectra fairly well, the time domain information does not correlate well enough, something that can be heard if listening to the impulses. This suggests that for random signals, where the time domain is of little or no importance, the IFRF is a sufficient tool.

References

- [1] Stevens, K.K. : *Force Identification Problems - An Overview*, Proceedings of SEM Spring Meeting, Houston, pp. 838-844, 1987
- [2] Nelson, P. A. and Elliott, S. J. : *Active Control of Sound*, Academic Press, London, 1992
- [3] Widrow, B. and Hoff, M. : *Analog Switching Circuits*, Proceedings of the Western Electronic Show and Convention, Los Angeles, USA, 23-26 August, 1960
- [4] Proakis, J.G. and Manolakis, D. G. : *Digital Signal Processing: Principles, Algorithms and Applications*, Pearson Education, Inc., New Jersey, 2007
- [5] Uhl, T. : *The Inverse Identification Problem and its Technical Application* , Archive of Applied Mechanics, Vol. 7, Issue 5, pp. 325-337, November 2006
- [6] Stelzner, A. D., Kammer, D. C. and Milenkovic, P. : *A Time Domain Method for Estimating Forces Applied to an Unrestrained Structure*, Transaction of the ASME, Vol. 123, p. 524, October 2001
- [7] Kropp, W., Larsson, K. : *Force Estimation in the Time Domain by Applying an LMS Algorithm*, Proceedings of NOVEM, Sain-Raphaël, France, 2005
- [8] Sturm, M., Moorehouse, A., Kropp, W. and Alber, T. : *Robust Force Identification For Complex Technical Structures With Single Degree of Freedom Excitation Using an Adaptive Algorithm in Time Domain*, Proceedings of AIA-DAGA, Merano, Italy, 2013
- [9] Sturm, M., Moorehouse, A., Kropp, W. and Alber, T. : *Robust Calculation of Simultaneous Multichannel Blocked Force Signatures From Measurements Made in Time Domain*, Proceedings of ICSV20, Bangkok, Thailand, 2013
- [10] Sturm, M., Moorehouse, A., Alber, T. and Li, F.F. : *Force Reconstruction Using an Adaptive Algorithm in Time Domain*, Proceedings of ISMA2012-USD2012, xx, xx, 2012
- [11] Sandberg, U., Ejsmont, J.A. : *Tyre/road Noise Reference Book*, Informex Ejsmont & Sandberg Handelsbolag, Kisa, Sweden, 2002

- [12] Kindt, P. : *Structure-Borne Tyre/Road Noise due to Road Surface Discontinuities*, PhD Thesis, KU Leuven, 2009
- [13] Kropp, W., Larsson, K. : *A High Frequency Three-Dimensional Tyre Model Based On Two Coupled Elastic Layers*, Journal of Sound And Vibration, Volume 253, Issue 4, pp. 889-908, 2002
- [14] Jazar, R.N. : *Vehicle Dynamics: Theory and Applications* Springer Science+Business Media, New York, 2009
- [15] Thomson, J.K. : *Plane Wave Resonance in the Tire Air CAvity as a Vehicle Inter Noise Source* Tire and Noise Technology, TSTCA, Vol.23, No.1, pp. 2-10, January-March, 1995
- [16] Zwicker, K.K. and Fastl, H. : *Psychoacoustics - Facts and Models*, Springer, cop., New York, 1990.
- [17] Brandt, A. : *Noise and Vibration Analysis : Signal Analysis and Experimental Procedures*, John Wiley & Sons, cop., Hoboken NJ, USA , 2010.
- [18] Lay, D.C. : *Linear Algebra and Its Application*, Third Edition, Pearson Education, Inc., Boston, 2006
- [19] *FRONT AXLE ARM & STEERING KNUCKLE*, http://www.villagetoyotaparts.com/showAssembly.aspx?ukey_assembly=1100799 (Last visited 16/10-2014).

A. Glossary

Well-posed problem The term well-posed problem was coined by Jacques Hadamard in regards to problems describing physical problems. He proposed that a problem could be said to be well-posed if it had the following properties:

- A solution exists
- The solution is unique
- The solution's behavior changes continuously with the initial conditions.

Ill-posed problem A problem is ill-posed if it doesn't fulfill the conditions of a well-posed problem.

Ill-conditioned matrix A matrix is said to be ill-conditioned if a small change in the input will cause a large change in output.

Well-conditioned matrix A matrix is said to be well-conditioned if a small change in the input will cause a small change in output.

Over-determined An over-determined case is one where the number of inputs is larger than the number of outputs that need to be determined.

Under-determined An under-determined case is one where the number of inputs is smaller than the number of outputs that need to be determined.